Towards High-Efficiency Thin-Film Solar Cells: from Theoretical Analysis to Experimental Exploration

by

Shi Liu

A Dissertation Presented in Partial Fulfillment
of the Requirements for the Degree
Doctor of Philosophy

Approved August 2015 by the
Graduate Supervisory Committee:

Yong-Hang Zhang
Hongbin Yu
Dragica Vasileska
Shane Johnson

ARIZONA STATE UNIVERSITY

December 2015

ABSTRACT

GaAs single-junction solar cells have been studied extensively in recent years, and have reached over 28 % efficiency. Further improvement requires an optically thick but physically thin absorber to provide both large short-circuit current and high open-circuit voltage. By detailed simulation, it is concluded that ultra-thin GaAs cells with hundreds of nanometers thickness and reflective back scattering can potentially offer efficiencies greater than 30 %. The 300 nm GaAs solar cell with AlInP/Au reflective back scattering is carefully designed and demonstrates an efficiency of 19.1 %. The device performance is analyzed using the semi-analytical model with Phong distribution implemented to account for non-Lambertian scattering. A Phong exponent *m* of ~12, a non-radiative lifetime of 130 ns, and a specific series resistivity of 1.2 $\Omega \cdot cm^2$ are determined.

Thin-film CdTe solar cells have also attracted lots of attention due to the continuous improvements in their device performance. To address the issue of the lower efficiency record compared to detailed-balance limit, the single-crystalline Cd(Zn)Te/MgCdTe double heterostructures (DH) grown on InSb (100) substrates by molecular beam epitaxy (MBE) are carefully studied. The $Cd_{0.9946}Zn_{0.0054}Te$ alloy lattice-matched to InSb has been demonstrated with a carrier lifetime of 0.34 μs observed in a 3 μm thick $Cd_{0.9946}Zn_{0.0054}Te$/MgCdTe DH sample. The substantial improvement of lifetime is due to the reduction in misfit dislocation density. The recombination lifetime and interface recombination velocity (IRV) of CdTe/$Mg_xCd_{1-x}Te$ DHs are investigated. The IRV is found to be dependent on both the MgCdTe barrier height and width due to the thermionic emission and tunneling processes. A record-long carrier lifetime of 2.7 μs and a record-low IRV of close to zero have been confirmed experimentally.

The MgCdTe/Si tandem solar cell is proposed to address the issue of high manufacturing costs and poor performance of thin-film solar cells. The MBE grown $Mg_xCd_{1-x}Te/Mg_yCd_{1-y}Te$ DHs have demonstrated the required bandgap energy of 1.7 eV, a carrier lifetime of 11 ns, and an effective IRV of $(1.869 \pm 0.007) \times 10^3$ cm/s. The large IRV is attributed to thermionic-emission induced interface recombination. These understandings can be applied to fabricating the high-efficiency low-cost MgCdTe/Si tandem solar cell.

This work is dedicated to my girlfriend, Yu Guo, and my parents, Xinyou Liu and Xuyong Han, whose love and support have made it possible to pursue my dreams.

ACKNOWLEDGMENTS

First and foremost, I would like to thank my research advisor Dr. Yong-Hang Zhang, for his guidance and supervision for the past five years. I have benefited significantly from his clear and deep understanding of optoelectronic device physics and his rigorous way and attitude of conducting scientific research. I would also like to thank Dr. Shane Johnson, who has also been a mentor to me, particularly in regards to the operation and maintenance of MBE system, and the theory of photovoltaic devices. I am also thankful to Dr. Dragica Vasileska for her teaching in the field of numerical simulation in semiconductor devices, and Dr. Hongbin Yu for his mentoring in material characterization such as atomic force microscopy. I also would like to thank Dr. David Smith, who had taught me on how to write and present the research work. The advice and feedback of my research work from these committee members and professors are especially valuable and I am grateful for that.

I am thankful to many current and previous colleagues for their help and mentoring in the past years. Especially, I am indebted to Dr. Ding Ding, Dr. Hua Li, Dr. Oray O. Cellek, Dr. Jin Fan, Dr. Jing-Jing Li, Dr. Michael DiNezza, Dr. Qiang Zhang, Dr. Weiquan Yang, Dr. Stuart Farrell, and Dr. Elizabeth Steenbergen. Special thanks to the group members that are directly related to my research work: Dr. Weiquan Yang, Jacob Becker, and Ying-Shen Kuo fabricated the nice ultra-thin GaAs solar cell and did the device testing; Dr. Michael DiNezza developed the CdTe growth recipe and demonstrated the very first world record of CdTe lifetime; Xin-Hao Zhao carried out all the TRPL measurement and contributed a lot to the analysis; Calli Campbell assisted in CdTe MBE growth and did a lot XRD measurements; Maxwell Lassise assisted with the InSb growth; Yuan Zhao provided his help with photon recycling factor calculation and a few PL measurements;

Preston Webster contributed to my understanding of MBE through a lot of discussions and many MBE maintenance hours; Jing Lu provided TEM images of our CdTe samples.

Several ASU and external organizations also contributed to this work. The Center for Solid State Electronics Research (CSSER) provided the fabrication tools for the GaAs solar cell processing. The Leroy Eyring Center for Solid State Science (CSSS) provided the characterization equipment such as XRD. The Biodesign Institute provided the time-correlated single photon counting system for TRPL measurement. The John M. Cowley Center for High Resolution Electron Microscopy provided the electron microscopy facility. External collaborations include Sumika Electronic Materials (GaAs project), First Solar (CdTe project), and the National Renewable Energy Laboratory (CdTe project).

Funding from numerous sources has made this work possible, and I am grateful for their support. The research grants that supported this work include: Science Foundation Arizona (Contract No. SRG 0339-08), National Science Foundation (Grant No. 1002114), Air Force Office of Scientific Research (Grant No. FA9550-12-1-0444), Department of Energy/Bay Area Photovoltaic Consortium (Award No. DE-EE0004946), and Department of Energy/FPACE II (Contract No. DE-AC36-08GO28308).

TABLE OF CONTENTS

Page

CHAPTER Page

LIST OF TABLES

Table Page

LIST OF FIGURES

Figure Page

Figure Page

Figure Page

Figure Page

Figure Page

Figure Page

Figure Page

Figure Page

CHAPTER 1

INTRODUCTION

Energy is related to almost all aspects of human society, including residential, commercial, industrial, and transportation use. The total energy consumption in the US had reached 97.3 quadrillion Btu in 2013, which is a 2.4 % increase from 2012. Currently a large portion of the energy consumption is supplied by fossil fuels, such as petroleum, coal, and natural gas. However, there is only a limited storage of these fuels on earth and they are considered non-renewable energy sources. As a result, renewable energy (including Biomass, hydropower, solar, wind, and geothermal) usage has seen rapid growth in recent decades. The installed global renewable electricity capacity has grown 108 % (from 748 GW to 1560 GW) between 2000 and 2013, and comprised 27 % of the total electricity capacity, and 23 % of all electricity generation worldwide in 2013, representing a significant and growing portion of the total energy supply. In the US, between the year's 2008 to 2013, the total renewable electricity generation increased by 40 %, and now occupies 14.8 % of the total electricity capacity and 13.1 % of the annual electricity generation [1].

In particular, Photovoltaics (PV), as an emerging renewable energy generation technology, has experienced the fastest growth in both technology development and market share expansion over the past ten years. Figure 1.1 below shows the continuous improvements of the best research cell efficiencies [2]. Some important numbers include: 46.0 % achieved by concentrated III-V multi-junction solar cell [3][4], 28.8 % achieved by thin-film GaAs solar cell [5][6], 25.6 % achieved by single-crystalline Si HIT solar cell [7], 21.5 % achieved by thin-film CdTe solar cell [8], 21.7 % achieved by CIGS solar cell [9],

and so on [6]. As for the market share, the US PV capacity has grown by a factor of 35 from 2000 to 2013, and global PV energy generation has grown by a factor of 68 in the same timeframe. In 2013, the cumulative PV electricity capacity increased by 66 % in US, which accounts for more than 63 % of the total installed renewable energy capacity [1].

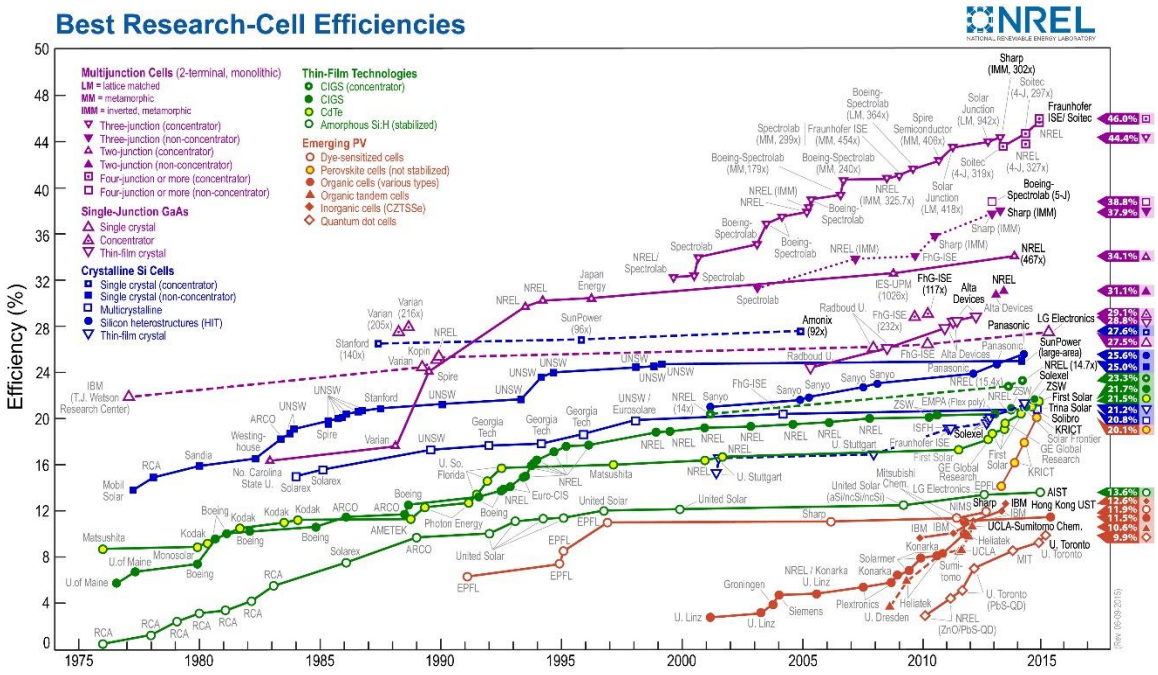

Figure 1.1. Efficiency chart of best research cells [2].

Despite the rapid growth, the percentage of electrical power generated by PV is still much smaller than the other energy resources. In 2013, PV energy represents 1.1 % of the US overall electricity nameplate capacity and 0.5 % of the US overall electricity net generation [1]. The major obstacle is its high manufacturing cost. Thus the US Department of Energy has launched the SunShot initiative, aiming to make large-scale PV system cost-comparable to other energy sources by 2020. Among all the PV technologies, thin-film

solar cells show great potentials in achieving the goals of improving the cell efficiency while further reducing the manufacturing cost.

1.1 GaAs solar cell

The power conversion efficiency record of GaAs single-junction solar cells has been broken frequently in the past several years due to the utilization of epitaxial lift-off techniques [5][10], in which the grown GaAs solar cell is lifted-off from the GaAs substrate and transferred to a low-cost flexible carrier to make a thin-film device. The GaAs substrate then undergoes certain treatments before being used for the next epitaxial growth. Typically the substrate can be reused about six times, effectively reducing the substrate cost by over 80 %. A highly-reflective mirror is deposited on the backside of the cell, which helps to increase the optical length of the cell, as well as to trap the luminescence photons inside the absorber. Using the above technology, Alta Devices has achieved the efficiency world record of 28.8 % for a single junction GaAs cell [6].

Along with the enhancement of GaAs solar cell performance, the underlying physics is attracting people's attentions. The detailed-balance model, proposed by Shockley and Queisser [11] and later on developed by Henry [12], clearly explains the fundamental physics of solar cells. However, the detailed balance model is only capable of clarifying a theoretical efficiency limit as it only considers ideal step-like absorption and radiative recombination loss. Therefore, a semi-analytical model was built by Ding et al., which includes non-radiative recombination, non-step-like absorptance and emittance, real material parameters including the absorption tail below the bandgap, and device geometries [13][14]. This model enables the capability to study the impact of device geometries on the

device performance of solar cells with non-ideal material quality taken into account, and thus can provide guidance in practical device design.

1.2 CdTe solar cell

CdTe, another major material for thin film photovoltaic technology, has also attracted a lot of interests in recent years due to continuous improvements in device performance and market share. The efficiency record of polycrystalline CdTe solar cells has been frequently broken, and has reached 21.5 % up to now [8]. However, this is still more than ten absolute percent lower than the Shockley-Queisser limit [11]. Despite that the short-circuit current density (J_{sc}) is already close to the theoretical limit, there is still significant room for further improvement in open-circuit voltage (V_{oc}) and fill factor (FF), which are currently still below 0.9 V and 80 % for most devices [15]. Such imperfections are believed to be due to the large defect density, short minority carrier lifetime and so on associated with polycrystalline materials. The use of monocrystalline CdTe is anticipated to help improve the V_{oc} dramatically due to its better material quality and longer carrier lifetime. DiNezza et al. reported a long carrier lifetime of 86 ns observed in an epitaxial 1 μm CdTe/MgCdTe double heterostructure (DH) grown on an InSb substrate [16], and a theoretical study shows that a V_{oc} of ~1.05 V and an energy conversion efficiency of ~25 % can be potentially achieved [17]. The radiative recombination coefficient has also been determined to be $(4.3 \pm 0.5) \times 10^{-9}$ cm^3 s^{-1} [18]. A following paper shows an improved lifetime of 179 ns in a sample with a 2 μm CdTe layer, and the CdTe/$Mg_{0.24}Cd_{0.76}Te$ interface recombination velocity has been determined as $(4.7 \pm 0.4) \times 10^2$ cm/s [19]. Other studies involving the lifetime of monocrystalline CdTe were reported by Kuciauskas et al.

claiming 66 ns and 360 ns measured by a 2-photon excitation technique [20][21], and by Swartz et al. claiming 240 ns [22]. Recently a V_{oc} greater than 0.9 V was achieved using monocrystalline CdTe [23].

1.3 Organization of this paper

This paper focuses on the research efforts along the road to developing high-performance thin-film GaAs and CdTe solar cells.

Chapter 2 is about the theoretical study, practical device design, experimental demonstration and analysis of ultra-thin GaAs single-junction solar cells. In Section 2.1, ten GaAs single-junction solar cells with different combinations of smooth, textured, non-reflective, and reflective surfaces are studied, in order to explore the optimal optical design, and their achievable efficiency limits are established [24][25]. The non-Lambertian scattering is then discussed in Section 2.2. From a practical point of view, a wide bandgap back scattering layer coated with highly reflective mirror can be integrated with an ultra-thin GaAs solar cell to reach the achievable efficiency limit [26][27]. In Section 2.3, a few designs have been explored regarding the ultra-thin cell with reflective back scattering. Several materials for the back scattering layer and the mirror are carefully compared by using the modified formula, which takes into account the absorption in the scattering layer and reflection loss of the backside mirror. The anti-reflection (AR) coating design for ultra-thin GaAs single-junction solar cells is optimized by finding the minimum reflection design of a multi-layer structure, which includes window layer, ultra-thin absorber, and back surface field (BSF) layer, and utilizes the transfer matrix method. The fabricated device with 300 nm absorber achieves an efficiency of 19.1 %, which is however quite below the

predicted achievable efficiency. The difference between achieved and predicted device performance is carefully investigated in this report. Specifically, the non-Lambertian scattering, non-unity back mirror reflectivity, non-radiative recombination, and series resistance in the device are discussed [28].

Chapter 3 focuses on the single-crystalline CdTe/MgCdTe grown by molecular beam epitaxy (MBE), and characterized by x-ray diffraction (XRD), steady-state photoluminescence (PL), and time-resolved photoluminescence (TRPL). In particular, the CdTe/MgCdTe DH is used to study the optical properties. In Section 3.1, the fundamentals of MBE are firstly introduced, including ultra-high vacuum (UHV), atomic/molecular beam generation, and *in-situ* characterizations. Following that are the detailed growth procedures of InSb and CdTe, and the growth rate and flux ratio calibration methods. In Section 3.2, the CdZnTe alloy lattice-matched to InSb is proposed and demonstrated [29]. The structural and optical properties of a CdZnTe/MgCdTe DH are compared with those of a CdTe/MgCdTe DH with identical thickness. In Section 3.3, the interface recombination velocities of various CdTe/MgCdTe DH samples with different Mg compositions and MgCdTe thicknesses are studied [30][31]. For each DH sample set, several samples with different CdTe layer thicknesses are grown and characterized, and the corresponding interface recombination velocity is extracted. A model is also developed to study the carrier escape via thermionic emission over or tunneling through the MgCdTe barrier and its impact on the recombination mechanisms in the CdTe/MgCdTe DHs. In Section 3.4, the initial demonstration of 1.7 eV MgCdTe alloys is presented. The grown samples show excellent structural and optical qualities, showing that MgCdTe is promising for II-VI/Si tandem solar cell applications.

CHAPTER 2

HIGH-EFFICIENCY ULTRA-THIN GAAS SINGLE-JUNCTION SOLAR CELLS APPROACHING THEORETICAL LIMIT

Theoretical and experimental approaches have been carried out to improve the device performance of GaAs single-junction solar cells. To achieve making an "optically thick but physically thin" structure, 10 different optical designs of GaAs single-junction solar cells, which feature scattering and reflection inside the cell, are compared with each other. This comparison is essential to shine a light on the novel solar cell structure design targeting the maximum achievable efficiency. At the same time, from a practical point of view, the impact of non-Lambertian scattering are carefully examined so that a lower bound of the achievable performance is well understood. After that, the designs for the back scattering layer, the mirror and the AR coating, are presented regarding the ultra-thin solar cell structure, followed by a thorough analysis of the actual performance of the fabricated cell.

2.1 Optimal optical designs of GaAs single-junction solar cells

Considering non-ideal materials, the optimal structure design results from the tradeoff between maximizing the absorption of incoming photons and minimizing Shockley-Read-Hall (SRH) losses. This requires an optically thick, but physically thin absorber. It is therefore necessary to consider various optical designs that provide efficient light trapping to further improve the effective absorption of the incident light and the overall energy conversion efficiency.

2.1.1 Planar structures

The optical optimization process considers seven different surfaces and their combinations. The front surface is non-reflective and categorized by two bounds according to its ability to scatter light: i) smooth surface or ii) textured surface. The back surface is categorized by five cases: i) non-reflective interface, ii) smooth ideal reflective surface, iii) textured ideal reflective surface, iv) smooth surface with reflectivity R, and v) textured surface with reflectivity R'. The 10 planer structures constructed based on these surfaces are schematically shown in Figure 2.1.1. The non-reflective interfaces of Structure A and B represents devices grown on index-matched substrates; the smooth or textured ideal back reflective surfaces of Structure C, D, E, and F represent mirrors on the backside of the solar cells with reflectivity equals one; and the smooth or textured back surfaces of Structure G, H, I, and J describe the case where substrates have been removed.

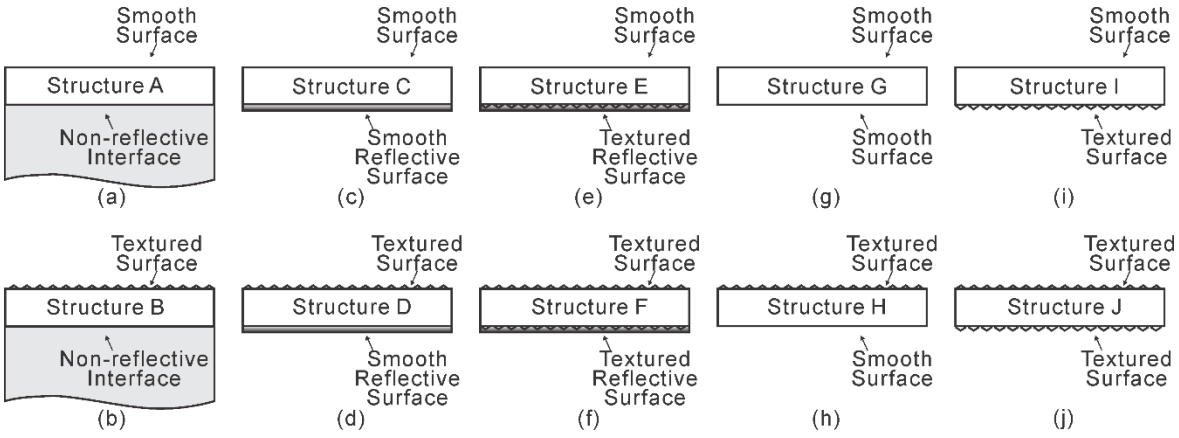

Figure 2.1.1. Schematic structures of the 10 studied GaAs single-junction solar cells.

2.1.2 Optical properties calculation

The well-known detailed balance model considers ideal step-like absorptance and emittance, assuming the solar cell is opaque at energies above bandgap and transparent at energies below bandgap, which by the way implicitly assumes a perfect photon recycling process. In practice, one must take the real absorption coefficients into consideration, including the below-bandgap absorption like the Urbach tail [32]. This leads to less than ideal absorptance, emittance, and photon recycling properties that are not negligible when considering real solar cell performance.

Statistical ray tracing is used to derive the absorptance and emittance of the 10 planar structures, assuming the maximal scattering case with an angular Lambertian distribution. Equations (2.1.1a)-(2.1.1j) shown below provide the wavelength-dependent absorptance of Structures A through J, respectively. Here α is absorption coefficient, d is absorber thickness, and n_r is the refractive index. R and R' are the angle-independent reflectivities of smooth and textured back surfaces, respectively. The term $(1\text{-}1/n_r^2)$ is the fraction of light from all light paths within the semiconductor that is reflected from a non-reflective semiconductor to air interface, which is the minimum fraction that can be reflected from a semiconductor to air interface (textured or smooth).

$$A_A \cong 1 - e^{-\alpha \cdot d} \tag{2.1.1a}$$

$$A_B = 1 - t_B \tag{2.1.1b}$$

$$A_C \cong 1 - e^{-2\alpha \cdot d} \tag{2.1.1c}$$

$$A_D = \frac{1 - t_D}{1 - \left(1 - \frac{1}{n_r^2}\right) \cdot t_D} \tag{2.1.1d}$$

$$A_E \cong 1-e^{-\alpha d}\frac{t_{E1}}{1-t_{E2}} \tag{2.1.1e}$$

$$A_F = \frac{1-t_F^2}{1-t_F^2\cdot\left(1-\frac{1}{n_r^2}\right)} \tag{2.1.1f}$$

$$A_G \cong \left(1-e^{-\alpha d}\right)\left(1+e^{-\alpha d}R\right) \tag{2.1.1g}$$

$$A_H = \frac{1-t_{H11}\left(1-R\right)-R\cdot t_{H12}-t_{H2}}{1-\left(R\cdot t_{H12}+t_{H2}\right)\left(1-\frac{1}{n_r^2}\right)} \tag{2.1.1h}$$

$$A_I \cong 1-e^{-\alpha d}\cdot\frac{1-\left(1-t_{I1}\right)\cdot\left(1-\frac{1-R'}{n_r^2}\right)}{1-t_{I2}\cdot\left(1-\frac{1-R'}{n_r^2}\right)} \tag{2.1.1i}$$

$$A_J = \frac{\left(1-t_J\right)\cdot\left[1+t_J\cdot\left(1-\frac{1-R'}{n_r^2}\right)\right]}{1-t_J^2\cdot\left(1-\frac{1}{n_r^2}\right)\cdot\left(1-\frac{1-R'}{n_r^2}\right)} \tag{2.1.1j}$$

Term *t* is the fraction of transmitted light in a single pass through the cell, with subscripts referring to different ray paths of the 10 planar structures: "1" refers to the ray paths within the escape cone and "2" refers to the ray paths outside the escape cone.

$$t_B = t_F = t_J = \int_0^{\frac{\pi}{2}} e^{-\alpha d/\cos\theta}\cdot 2\cos\theta\sin\theta\cdot d\theta \tag{2.1.2a}$$

$$t_D = \int_0^{\frac{\pi}{2}} e^{-2\alpha d/\cos\theta}\cdot 2\cos\theta\sin\theta\cdot d\theta \tag{2.1.2b}$$

$$t_{H11} = \int_0^{\theta_c} e^{-\alpha d/\cos\theta}\cdot 2\cos\theta\sin\theta\cdot d\theta \tag{2.1.2c}$$

$$t_{H12} = \int_0^{\theta_c} e^{-2\alpha d/\cos\theta} \cdot 2\cos\theta \sin\theta \cdot d\theta \tag{2.1.2d}$$

$$t_{E1} = t_{I1} = \int_0^{\theta_c} e^{-\alpha d/\cos\theta} \cdot 2\cos\theta \sin\theta \cdot d\theta \tag{2.1.2e}$$

$$t_{E2} = t_{H2} = t_{I2} = \int_{\theta_c}^{\frac{\pi}{2}} e^{-2\alpha d/\cos\theta} \cdot 2\cos\theta \sin\theta \cdot d\theta \tag{2.1.2f}$$

where θ is the angle between scattered light and surface normal, and θ_c is the critical angle of total reflection of semiconductor-air interface. Lambertian scattering is assumed so that the fraction of light intensity distributed in the solid angle $sin\theta \cdot d\theta$ is $cos\theta$; the factor "2" is the result of normalization over angle. The Lambertian distribution here can be replaced by other manually generated distributions to imitate insufficient scattering case.

By assuming emittance equals absorptance when background blackbody radiation is incident from all angles at equilibrium [33], the front and back surface emittance can be obtained from the absorptance in the case where the background radiation is assumed incident at all angles (as shown below). The assumption is valid since most solar cells work at low injection level.

$$\varepsilon_{front,\,A} = 1 - n_r^2 \int_0^{\theta_c} e^{-\alpha d/\cos\theta} \cdot 2\cos\theta \sin\theta \cdot d\theta \tag{2.1.3a}$$

$$\varepsilon_{front,\,B} = A_B \tag{2.1.3b}$$

$$\varepsilon_{front,\,C} = 1 - n_r^2 \int_0^{\theta_c} e^{-2\alpha d/\cos\theta} \cdot 2\cos\theta \sin\theta \cdot d\theta \tag{2.1.3c}$$

$$\varepsilon_{front,\,D} = A_D \tag{2.1.3d}$$

$$\varepsilon_{front,\,E} = 1 - t_{\alpha 3} \cdot \frac{t_{\alpha 1}}{1 - t_{\alpha 2}} \tag{2.1.3e}$$

$$\varepsilon_{front,\,F} = A_F \tag{2.1.3f}$$

$$\varepsilon_{front,\,G} = \int_0^{\theta_c} \left(1 - e^{-\alpha d/\cos\theta}\right)\left(1 + e^{-\alpha d/\cos\theta} R\right) \cdot 2n_r^2 \cos\theta \sin\theta \cdot d\theta \tag{2.1.3g}$$

$$\varepsilon_{front,\,H} = A_H \tag{2.1.3h}$$

$$\varepsilon_{front,\,I} = 1 - t_{\alpha 3} \cdot \frac{1 - \left(1 - t_{\alpha 1}\right) \cdot r \cdot \left(1 - \dfrac{1}{n_r^2}\right)}{1 - t_{\alpha 2} \cdot r \cdot \left(1 - \dfrac{1}{n_r^2}\right)} \tag{2.1.3i}$$

$$\varepsilon_{front,\,J} = A_J \tag{2.1.3j}$$

$$\varepsilon_{back,\,A} = 1 - \int_0^{\theta_c} e^{-\alpha d/\cos\theta} \cdot 2\cos\theta \sin\theta \cdot d\theta - \int_{\theta_c}^{\frac{\pi}{2}} e^{-2\alpha d/\cos\theta} \cdot 2\cos\theta \sin\theta \cdot d\theta \tag{2.1.4a}$$

$$\varepsilon_{back,\,B} = \left(1 - t_\alpha\right)\left[1 + t_\alpha \left(1 - \frac{1}{n_r^2}\right)\right] \tag{2.1.4b}$$

$$\varepsilon_{back,\,C} = 0 \tag{2.1.4c}$$

$$\varepsilon_{back,\,D} = 0 \tag{2.1.4d}$$

$$\varepsilon_{back,\,E} = 0 \tag{2.1.4e}$$

$$\varepsilon_{back,\,F} = 0 \tag{2.1.4f}$$

$$\varepsilon_{back,\,G} = \int_0^{\theta_c} \left(1 - e^{-\alpha d/\cos\theta}\right)\left(1 - R\right) \cdot 2n_r^2 \cos\theta \sin\theta \cdot d\theta \tag{2.1.4g}$$

$$\varepsilon_{back,\,H} = \left(1 - R\right) \cdot \left\{1 - t_{\alpha 3} \cdot \frac{1 - \left[1 - \left(1 - R\right) \cdot t_{\alpha 11}\right] \cdot \left(1 - \dfrac{1}{n_r^2}\right)}{1 - \left(R \cdot t_{\alpha 12} + t_{\alpha 2}\right) \cdot \left(1 - \dfrac{1}{n_r^2}\right)}\right\} \tag{2.1.4h}$$

$$\varepsilon_{back,\,I} = \frac{\left(1 - R\right) \cdot \left(1 - t_{\alpha 1} - t_{\alpha 2}\right)}{1 - t_{\alpha 2} \cdot r \cdot \left(1 - \dfrac{1}{n_r^2}\right)} \tag{2.1.4i}$$

$$\varepsilon_{back,\,J} = \frac{(1-R)\left(1-t_\alpha\right)\cdot\left[1+t_\alpha\cdot\left(1-\frac{1}{n_r^2}\right)\right]}{1-t_\alpha^2\cdot r\cdot\left(1-\frac{1}{n_r^2}\right)^2} \tag{2.1.4j}$$

Moreover, photon extraction and photon recycling factors can be extracted from emittance [14]. Here photon recycling refers to the process that photons generated by radiative recombination undergo many absorption-emission cycles before finally escaping from the device. The photon recycling factor is defined as the fraction of spontaneously emitted photons that are reabsorbed by the device [34]. The photon extraction factor is defined as the fraction of spontaneously emitted photons that are extracted from the device. The photon extraction factor of a semiconductor/air surface and a semiconductor/semiconductor interface are shown below, respectively [14]:

$$\gamma_{e,semi/air} = \varepsilon \big/ 4\cdot\alpha_{sp} d\cdot n_{sp}^2 \tag{2.1.5a}$$

$$\gamma_{e,semi/semi} = \varepsilon \big/ 4\cdot\alpha_{sp}\, d \tag{2.1.5b}$$

where ε is the surface effective emittance, and α_{sp} and n_{sp} are the average absorption coefficient and refractive index of the spontaneous emission spectrum. The photon recycling factor can be obtained by the following equation, under the assumption that parasitic absorption can be neglected:

$$\gamma_r = 1-\gamma_{e,\,front}-\gamma_{e,back} \tag{2.1.6}$$

Here γ_r is photon recycling factor, $\gamma_{e,front}$ and $\gamma_{e,back}$ are the photon extraction factors of front and back surfaces.

2.1.3 Results and discussion

This section shows the simulation results using the method described above. All the simulations are done using one-sun AM1.5G solar spectrum, which is the standard for single-junction solar cell characterization.

The effective absorptance is obtained by integrating the wavelength-dependent absorptance over the solar spectrum, where published GaAs refractive indices and absorption coefficients are used [35]. Figure 2.1.2 clearly shows that at a given absorber thickness, Structures A, B, C, and G have much smaller effective absorptance because of the limited number of ray paths inside the solar cell with a smooth front surface or non-reflective back surface (or both). While the other structures have larger effective absorptance because of strong light trapping (i.e., long ray path for absorption due to multiple reflection/scattering) due to textured surface(s) and reflective back surface. Hence, combining textured and reflective back surfaces will enable the use of a much thinner absorber (more than 10 times thinner), while still maintaining sufficient absorption. Furthermore, Structure D, E and F possess almost the same effective absorptance, and Structure D and E are more practical from the device fabrication point of view.

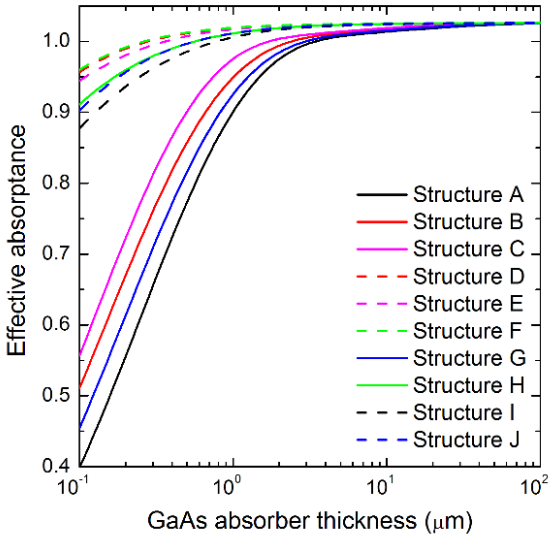

Figure 2.1.2. Effective absorptance versus absorber thickness for the 10 studied GaAs single-junction solar cell structures.

The average generation rate as a function of absorber thickness plotted in Figure 2.1.3 is obtained by dividing absorbed photon flux by the absorber thickness. Although a thicker layer enhances absorption, the average generation rate still decreases with increased absorber thickness. The results show clear evidence that a physically thin layer is required to obtain high excess carrier density, and thus high open-circuit voltage.

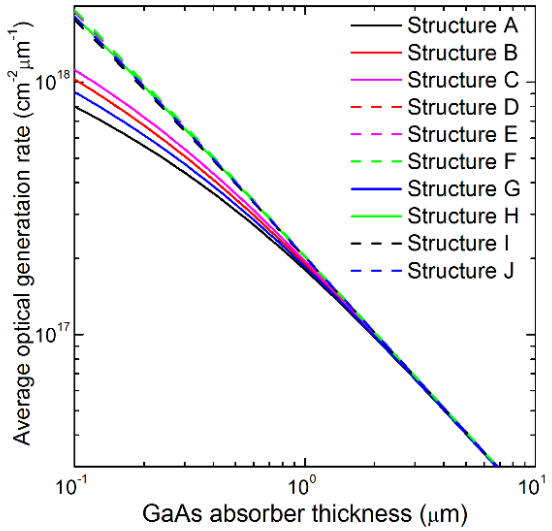

Figure 2.1.3. Average optical generation rate versus absorber thickness for the 10 studied GaAs single-junction solar cells.

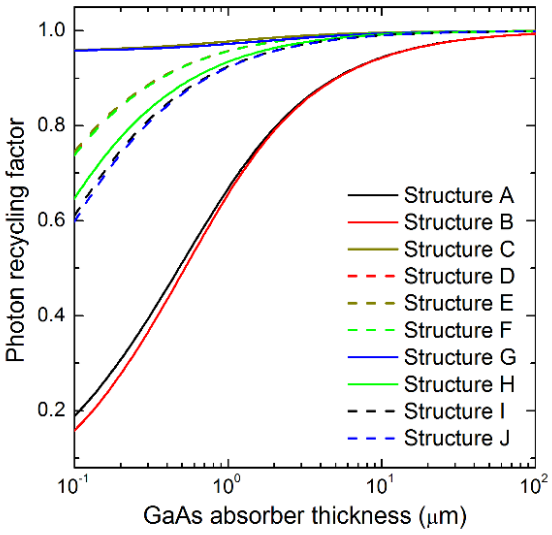

Figure 2.1.4. Photon recycling factor versus absorber thickness for the 10 studied GaAs single-junction solar cells.

Figure 2.1.4 shows the photon recycling factor as a function of absorber thickness for the 10 studied structures. Generally the photon recycling factor increases with absorber

thickness and saturates at large thickness (above 100 μm). At a given absorber thickness, Structure A and B have the lowest photon recycling factor due to the large photon extraction at the index-matched interface between the device and the substrate; Structure C and G have the largest photon recycling factor because of the substrate removal and the highly reflective back surface. The photon recycling factors of Structures D, E, F, H, I and J with textured surfaces are larger than those of Structure A and B due to the reflection at the back surface, but smaller than those of Structure C and G, indicating an enhancement of extraction by surface texturing. A high photon recycling factor with a given absorber thickness is helpful in building up excess carrier density and reaching high open-circuit voltage. However, Structure C and G are not optimal since the absorptance and average generation rate is limited by the short optical paths.

The benefits of using textured surfaces are also clearly revealed in Figure 2.1.5, in which the short-circuit current density is plotted against the number of equivalent light passes in a GaAs single-junction solar cell, with a 300 nm-thick absorber using Structure C and E. No AR coating is assumed here. The number of passes is counted each time the incoming photons reach the back surface of solar cells. The figure shows clearly that 5 passes is sufficient for most of the photons to be absorbed in a 300 nm thick absorber, and the textured back surface improves short-circuit current, at a given absorber thickness, as more photons are absorbed with the photons scattered into large angles. Note that the short-circuit current density is actually an important criterion to evaluate the effectiveness of the back surface scattering and reflection in device design and fabrication. A back surface scattering, which deviates from Lambertian scattering, will have a short-circuit current density between the results of Structure C and Structure E.

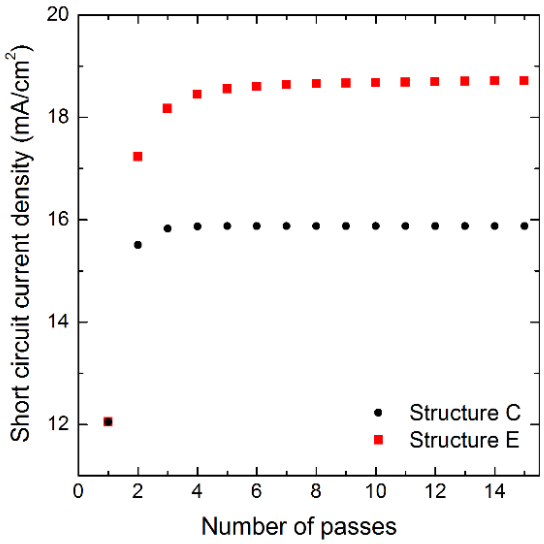

Figure 2.1.5. Short-circuit current density versus number of light passes for GaAs single-junction solar cells with 10 % contact area ratio, and a 300-nm absorber.

The energy conversion efficiencies versus absorber thickness are plotted in Figure 2.1.6. A typical Auger recombination saturation current density per unit length is assumed. Shockley-Reed-Hall recombination saturation current density per unit length, is derived from a published minority carrier lifetime of 3 μs in the literature [36]. Structure A has the lowest efficiency due to large transmission loss from back surface and a short ray path through the absorber. Structure F has the highest peak efficiency of 31.20 % as a result of the large effective absorptance and photon recycling factor within a thin absorber (200 nm).

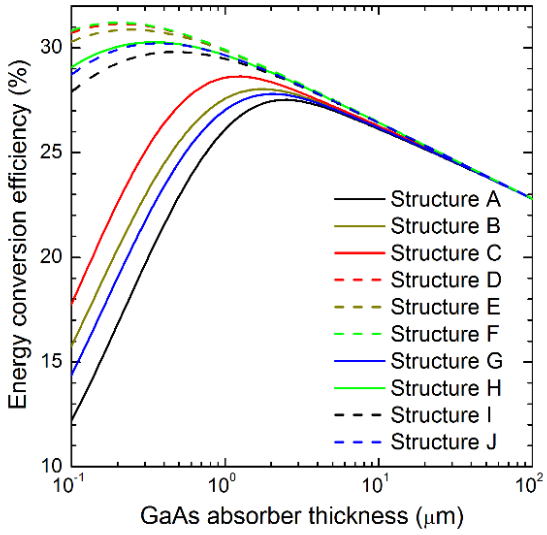

Figure 2.1.6. Energy conversion efficiency versus absorber thickness for the 10 studied GaAs single-junction solar cells.

The modeling results also show that each structure has an optimal absorber thickness, beyond which the energy conversion efficiencies decrease. As the physical thickness of absorber increases, the average generation rate decreases and the probability for carriers to recombine non-radiatively increases, and thus the non-radiative recombination loss. Moreover, spatial relaxation loss, which refers to the energy loss when carriers are swept through device to contacts, also increases due to a larger total potential drop along the device. This optimal thickness is indeed the compromise between maximizing absorption and minimizing non-radiative recombination loss. Figure 2.1.7 below shows the plot of energy conversion efficiency versus absorber thickness of GaAs single-junction solar cells (Structure E). The SRH recombination saturation current density per unit length, J_A/d, is varied to represent different material quality and carrier lifetime. The Auger recombination is assumed to be zero here as it is typical in GaAs. The curve of

J_A/d = 0 represents the case when there is no SRH recombination, from which we can see the efficiency remains constant at maximum value once the absorber is optically thick. However, as the SRH recombination saturation current density increases, that's to say, material quality becomes worse, the maximum efficiency drops due to the increased SRH recombination loss, and the optimal thickness decreases as a thinner layer is required to extract as many carriers as possible before they recombine non-radiatively. This particular example demonstrated the advantage of using a thin absorber when the material is non-ideal (i.e. a material with substantial non-radiative recombination loss).

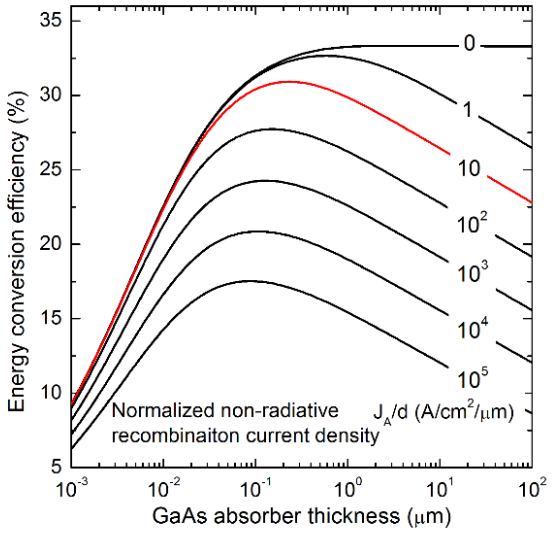

Figure 2.1.7. Energy conversion efficiency versus absorber thickness for GaAs single-junction solar cells using Structure E for various SRH recombination saturation current densities.

Table 2.1 summarizes the calculated device properties (J_{sc}, V_{oc}, FF and efficiency) of the 10 studied GaAs single-junction solar cells at optimal absorber thickness. The optimal absorber thickness is greatly reduced when a textured surface and a reflective back

surface is introduced, while at the same time J_{sc} remains almost unchanged. Consequently, larger V_{oc} and *FF* are achieved as a result of higher excess carrier density, lower SRH and spatial-relaxation losses. Compared with Structure A, Structure F has 1/10 of the absorber thickness and an increased efficiency, V_{oc}, and *FF* by 13.4 %, 8.3 %, and 4.4 %, respectively.

Table 2.1. Summary of simulated device performance for the 10 studied GaAs solar cell structures.

Structure	A	B	C	D	E	F	G	H	I	J
Optimal thickness (μm)	2.51	1.74	1.26	0.21	0.25	0.20	2.00	0.34	0.48	0.36
J_{sc} (mA/cm^2)	31.8	31.8	31.8	31.9	31.8	31.9	31.7	31.7	31.6	31.7
V_{oc} (V)	1.051	1.060	1.100	1.139	1.135	**1.138**	1.079	1.122	1.114	1.118
FF (%)	82.75	83.58	82.22	86.29	85.89	86.38	81.78	85.57	84.99	85.62
η (%)	27.52	28.03	28.64	31.14	30.87	**31.20**	27.79	30.27	29.80	30.22

2.1.4 Summary

Ten types of planar structures with different combinations of smooth, textured, non-reflective, and reflective surfaces are explored for the optimization of the optical design for single-junction GaAs solar cells for record energy conversion efficiency. Calculation of optical properties and device performance is carried out by a semi-analytical model. Both absorptance and photon recycling factor increase with absorbing layer thickness as more

photons can be absorbed/reabsorbed in longer optical paths. However, the average generation rate decreases with absorbing layer thickness. The tradeoff between more absorption and larger average generation rate is one of the reasons why the optimal absorbing layer thickness exists. The combination of textured and reflective surfaces maximizes absorptance at a given absorbing layer thickness and hence provides smallest absorbing layer thickness and largest average generation rate. It is found that with both textured surface and reflective back surface, the conversion efficiency is increased by more than 10 % with only ~10 % absorbing layer thickness. Assuming a minority carrier lifetime of 3 μs for GaAs, Structure F gives maximum achievable efficiency of 31.25 % under one sun AM1.5G solar spectrum. The three absolute percentage point gap between this efficiency and current world record inspires more efforts into research on devices with surface roughness.

2.2 Impact of non-Lambertian back scattering on solar cell performance

Although Lambertian scattering provides the most efficient light trapping, it is a theoretical limit that is difficult to achieve experimentally, and any scattering that deviates from Lambertian will reduce the total optical thickness and result in insufficient photon absorption in the ultra-thin absorber. Hence, it is important to quantify the effectiveness of the light scattering at textured surfaces so that better design guidance, such as the desirable absorber thickness, can be provided to ultra-thin film solar cells for achieving optimal efficiency. In this section we use the semi-analytical model [14] and the Phong distribution [37] to study the impact of non-Lambertian scattering on the optical properties and device performance of GaAs single-junction solar cells with reflective back scattering. The Phong

distribution applied here gives the analytical expressions for the non-Lambertian scattering simulation, which is different than the numerical approach that uses Monte Carlo method [38]. It assumes that the angular light intensity is proportional to $cos^m(\theta)$, where θ is the angle between the scattered light and the surface normal and m is the Phong exponent. Note here that m=1 corresponds to the Lambertian distribution, and higher values of m result in narrower angular intensity distributions, which are expected results for smoother surfaces. Thus the m value is the figure of merit of the scattering effectiveness for a certain textured surface. The figures below show three Phong distributions with m = 1, 5, and 20, clearly showing a narrower distribution with a larger m value.

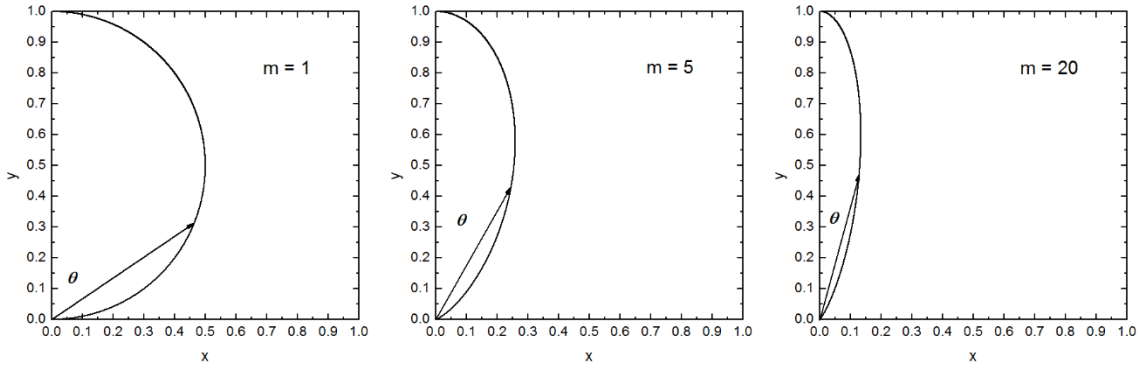

Figure 2.2.1. Illustrations of three Phong distributions with the Phong exponent equals 1, 5, and 20, respectively.

The absorber structure used in the simulation is Structure E, of which the front surface is smooth, and has an ideal AR coating where reflectance is equal to zero, and the back surface is textured and coated with an ideal reflective mirror with unity reflectivity. The textured surface can scatter light into different orders of Phong distributions represented by different Phong components depending on the roughness of the surface.

2.2.1 Optical properties of GaAs absorber

Statistical ray tracing is used to derive the absorptance and emittance of the structure and to calculate the optical properties, assuming Phong scattering events at the textured back surface. Equation (3.1) shows the wavelength-dependent absorptance A_E of the absorber, in which α is the absorption coefficient of GaAs, and d is the absorber thickness.

$$A_E = 1 - e^{-\alpha d} \cdot \frac{t_{E1}}{1 - t_{E2}} \tag{2.2.1}$$

Here t_{E1} and t_{E2} are the fraction of transmitted light in a single pass through the cell and are calculated using (2.2.2) and (2.2.3), respectively; t_{E1} represents the fraction of light within the escape cone, which will exit the device through the front surface, while t_{E2} represents the rest of light that will be totally reflected back (total internal reflection) into the semiconductor and reach the back surface for another scattering event. The count for light pass is incremented each time as the photons reach the back surface where a scattering event occurs.

$$t_{E1} = \frac{2}{t} \cdot \int_0^{\theta_c} e^{-\frac{\alpha d}{\cos\theta}} \cdot \cos^m\theta \cdot \sin\theta \cdot d\theta \tag{2.2.2}$$

$$t_{E2} = \frac{2}{t} \cdot \int_{\theta_c}^{\pi/2} e^{-\frac{2\alpha d}{\cos\theta}} \cdot \cos^m\theta \cdot \sin\theta \cdot d\theta \tag{2.2.3}$$

Here θ is the angle between the scattered light and surface normal, and θ_c is the critical angle of total internal reflection from semiconductor to air at the interface. The Phong distribution is applied so that the fraction of light intensity distributed in solid angle $\sin\theta \cdot d\theta$ is $\cos^m\theta$. The integration is multiplied by a factor of "2" to include all the solid angles, and t is the normalization term as calculated below:

$$t = 2 \cdot \int_0^{\frac{\pi}{2}} cos^m\theta \cdot sin\theta \cdot d\theta \tag{2.2.4}$$

By assuming emittance equals absorptance at equilibrium, the emittance of the absorber can be obtained from the absorptance in the equilibrium case, where the background radiation is incident at all angles. The front surface emittance of the studied structure is expressed as:

$$\varepsilon_{E,\,front} = 1 - t_{E3} \cdot \frac{t_{E1}}{1 - t_{E2}} \tag{2.2.5}$$

where t_{E1} and t_{E2} are explained as above, and t_{E3} is the fraction of transmitted light in the first pass from the front surface to the back surface of the absorber:

$$t_{E3} = 2n_r^2 \cdot \int_0^{\theta_c} e^{-\frac{\alpha d}{cos\theta}} \cdot cos\theta \cdot sin\theta \cdot d\theta \tag{2.2.6}$$

The effective absorptance can be obtained by integrating the wavelength-dependent absorptance over the GaAs absorbing portion of the AM 1.5G solar spectrum:

$$\overline{A_E} = \frac{\int_{E_g - E_u}^{\infty} A_E \cdot n_{sun} \cdot dh\nu}{\int_{E_g - E_u}^{\infty} n_{sun} \cdot dh\nu} \tag{2.2.7}$$

where E_g and E_u are the bandgap and Urbach tail of GaAs, respectively, and n_{sun} is the photon flux of the AM 1.5G solar spectrum. Figure 2.2.2(a) below shows the effective absorptance as a function of absorber thickness for different orders of Phong distributions (different *m* values). It indicates that a stronger absorbing capability can be achieved with a wider scattering distribution (represented by a smaller *m* value), especially when the absorber is thin (below 1 μm). This trend is more clearly illustrated in Figure 2.2.2(b) where the effective absorptance is plotted against the *m* value for several absorber thicknesses. There is a dramatic reduction in absorptance as the *m* value increases from 1 to 40 for the

100 nm absorber, while the magnitude of the subsequent reductions diminishes as the absorber becomes thicker, and eventually the absorptance of the 2 μm absorber remains close to unity regardless of the *m* value. It therefore indicates the necessity of sufficient light trapping only in the case of an ultra-thin solar cell that has a thickness on the order of a few hundred nanometers.

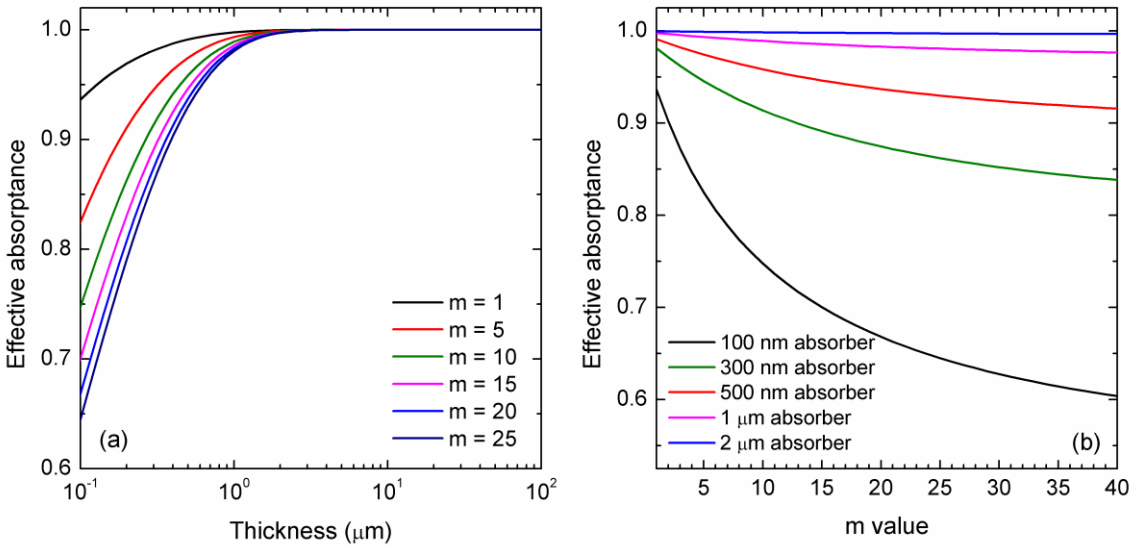

Figure 2.2.2. The effective absorptance of the studied structure versus a) the absorber thickness for different *m* values and b) the *m* value for different absorber thicknesses.

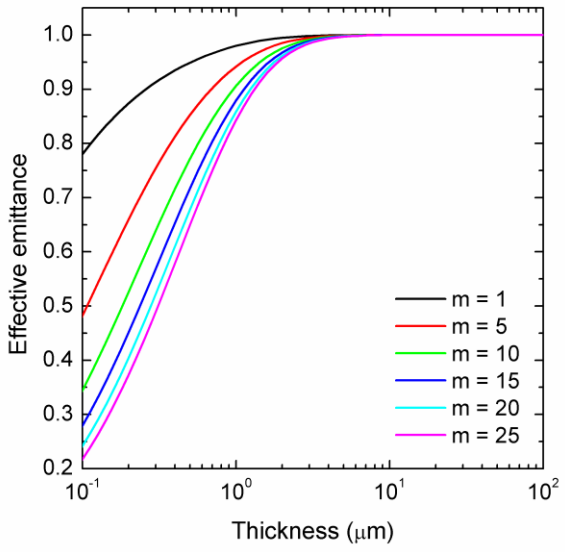

Figure 2.2.3. The effective emittance of the studied structure versus absorber thickness for different *m* values.

The effective emittance can be calculated by normalizing the wavelength-dependent emittance against the spontaneous emission spectrum of the absorber material, and is plotted against absorber thickness in Figure 2.2.3. It follows a trend similar to effective absorptance as a natural result of detailed balance. The larger effective emittance for the case with a smaller m value at certain absorber thickness indicates a stronger light extraction for a rougher back surface. Moreover, the photon extraction factor, γ_e, defined as the fraction of spontaneously emitted photons that are extracted out of the absorber into the air, can be calculated using the following equation [14]:

$$\gamma_e = \varepsilon / (4 \cdot \alpha_g d \cdot n_g^2) \tag{2.2.8}$$

where, ε is the surface effective emittance, and α_g and n_g are the average absorption coefficient and refractive index of the spontaneous emission spectrum. The photon recycling factor, γ_r, defined as the fraction of spontaneously emitted photons that are

reabsorbed by the absorber, is calculated using (2.2.9) under the assumption that parasitic absorption can be neglected. Note the photon extraction factor of the back surface is zero for the studied structure due to the highly-reflective mirror.

$$\gamma_r = 1 - \gamma_{e,\,front} - \gamma_{e,back} \tag{2.2.9}$$

Figure 2.2.4(a) shows the front surface photon extraction factor versus absorber thickness for the studied structure. It is obvious that the extraction factor is larger for thinner absorbers and smaller for thicker absorbers due to the photon recycling effect, and the extraction factor will reach the value of zero for an infinitely thick absorber. The photon recycling factor as a function of absorber thickness is shown in Figure 2.2.4(b), where reverse trends are observed.

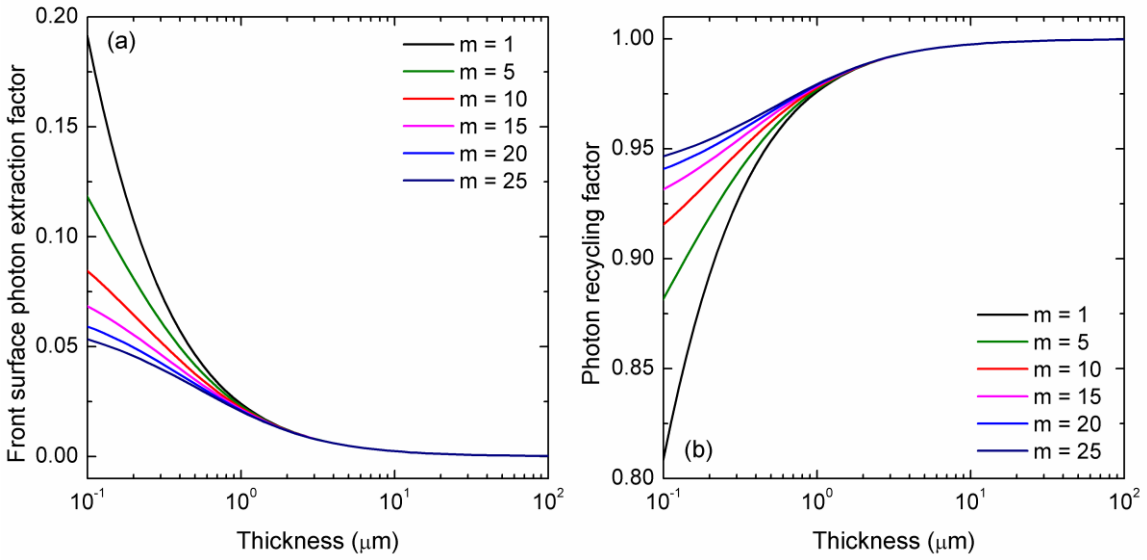

Figure 2.2.4. (a) The front surface photon extraction factor and (b) the photon recycling factor of the studied structure versus absorber thickness for different *m* values.

The large difference in the photon extraction factors, as well as the photon recycling factors, for different orders of Phong distributions (different *m* values) at thinner absorber

thicknesses can be explained by the following comparison. Consider two slab absorbers: one has a smooth back mirror while the other has a textured back mirror that can scatter light into a Lambertian distribution. Both absorbers have the same thickness that is below 300 nm, and both mirrors are ideal with a reflectivity of unity. The spontaneously emitted photons can be reflected between the two surfaces before finally being extracted or reabsorbed. Hence for the textured absorber, every time the photons reach the back surface where a scattering event happens, they are redistributed into a Lambertian distribution and those photons within the escape cone will be extracted if they reach the front surface afterwards. For the slab absorber with smooth surfaces however, the spontaneously emitted photons outside the escape cone will never be redistributed into the escape cone and extracted into the air before they are reabsorbed. The extraction factor of the textured surface is therefore larger than that of the smooth surface due to a larger total amount of escaped photons.

2.2.2 Device performance of GaAs single-junction solar cell

This section shows the device performance of a GaAs single-junction solar cell with reflective back scattering calculated using the semi-analytical model. The simulation assumes a SRH recombination lifetime of 3 μs and an Auger recombination coefficient of 8.66×10^{-31} cm^6/s from a published source [36]. The power conversion efficiency versus absorber thickness plots for different orders of Phong distributions (different *m* values) are shown in Figure 2.2.5(a). The optimal absorber thicknesses shown in the plots are attributed to the trade-off between maximizing the absorption and minimizing the non-radiative recombination. It is noticed that as the surface becomes rougher (*m* value

decreases), a higher "maximum efficiency" can be achieved with a thinner absorber due to the enhanced light trapping capability. The optimal thickness increases as the surface becomes smoother (*m* value increases), because a thicker absorber is necessary to guarantee sufficient absorption of solar radiation. The convergence of all the curves beyond a thickness of 2 μm indicates that no light scattering is necessary for very thick absorbers.

Figure 2.2.5(b) shows the power conversion efficiency versus *m* value for absorbers with various thicknesses. It is clear that the thinner absorbers are more sensitive to the scattering effectiveness than the thicker ones: the efficiency drops from ~30 % to ~20 % as the *m* value increases from 1 to 25 for the 100 nm absorber, while that of the 2 μm absorber remains ~28 % regardless of the variation of the *m* value. This figure also provides the design guidance of the absorber thickness based on the scattering effectiveness of the textured surface. A thinner absorber is more beneficial when the scattering is closer to Lambertian, while a thicker absorber would be required to achieve sufficient absorption in the case of poor scattering effectiveness.

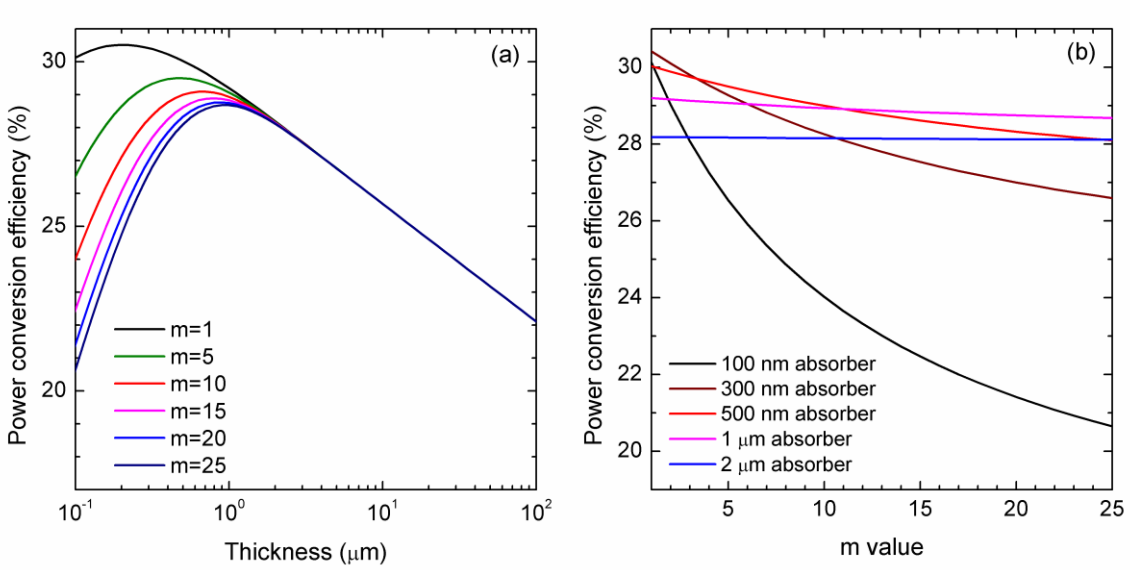

Figure 2.2.5. The power conversion efficiency of the studied structure versus a) the absorber thickness for different *m* values and b) the *m* value for different absorber thicknesses.

It should be noted that the V_{oc} is much less dependent on the scattering effectiveness of the textured surface than the J_{sc}, although strong scattering can enhance the photon density greatly and thus the V_{oc}. However, the SRH recombination, instead of radiative recombination, dominates the total recombination under normal solar cell operating conditions, and the variation of the Phong distribution doesn't change the total recombination greatly.

2.2.3 Summary

A semi-analytical model and Phong distribution have been used to explore the impact of non-Lambertian scattering on the optical properties and device performance of GaAs single-junction solar cells. The absorptance is strongly enhanced with a scattering closer to the Lambertian case compared to a higher order of Phong distribution at an

absorber thickness below 1 μm. It also indicates that the thinner the absorber is, the more dependent the absorptance is on the scattering effectiveness of the textured surface. The modeling results also show stronger light extraction with rougher surfaces, (smaller *m* values) especially for thinner absorbers, which therefore have smaller photon recycling factors compared to absorbers with smoother surfaces. The optimal thickness of the device shifts to larger values and the maximum efficiency drops as the surface becomes smoother (larger *m* values). The efficiency of a thinner cell is found to be more dependent on the scattering effectiveness, which results from the dependence of J_{sc}; however, the V_{oc} remains almost constant for different orders of Phong distributions due to the domination of non-radiative recombination under a normal one-sun condition.

2.3 Ultra-thin GaAs single-junction solar cell with reflective back scattering

Although Structure F shown in the previous section gives the highest efficiency, it is very hard to fabricate textures on both sides of the solar cells, and utilizing textured surfaces in GaAs-based single- or multi-junction solar cells for light management has not been reported in the literature. The reason for this is mainly due to the fact that the absorbers in those cells usually have large absorption coefficients and are therefore very thin with a typical thickness of only a few microns, resulting in difficulties in making textures on their surfaces. Additionally, it is known that roughening the absorber directly will lead to huge surface/interface recombination. On the other hand, the GaAs substrate is not transparent

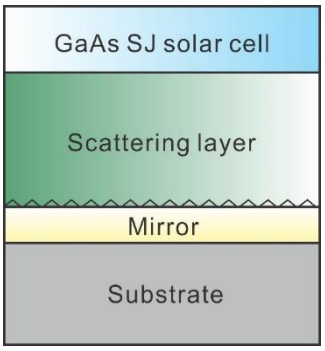

Figure 2.3.1. Schematic structure of the single-junction GaAs solar cell integrated with a reflective back scattering layer.

to the part of the sunlight to be absorbed by the cell, so it is still necessary to remove the substrate and deposit a highly reflective mirror on the backside of the solar cell to achieve high efficiency. Therefore, Structure E, which can be obtained by integrating the solar cell with a back scattering layer coated with a reflective mirror (shown in Figure 2.3.1), is the most practical design.

2.3.1 Design of the back scattering layer

In the design shown above, the textures are applied on the thick (5 μm) scattering layer surface so that the GaAs absorber will not be impacted, and the fabrication of those textures remains feasible as well. The absorptance of this structure can then be expressed as:

$$A_E \cong 1-e^{-\alpha d}+e^{-(\alpha d+\alpha_{scatter} d_{scatter})}\frac{t_{11}+t_{21}-t_{12}-t_{22}}{1-t_f} \tag{2.3.1}$$

where α and $\alpha_{scatter}$ are absorption coefficients of absorber and scattering layer, respectively; d and $d_{scatter}$ are thicknesses of absorber and scattering layer, respectively. Term t is the fraction of transmitted light at different surface/interface(s) in a single pass through the cell. Therefore, t_{11}-t_{12} and t_{21}-t_{22} are the fractions of the light absorbed in the absorber in a single pass, in and out of the escape cone, respectively.

$$t_{11}=\int_0^{\theta_c} e^{-\alpha_{scatter} d_{scatter}/\cos\theta}\cdot 2\cos\theta\sin\theta\cdot d\theta \tag{2.3.2a}$$

$$t_{12}=\int_0^{\theta_c} e^{-(\alpha d+\alpha_{scatter} d_{scatter})/\cos\theta}\cdot 2\cos\theta\sin\theta\cdot d\theta \tag{2.3.2b}$$

$$t_{21}=\int_{\theta_c}^{\frac{\pi}{2}} e^{-\alpha_{scatter} d_{scatter}/\cos\theta}\cdot 2\cos\theta\sin\theta\cdot d\theta \tag{2.3.2c}$$

$$t_{22} = \int_{\theta_c}^{\frac{\pi}{2}} e^{-(2\alpha d + \alpha_{scatter} d_{scatter})/\cos\theta} \cdot 2\cos\theta \sin\theta \cdot d\theta \tag{2.3.2d}$$

$$t_f = \int_{\theta_c}^{\frac{\pi}{2}} e^{-2\cdot(\alpha d + \alpha_{scatter} d_{scatter})/\cos\theta} \cdot 2\cos\theta \sin\theta \cdot d\theta \tag{2.3.2e}$$

It is required that the material of the back scattering layer should be wide-bandgap to reduce the parasitic absorption, as well as lattice-matched to GaAs to minimize misfit dislocation density. The effective absorptance of GaAs single-junction solar cells integrated with reflective back scattering layers, made of several different III-V materials ($Al_{0.50}In_{0.50}P$, $Al_{0.80}Ga_{0.20}As$, $Al_{0.59}Ga_{0.41}As$, $Ga_{0.50}In_{0.50}P$), are plotted against absorber thickness in Figure 2.3.2. It clearly shows that when absorber thickness is smaller than 1 μm, the solar cells with back scattering layers made of wider bandgap materials have larger effective absorptance. Using an $Al_{0.50}In_{0.50}P$ back scattering layer offers the largest absorptance as a result of it having the largest bandgap among the four candidates. When the absorber thickness is larger than 1 μm, the effective absorptance is almost identical for all types of back scattering layers as the high-energy photons are already fully absorbed in the first pass through the absorber, and the parasitic absorption loss in the back scattering layer is therefore negligible. The efficiency-thickness plots in Figure 2.3.3 demonstrate that the cell integrated with $Al_{0.50}In_{0.50}P$ reflective back scattering layer gives the highest efficiency.

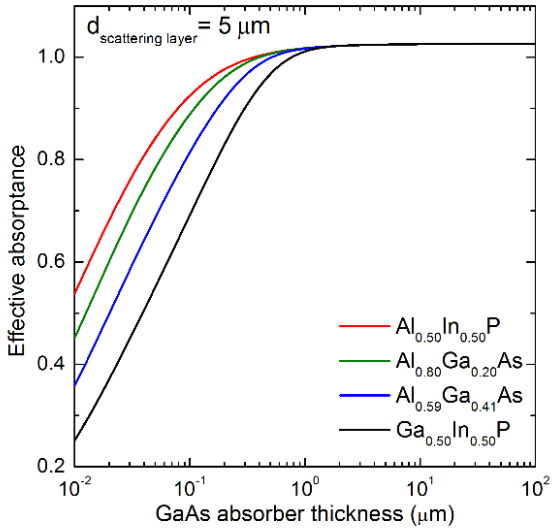

Figure 2.3.2. Effective absorptance versus absorber thickness for GaAs single-junction solar cells integrated with four types of reflective back scattering layers.

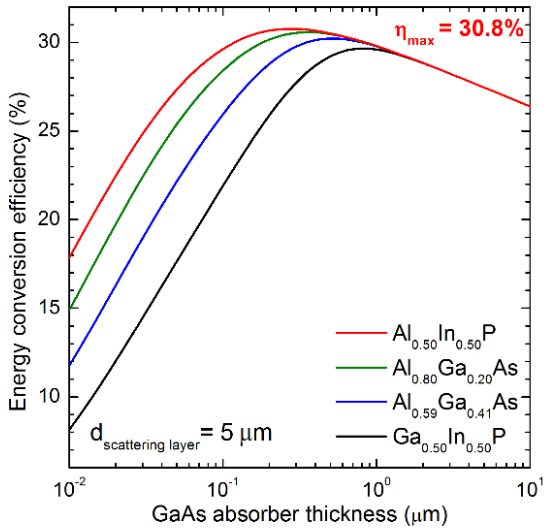

Figure 2.3.3. Energy conversion efficiency versus absorber thickness for GaAs single-junction solar cells integrated with four types of back scattering layers.

2.3.2 Design of the backside mirror

Potential candidates for the backside mirror include Au, Ag and Al, of which the reflectivities in the spectrum range from 250 nm to 900 nm are shown in Figure 2.3.4. The

reflectivity of Al remains close to or above 0.9 throughout the whole spectrum, however, it is not as large as those of Au and Ag in near-infrared (NIR) range. Due to the fact that the photon flux in visible and NIR range is larger than that in UV range, and photons with high energy are unlikely to reach the backside mirror due to large absorption coefficient of GaAs absorber, it is expected that Ag and Au mirrors have less reflection loss than Al mirror. Moreover, the reflection loss of Ag mirror should be less than that of Au mirror as a result of its much larger reflectivity in the spectrum range from 350 nm to 450 nm.

Figure 2.3.5 shows the effective absorptance as a function of absorber thickness for the three different mirrors. Ag mirror is the best with least reflection loss, Au mirror is the second best, and Al mirror is the worst. A few data points are listed in Table 2.2 for detailed comparison. The three curves merge eventually when the absorber thickness is larger than 10 μm, as no photons will reach the backside mirror and thus the reflection loss is zero for all three cases.

Note the discussion here is about the reflectivity at an air/metal interface instead of a semiconductor/metal interface, which doesn't represent the case here accurately. A correction is discussed in Section 2.3.3.1.

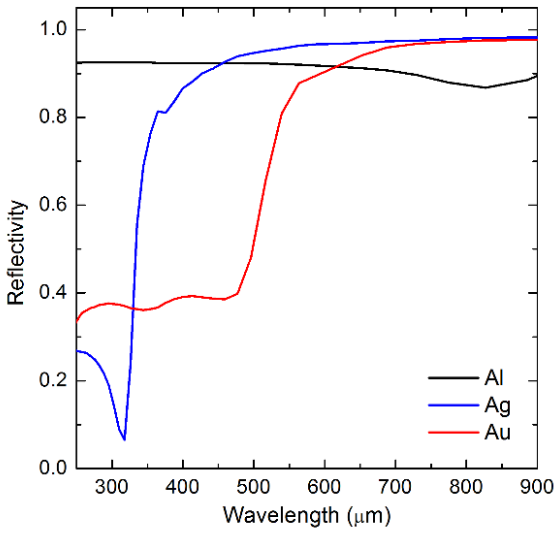

Figure 2.3.4. Reflectivity of Al, Ag, and Au.

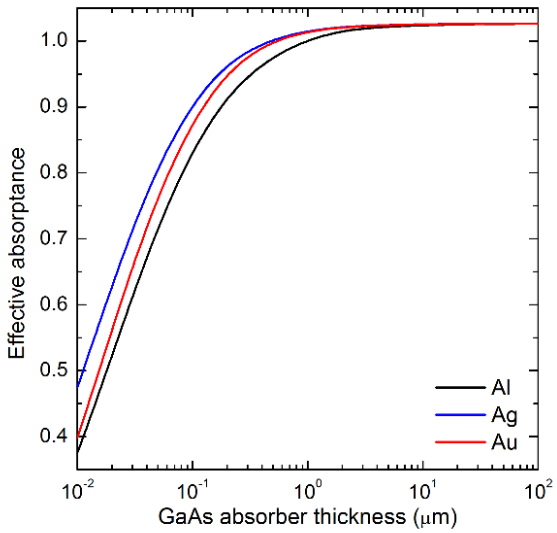

Figure 2.3.5. Effective absorptance versus absorber thickness of GaAs single-junction solar cells integrated with AlInP back scattering layer and Al, Ag and Au mirrors.

Table 2.2. Comparison of effective absorptance at different absorber thicknesses and using different mirrors.

	Effective absorptance			
	100 nm	300 nm	1000 nm	2000 nm
Al mirror	0.830	0.945	1.003	1.014
Au mirror	0.872	0.974	1.013	1.020
Ag mirror	0.900	0.983	1.014	1.021

2.3.3 Design of the MgF_2/ZnS double-layer anti-reflection coating

This section discusses the transfer matrix method in calculating the reflectance of a multi-layer structure, and the optimization of a double-layer anti-reflection coating using this method.

2.3.3.1 Anti-refection coating optimization for ultra-thin solar cells

The simplest optimization of the AR coating is usually done by calculating the quarter-wavelength-thickness of AR coating layers at ~ 600 nm, at which point the photon flux of the solar spectrum reaches its maximum. A more accurate method should use transfer matrix and the energy-dependent refractive index to calculate the total reflectance over the entire spectrum. Moreover, the wide bandgap window layer in solar cells usually has a thickness on the order of 10 nm and a smaller refractive index than that of the absorber. It is therefore necessary to take the window layer into account in the reflectance calculation. In the ultra-thin GaAs single-junction solar cells, the absorber thickness is on the order of a few hundred nanometers and it is anticipated that the absorber thickness will affect the optimization of the AR coating design as well. This section shows the calculated

reflectance of MgF_2/ZnS double-layer AR coating for ultra-thin GaAs single-junction solar cells by taking into account the window layer, ultra-thin absorber, and BSF layer.

2.3.3.2 Reflectance calculation method

The transfer matrix method is used to calculate the reflectance and to optimize the MgF_2/ZnS double-layer AR coating design for ultra-thin GaAs single-junction solar cells. The formula of the normal incidence case is expressed as follows [39]:

$$\begin{bmatrix} a \\ b \end{bmatrix} = \begin{bmatrix} p_0 & -1 \\ p_0 & 1 \end{bmatrix} \left(\prod_{j=1}^{n} \begin{bmatrix} \cos\delta_j & -ip_j^{-1}\sin\delta_j \\ -ip_j\sin\delta_j & \cos\delta_j \end{bmatrix} \right) \begin{bmatrix} 1 \\ p_{n+1} \end{bmatrix} \tag{2.3.3}$$

$$\delta_j = \frac{2\pi}{\lambda_0} N_j d_j \tag{2.3.4}$$

where the subscripts from 0 to n+1 represent air, n-layer structure (includes some or all of the following layers: AR coating, window, absorber, and BSF), and substrate, respectively; δ_j is the optical phase change of j_{th} layer, d_j is the layer thickness, and N_j is the energy-dependent complex refractive index that equals $n_j + ik_j$; p_j equals N_j for TE waves and $1/N_j$ for TM waves. Considering sunlight is unpolarized, the energy-dependent spectral reflectance is given by:

$$R(h\nu) = 0.5 \cdot \left| \frac{a_{TE}}{b_{TE}} \right|^2 + 0.5 \cdot \left| \frac{a_{TM}}{b_{TM}} \right|^2 \tag{2.3.5}$$

The energy-independent total reflectance is defined by the following formula:

$$R_e = \frac{\int_{E_g}^{\infty} R(h\nu) \cdot N_{sun}(h\nu) \cdot dh\nu}{\int_{E_g}^{\infty} N_{sun}(h\nu) \cdot dh\nu} \tag{2.3.6}$$

where N_{sun} ($h\nu$) is the photon flux per unit energy of AM1.5G solar spectrum; the lower limit of the integration is the bandgap of the absorber in the solar cell.

The structures investigated in this work are shown in Figure 2.3.6. Structure I consists of a MgF_2/ZnS double-layer AR coating directly deposited on top of GaAs substrate. Structure II features a 30 nm thick GaInP window layer inserted between the GaAs substrate and the ZnS layer. Structure III represents the ultra-thin GaAs single-junction solar cells with a thick AlInP back scattering layer, in which the GaAs absorber is only 300 nm thick and sandwiched by two 30 nm GaInP films as window and BSF layers.

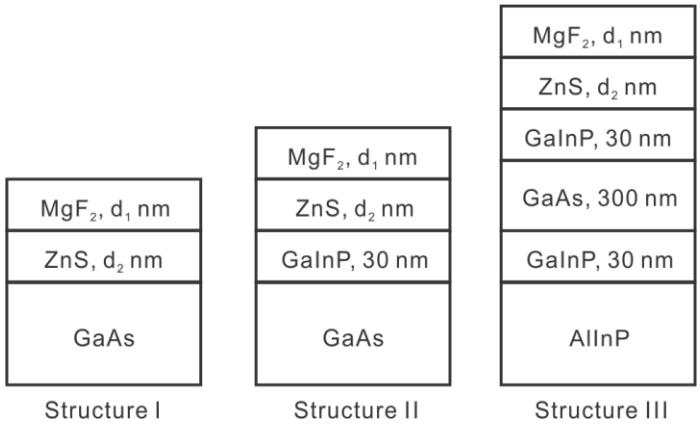

Figure 2.3.6. Three structures for the optimization of MgF_2/ZnS anti-reflection coating on GaAs thin-film solar cells.

The front surface total reflectance of the three structures are calculated and compared using the method described above and the experimental values of the energy-dependent refractive indices [35][40] (shown in Figure 2.3.7). Thicknesses of MgF_2 and ZnS layers are scanned simultaneously and the total reflectance of each combination is calculated using (2.3.3) to (2.3.6). The thickness combination with minimum total reflectance is chosen as the optimal design. This optimization method can provide more

accurate results since energy-dependent refractive indices and total reflectance over the absorbed solar spectrum, instead of refractive index and reflectance at one specific wavelength, are used.

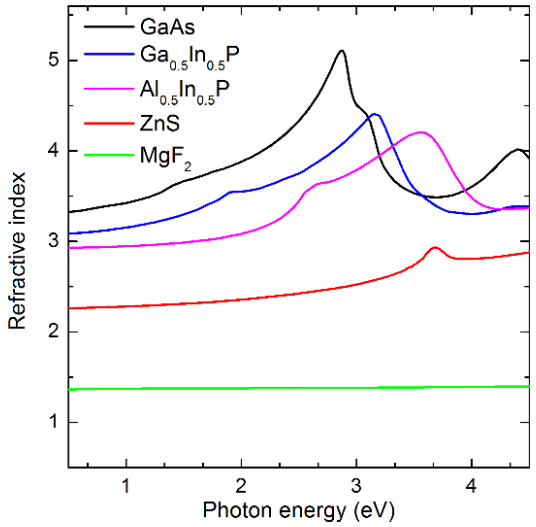

Figure 2.3.7. Refractive indices of the materials used in the anti-reflection coating design.

2.3.3.3 Results and discussions

Figure 2.3.8 shows the simulated total reflectance contours of the three structures plotted against MgF_2 and ZnS thicknesses. The optimal designs are denoted in the figures by the grey dots and also summarized in Table 2.3. For Structure I, the minimum total reflectance of 3.10 % is obtained with a 93 nm MgF_2/51 nm ZnS pair. When a GaInP window layer is considered, the optimized thicknesses of the MgF_2 and ZnS layers are shifted to 96 nm and 48 nm, respectively, and the minimum total reflectance decreases to 1.49 %. This is because the refractive index of GaInP is slightly lower than that of GaAs, and thus the window layer provides a better refractive index gradient from air to the GaAs absorber. The minimum total reflectance of Structure III is slightly larger than that of

Structure II as the GaInP layer and the AlInP substrate underneath the GaAs absorber have smaller refractive indices, and thus are inverse to the index gradient. However, the difference is only ~ 0.1 % absolute percentage due to the similar refractive indices of these III-V materials over the absorbed spectrum.

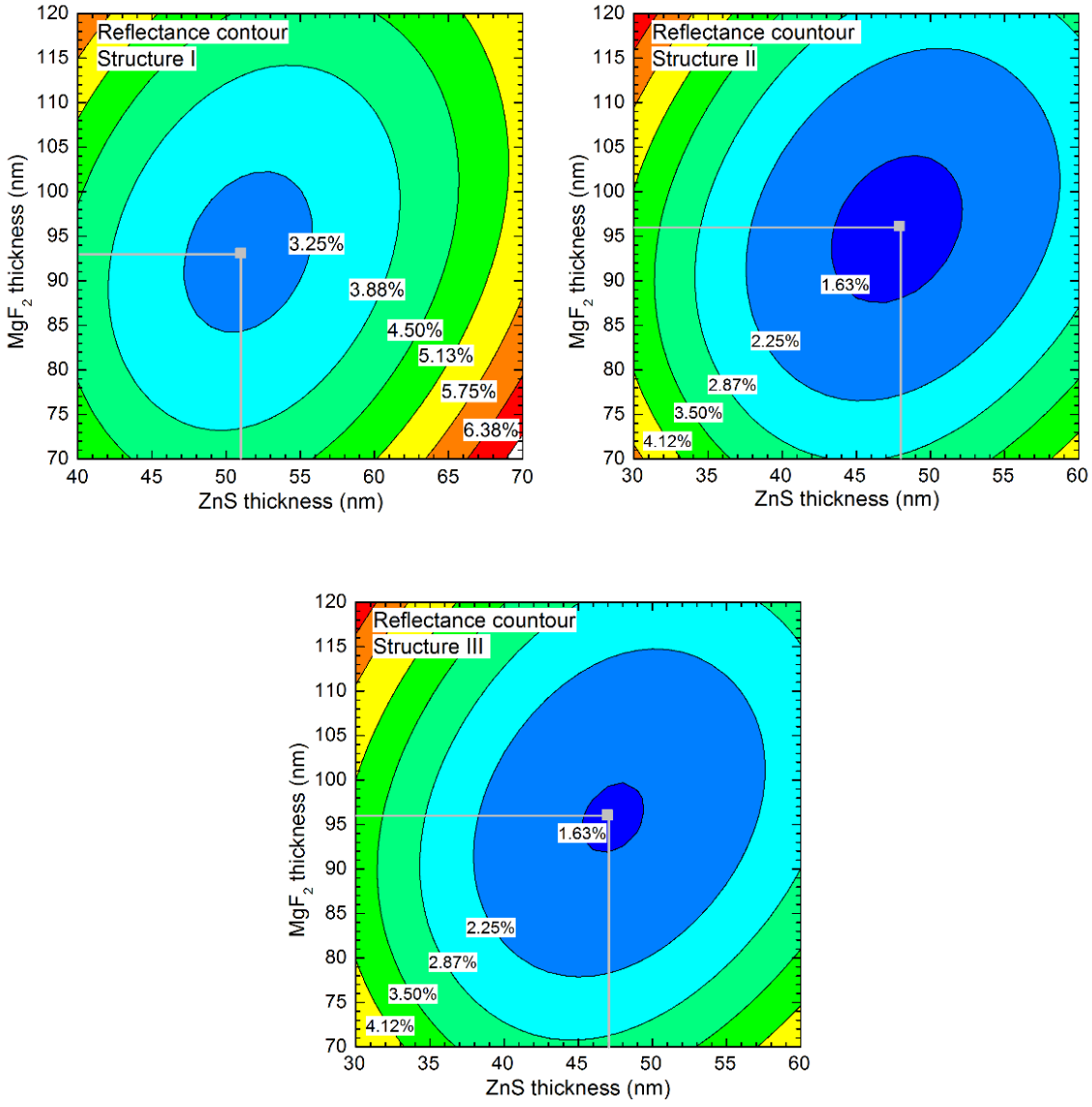

Figure 2.3.8. Simulated reflectance contours of the three structures

Table 2.3. Summary of the optimal designs of the three AR coating structures

Structure	d_MgF_2 (nm)	d_ZnS (nm)	Total reflectance (%)
I	93	51	3.10
II	96	48	1.49
III	96	47	1.60

The simulated reflectance spectra of the three optimized designs (shown in Figure 2.3.9) remain below 5.0 % in the energy range below 2.5 eV, and increases significantly to above 25 % at 3.5 eV. This is due to the visible and NIR ranges having a larger weight in the optimization due to the much larger photon flux in those spectral ranges, compared with that in the UV range. It is clearly shown that the spectral reflectance of Structure II and III is smaller than that of Structure I over almost the entire absorbed spectrum, resulting in their smaller total reflectance.

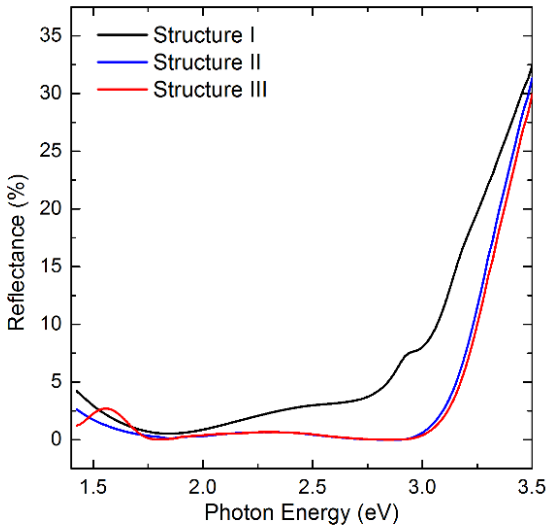

Figure 2.3.9. Simulated reflectance spectra of the optimal AR coating designs of the three structures.

2.3.4 Analysis of the 300 nm GaAs solar cells with reflective back scattering

The detailed device layer structure of the recently demonstrated ultra-thin GaAs single-junction solar cell with reflective back scattering is shown in Figure 2.3.10. It features a GaAs absorber with a thickness of 300 nm, a textured $Al_{0.52}In_{0.48}P$ layer for back scattering and a highly reflective Au mirror. This structure can potentially reach a high $V_{oc,}$ as a result of a larger equivalent internal electric field that improves carrier extraction and reduces SRH recombination in the ultra-thin absorber, while maintaining sufficient absorption of solar radiation through effective light trapping. The detailed design and fabrication process can be found in previously published papers [27][41].

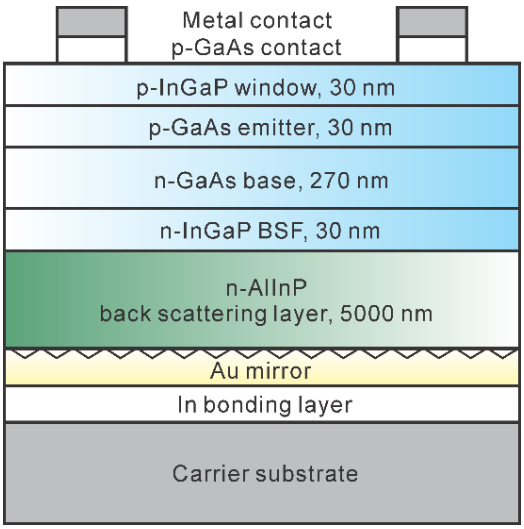

Figure 2.3.10. Schematic layer structure of the finished device.

The measured performance of the fabricated device, in comparison with the best achievable performance, is summarized in Table 2.4. The device is measured with a J_{sc} of 24.5 mA/cm^2, a V_{oc} of 1.00 V, a *FF* of 77.8 %, and a power conversion efficiency of 19.1 %. The predicted best achievable performance is modeled based on the assumptions of

Lambertian scattering on the back side of the cell, a back mirror with 100 % reflectivity, an AR coating with 2 % reflectance, a 2 % top contact grid coverage, the optimal material quality with the longest published minority carrier lifetime, and no series resistance or shunt.

Table 2.4. Comparison between the modeled best achievable and the measured device performance.

	J_{sc} (mA/cm^2)	V_{oc} (V)	FF (%)	η (%)
Modeled best achievable	30.7	1.13	85.4	29.5
Measured	24.5	1.00	77.8	19.1
Δ	6.2	0.13	7.6	10.4

The measured device performance, including J_{sc}, V_{oc} and FF, is noticeably smaller than the predicted best achievable values. The lower measured J_{sc} is attributed to the non-unity reflectivity of the Au mirror and the non-Lambertian scattering in the actual device, in addition to the 3.8 % AR coating reflection loss and 9.7 % contact grid coverage. The former two factors are carefully examined by using the method discussed above. Additionally, the smaller V_{oc} and FF are attributed to non-radiative recombination and series resistance, which will be discussed in the last part of this section.

2.3.4.1 Non-unity reflectivity at $Al_{0.52}In_{0.48}P$/Au interface

The reflectivity of a textured mirror is different from that of a smooth one, and the reflectivity of the semiconductor/Au interface is different from that of the air/Au interface, both of which may affect the light trapping property. Thus, it is important to use an

averaged angle-independent reflectivity of the textured Au mirror attached to the $Al_{0.52}In_{0.48}P$ scattering layer to model the properties of the studied device. The angular reflectivity of $Al_{0.52}In_{0.48}P$/Au interface is calculated by using the Fresnel equation and the complex refractive indices of $Al_{0.52}In_{0.48}P$ and Au [35][40]. The result is then averaged against the Phong distribution to get the average angle-independent reflectivity:

$$\overline{R_m} = \frac{\int_0^{\pi/2} R(\theta) \cdot \cos^m\theta \cdot \sin\theta \cdot d\theta}{\int_0^{\pi/2} \cos^m\theta \cdot \sin\theta \cdot d\theta} \tag{2.3.7}$$

where $\overline{R_m}$ is the averaged reflectivity of the textured Au mirror with an m^{th} order Phong distribution, $R(\theta)$ is the angle-dependent reflectivity, θ is the angle between surface normal and reflected beam, and m is the Phong exponent. The reflectivity spectra for various Phong distributions are shown in Figure 2.3.11, which indicates a larger reflectivity for a rougher surface that can scatter more light into large angles. However, the difference becomes smaller in the wavelength range beyond 600 nm, and even negligible near the GaAs absorption edge, and thus will not affect the absorption of the 300 nm absorber greatly. The relatively large difference in the wavelength range below 600 nm will also have a negligible impact on the absorption property as these photons have absorption depths much shorter than 300 nm, and thus will be mostly absorbed before they reach the back surface.

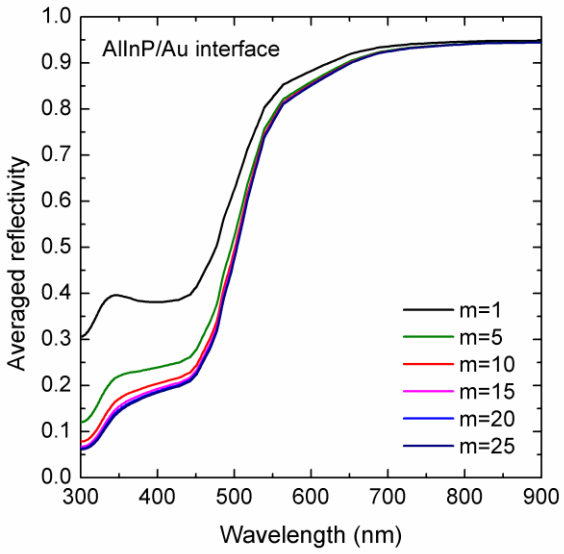

Figure 2.3.11. The averaged reflectivity at the textured $Al_{0.52}In_{0.48}P$/Au interface for different *m* values.

Furthermore, the reflectivities of the textured $Al_{0.52}In_{0.48}P$/Au and the air/Au interfaces are compared in Figure 2.3.12, where the assumption of Lambertian scattering is applied. The averaged reflectivity of the $Al_{0.52}In_{0.48}P$/Au interface at the GaAs absorption edge is calculated to be 95 %, while that of the air/Au interface is 98 %. The lower reflectivity of the $Al_{0.52}In_{0.48}P$/Au interface is due to the larger refractive index of $Al_{0.52}In_{0.48}P$ compared to air, and thus will result in increased photon absorption loss in the mirror.

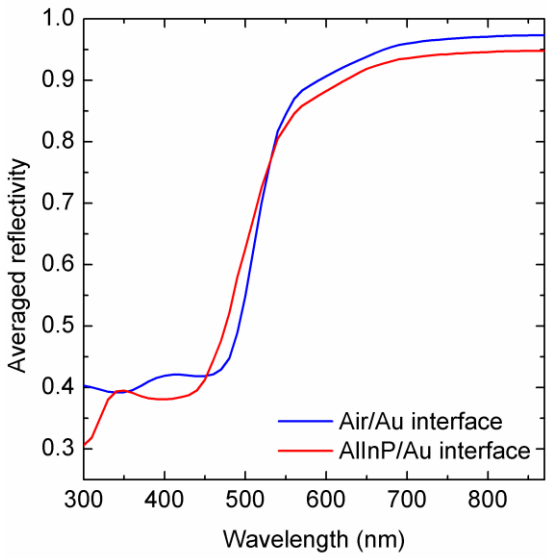

Figure 2.3.12. Comparison between the averaged spectral reflectivity of the air/Au and $Al_{0.52}In_{0.48}P$/Au interfaces.

2.3.4.2 Non-Lambertian scattering at the back surface

The non-Lambertian back scattering that deviates from Lambertian can be described by using the Phong distribution as discussed above. In this section the absorptance and J_{sc} of the 300 nm thick GaAs solar cell are simulated with the following factors considered: 1) the experimentally measured reflectance of the AR coating; 2) the real device structure that consists of a 300 nm thick GaAs absorber and 5000 nm thick $Al_{0.52}In_{0.48}P$ scattering layer; 3) the m^{th} order Phong distribution; and 4) the textured Au/AlInP mirror reflectivity that corresponds to the m^{th} order Phong distribution. The absorptance and J_{sc} can then be calculated by using an equation modified from Equation (1). Note that the parasitic absorption loss in the $Ga_{0.51}In_{0.49}P$ window layer is ignored at this stage due to the following reasons: 1) the thickness of the layer is relatively thin (30 nm) compared to that of the GaAs absorber and $Al_{0.52}In_{0.48}P$ scattering layer; and 2) the depletion region of the GaAs PN junction might extend into the window layer, and will

help to collect the photo-generated carriers in it. It is shown in Figure 2.3.13 that J_{sc} decreases from ~27 mA/cm^2 to ~23 mA/cm^2 as the *m* value increases from 1 to 40, which represents that the scattering is gradually deviating from the Lambertian distribution. The *m* value of the Phong distribution in the device is determined to be 12 by fitting the modeled J_{sc} to the experimental results.

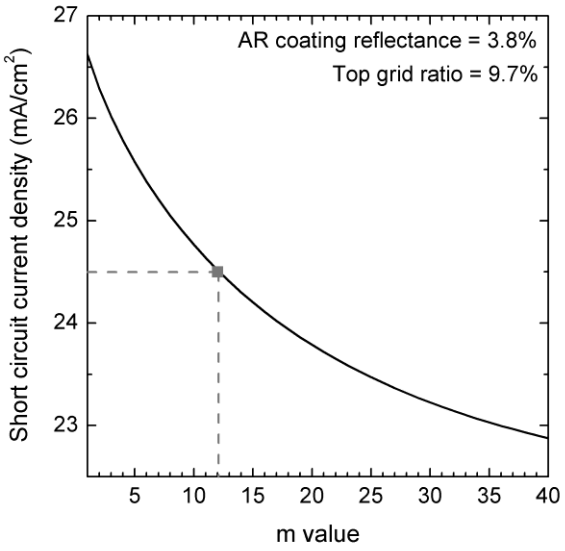

Figure 2.3.13. Simulated short-circuit current density as a function of the Phong exponent *m* and the comparison with experimental result.

The impact of non-Lambertian scattering on the external quantum efficiency (EQE) of the device is shown in Figure 2.3.14. Only the wavelength range from 600 nm to the GaAs absorption edge is considered here, as the photons with higher energy will be mostly absorbed during their first pass through the absorber. The solid curves represent the simulated EQE spectra, with the measured AR coating reflectance and the calculated textured $Al_{0.52}In_{0.48}P$/Au interface reflectivity considered. The near IR response decreases as the Phong exponent *m* increases, indicating a reduced light trapping due to the narrower

scattering distribution. The measured EQE spectrum is plotted as a dashed line in the figure. By comparing the near IR part of the simulated and measured EQE, the Phong exponent *m* is also determined to be ~10 to 15, which is in good agreement with the fitting discussed above.

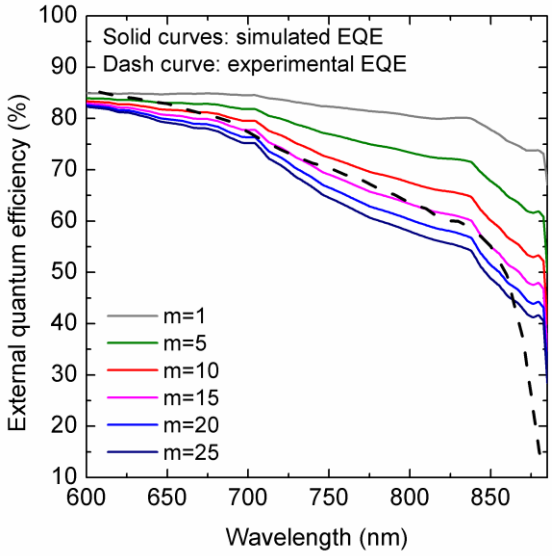

Figure 2.3.14 .Comparison between simulated and experimental external quantum efficiency spectra.

2.3.4.3 Non-radiative recombination and series resistance

Table 2.4 also shows deviations of experimental V_{oc} and *FF* measurements from the modeled best achievable values. The factors that will affect the V_{oc} of a GaAs solar cell include: cell geometry, material quality, and surface/interface quality. A substantial non-radiative recombination in the bulk and at the surface/interface can dramatically reduce the V_{oc}. Figure 2.3.15 shows the plot of V_{oc} versus non-radiative recombination lifetime for the studied structure. Note this recombination is an average effect of both SRH and surface/interface recombination. The plot clearly shows that V_{oc} increases rapidly in the

region where non-radiative recombination lifetime is below 100 ns, and gradually saturates at its theoretical limit when the lifetime reaches infinity. The grey dot shows where the simulated and experimental V_{oc} overlap and indicates a non-radiative recombination lifetime of ~130 ns in the studied device.

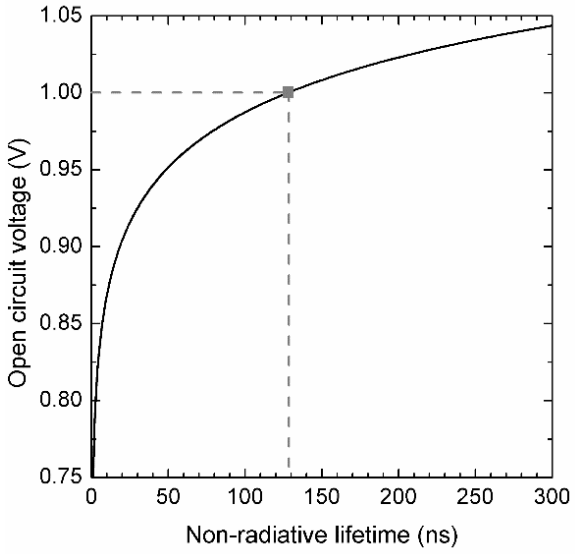

Figure 2.3.15. Simulated open-circuit voltage as a function of non-radiative recombination lifetime and its comparison with experimental value.

The impact of series resistance on the I-V characteristics of the solar cell is studied using the single diode equivalent circuit model, which is shown in Figure 2.3.16. In this model, the solar cell is treated as a combination of a current source, a diode, a series resistance and a shunt resistance. Here I_L represents the photo current generated by solar absorption, I_D and V_D represent the diode current and voltage, I_{sh} represents the shunt current which is usually due to surface/sidewall leakage, R_{sh} and R_s represent shunt and series resistance, respectively, and I and V are the current and voltage of the whole device.

The relationships of these parameters are shown by the equations below, from which the light *I*-*V* curve of the solar cell can be calculated.

$$I = I_L - I_D - I_{sh} \tag{2.3.8a}$$

$$V = V_D - I R_s \tag{2.3.8b}$$

$$I_{sh} = V_D / R_{sh} \tag{2.3.8c}$$

$$I_D = I_0 \times e^{\frac{qV_D}{nkT}} \tag{2.3.8d}$$

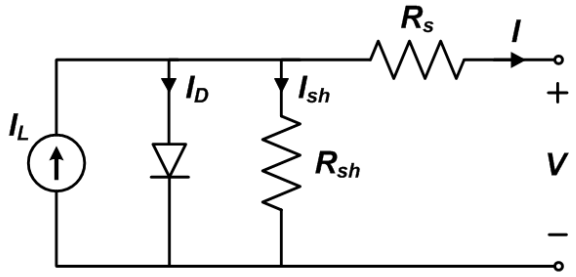

Figure 2.3.16. The schematic of the single diode equivalent circuit model for solar cells.

It is found that the *FF* decreases linearly when the specific series resistivity increases, as shown by the plot in Figure 2.3.17. By fitting the experimental *FF* of 77.8 %, the specific series resistivity of the device is determined to be 1.2 Ω·cm^2 (grey dot in the figure).

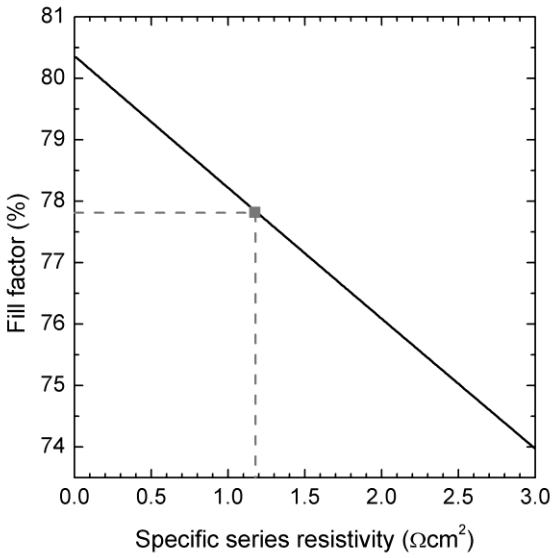

Figure 2.3.17. Simulated fill factor as a function of specific series resistivity (0.01 to 3 $\Omega \cdot cm^2$) and its comparison with experimental value.

2.3.5 Summary

The backscattering layer, back reflective mirror, and AR coating have been designed for the 300 nm GaAs single-junction solar cells. Wide-bandgap $Al_{0.5}In_{0.5}P$ alloy and Ag have been found to be the best candidates for the scattering layer and mirror. A novel transfer matrix method, which takes into account of multiple thin layers in the solar cell structure, gives the optimal AR coating of 96 nm MgF_2 / 48 nm ZnS.

The device performance of the 300 nm GaAs single-junction solar cell is analyzed using the theory developed in section 2.2. Calculations show a reduced averaged reflectivity of 95 % for the $Al_{0.52}In_{0.48}P$/Au interface near the GaAs absorption edge for the Lambertian scattering case, compared to the value of 98 % for the air/Au interface. The Phong exponent of the non-Lambertian scattering at the back surface is determined to be ~12 by fitting both the simulated J_{sc} and EQE to experimental values. A non-radiative recombination lifetime of ~130 ns, and a specific series resistivity of 1.2 $\Omega \cdot cm^2$ are

determined by fitting the simulated and measured V_{oc} and FF, respectively. The efficiency of the ultra-thin GaAs single-junction solar cell can be further improved by enhancing the reflective back scattering layer using dielectric material, reducing non-radiative recombination using material with better quality or a compositional gradient window layer, and improving the current spreading in the device.

CHAPTER 3

SINGLE-CRYSTALLINE CDTE-BASED MATERIALS FOR PHOTOVOLTAIC APPLICATIONS

This chapter talks about the research work on single-crystalline (Mg)Cd(Zn)Te/MgCdTe double heterostructure (DH) grown by molecular beam epitaxy (MBE) for photovoltaic applications. For the growth part, the fundamentals of MBE is introduced, with its key features that are essential to high-quality epitaxial growth explained. The growth conditions and procedures of CdTe on InSb are described in details, as well as the growth rate and flux ratio calibrations. After that, two projects on improving the minority carrier lifetime in CdTe are discussed. The first project focuses on using a lattice-matched CdZnTe alloy on InSb to maintain a low defect density in a thick CdTe/MgCdTe DH; the second project focuses on carefully examining the interface recombination mechanism of various CdTe/MgCdTe DH structures and the dependence of interface recombination velocity on barrier height and width. The demonstration of ~1.7 eV MgCdTe alloys is presented in the last part, of which the characterization results indicate that MgCdTe is suitable for II-VI/Si tandem solar cell applications.

3.1 Molecular beam epitaxial growth of CdTe on InSb (100) substrates

In the first section of this chapter, the growth of CdTe on InSb using MBE is discussed in details, including the fundamentals of MBE, the detailed growth procedures of CdTe on InSb substrates, and the growth rate and flux ratio calibrations.

3.1.1 Fundamentals of Molecular Beam Epitaxy

MBE is an epitaxial process by which growth of materials takes place under UHV conditions on a heated crystalline substrate, by the interaction of adsorbed species supplied by atomic or molecular beams [42]. By "epitaxial" it means the grown layers have the same crystalline structure and their lattice constants differ from that of the substrate by no more than 10 %. As a growth technique that can produce high quality single-crystalline material, it features several advantages compared to other techniques: 1) UHV; 2) heated substrate; 3) atomic/molecular beams; 4) various *in-situ* characterizations.

The UHV is usually achieved by multi-stage pumping that involves several types of pumps working at different regimes. A commercially available pumping station that includes an oil-free mechanical pump and a molecular turbo pump can pump the chamber down to 10^{-5} Torr ~ 10^{-6} Torr, and then the pumping source is switched to cryopump, ion pump, sublimation pump, etc. An additional liquid-nitrogen filled cryo-panel in the chamber provides another pumping source, and the ultimate background pressure of an MBE chamber can thus be down to 10^{-11} Torr. Such low pressure can minimize the impurities in the chamber. On the other hand, the UHV environment brings the growth to the molecular regime, as opposite to the vapor-phased deposition techniques such as metal-organic chemical vapor deposition (MOCVD). In the "molecular regime" the mean free paths of the atoms and the molecules is larger or comparable to the critical lengths of the growth chamber, thus the atoms and the molecules can reach the substrate without interacting with each other. A direct consequence is that the beams can be controlled abruptly by the shutters which results in accurate monolayer control of the growth and abrupt interfaces.

The substrate heating is critical to provide sufficient surface migration of the absorbed atoms and desorbing the excess atoms to maintain a stoichiometric surface. Insufficient heating leads to the forming of poly-crystalline and even amorphous films, while overheating will evaporate the incoming atoms/molecule flux and even the substrate materials. This is why there is a growth temperature window for a specific material. Typically GaAs can be grown at around 560 ℃ with a window of 40 ℃. However, the temperature window for II-VI growth is usually smaller, for example, the growth temperature window for high-quality HgCdTe is as small as 4 ℃. The heating also allows for thermal oxide removal of the substrates prior the growth, which is proven to provide a better surface for epitaxial growth compared to using chemical etching to remove the oxide.

The atomic/molecular beams are generated by heating the source materials in effusion or valved cracker cells, which are facing towards the substrate. The flux of the beam is tuned by either changing the temperature of the effusion cell, or valve of the valved crackers. To minimize the impurity levels in the grown materials, the purities of the source materials are usually on the order of 6N to 7N. The table below lists the typical purities for the MBE-grade source materials.

Table 3.1. Typical purities of MBE-grade source materials

Material	Purity	Material	Purity
Al	99.99995 %	Cd	99.99999 %
Ga	99.999999 %	Be	99.999 %
In	99.99999 %	Mg	99.9999 %
As	99.999995 %	Zn	99.99999 %
Sb	99.99999 %	Te	99.99999 %
P	99.99999 %	Se	99.9999 %

A MBE system usually features several *in-situ* characterization techniques. A residual gas analyzer is usually used to monitor the partial pressures of different gases in the chamber, such as H_2, N_2, O_2, H_2O, CO_2, Ar, and so on. It provides information of the chamber cleanliness, helps to check for the vacuum leak, and keeps track of the flux levels during growth. Another important technique is reflected high energy electron diffraction (RHEED), which monitors the diffraction pattern of a high energy electron beam that is incident on the substrate at a glancing angle. The high energy of the electron and the glancing incident angle ensures that the electron can only penetrate a few monolayers of the substrate, so the surface morphology and reconstruction are monitored. A smooth surface is usually indicated by streaky RHEED patterns and a failed growth is usually indicated by spotty RHEED patterns. Another important way of utilizing RHEED is the growth rate calibration by RHEED intensity oscillation. It has been found that usually the zeroth order of the diffraction peak intensity oscillates as the growth continues, and one period of the oscillation corresponds to the growth of one monolayer material. This method is used in this study and details of the growth rate and flux ratio calibrations are shown in section 3.2.3.

The MBE machine used in this study is a dual-chamber VG V80H system equipped with separate III-V and II-VI growth chambers connected by an UHV transfer chamber (Figure 3.1.1). Such a design allows for III-V/II-VI integration while preventing cross contamination. The III-V chamber is equipped with Al, Ga, and In effusion cells; P, As, and Sb valved crackers; a Bi valved effusion cell; and a triple-doping cell that contains Si, Be, and Te. The II-V chamber is equipped with Cd, Be, Zn and Mg effusion cells; Te and

Se valved effusion cells; and two triple-doping cells. The heating station is used for wafer outgassing before being transferred to the growth chambers.

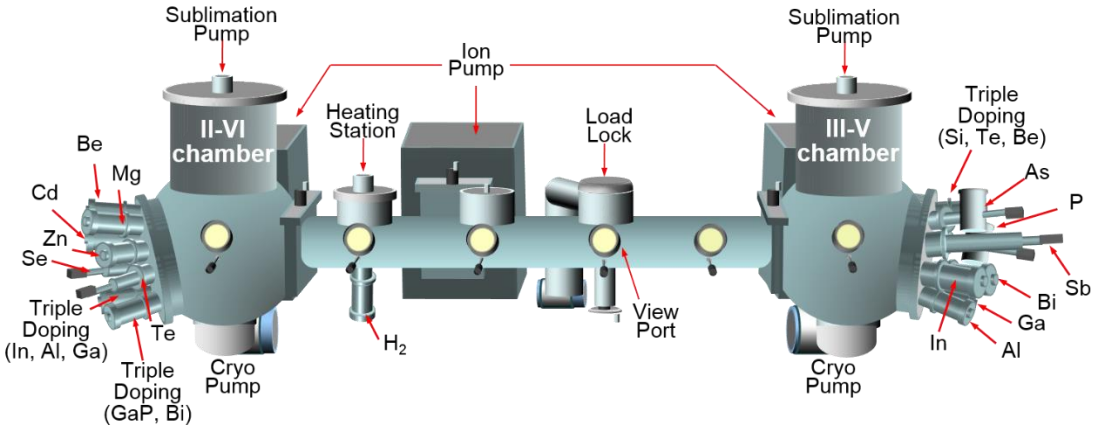

Figure 3.1.1. Schematic diagram of the VG V80H MBE system used in this study.

3.1.2 Growth procedures

All the samples are grown on InSb (001) substrates using the dual-chamber VG V80H MBE system. The oxide removal process of InSb starts with an initial substrate temperature ramp to a thermocouple reading of 500 ℃ at 25 ℃/min. Then the temperature is further ramped up at a slower rate of 5 ℃/min in a 5 ℃ interval, with a 3-min pause after each ramp to prevent the substrate from being overheated, until it reaches a pyrometer reading of 475 ℃ ~ 480 ℃. The reason for such a careful temperature ramp is that the InSb oxide removal temperature is very close to the InSb melting point. The substrates are kept at the temperature for one hour and the completion of oxide removal is then indicated by the streaky pseudo-(1×3) RHEED reconstruction patterns [43]. The RHEED patterns at different stages of the thermal oxide removal process are shown in the figures below. As the substrate temperature is ramping up, streaky RHEED patterns appear at $T_{sub} \approx 424$ °C (Figure 3.1.2 (a) and (b)), and then becomes spotty as the temperature is further ramped to

about 460 ℃ (Figure 3.1.2 (c)). This interesting phenomena is referred to as two-stage oxide removal: Sb_2O_5 and In_2O_3 [43]. Finally, a streaky pseudo-(1×3) and c(4×4) pattern is observed representing an oxide-free InSb surface (Figure 3.1.2 (d)-(e)).

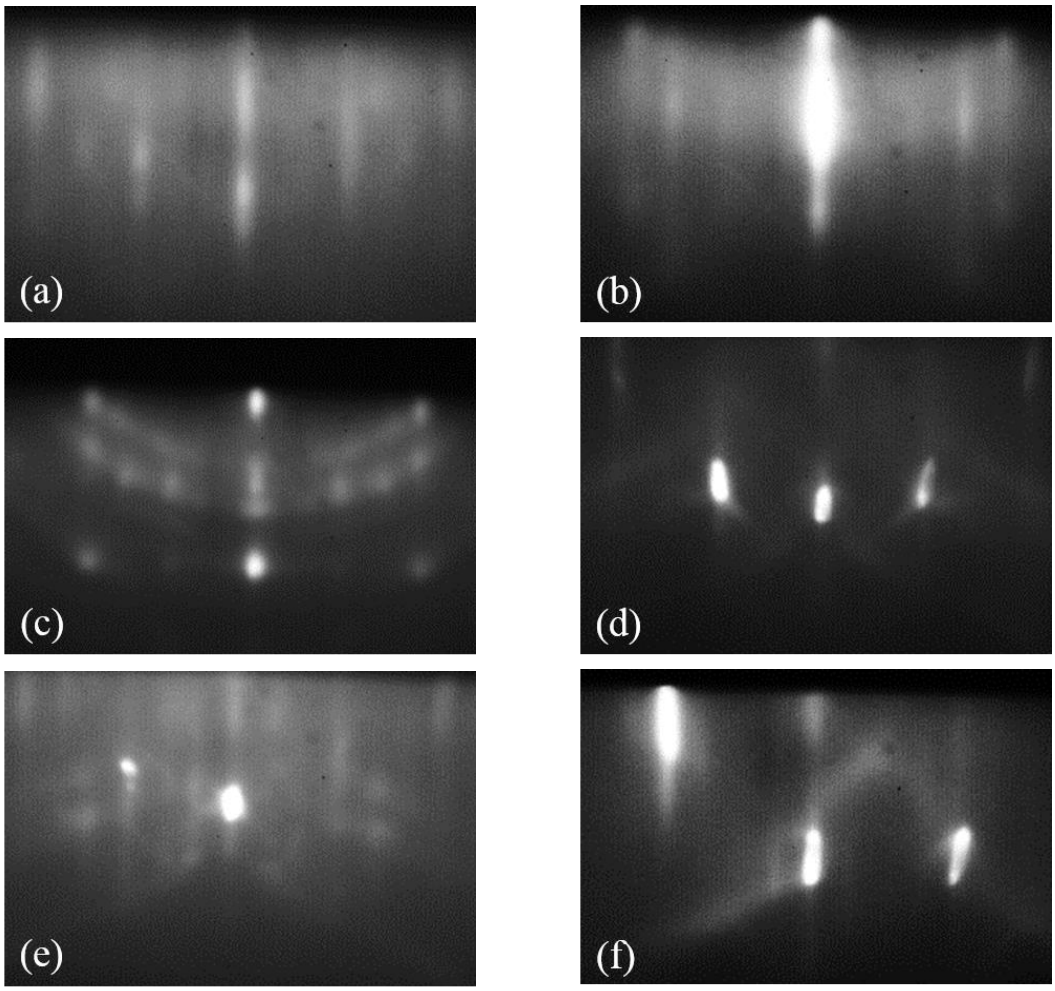

Figure 3.1.2. RHEED reconstruction patterns during the thermal oxide removal of InSb (100) substrate: (a)-(b) streaky patterns at $T_{sub} \approx 424$ °C indicating the removal of Sb_2O_5; (c) spotty semi-ring pattern at $T_{sub} \approx 460$ °C indicating a rough surface during the removal of In_2O_3; (d)-(f) streaky pseudo-(1×3) and c(4×4) reconstruction patterns after the oxide removal showing a surface ready for MBE growth.

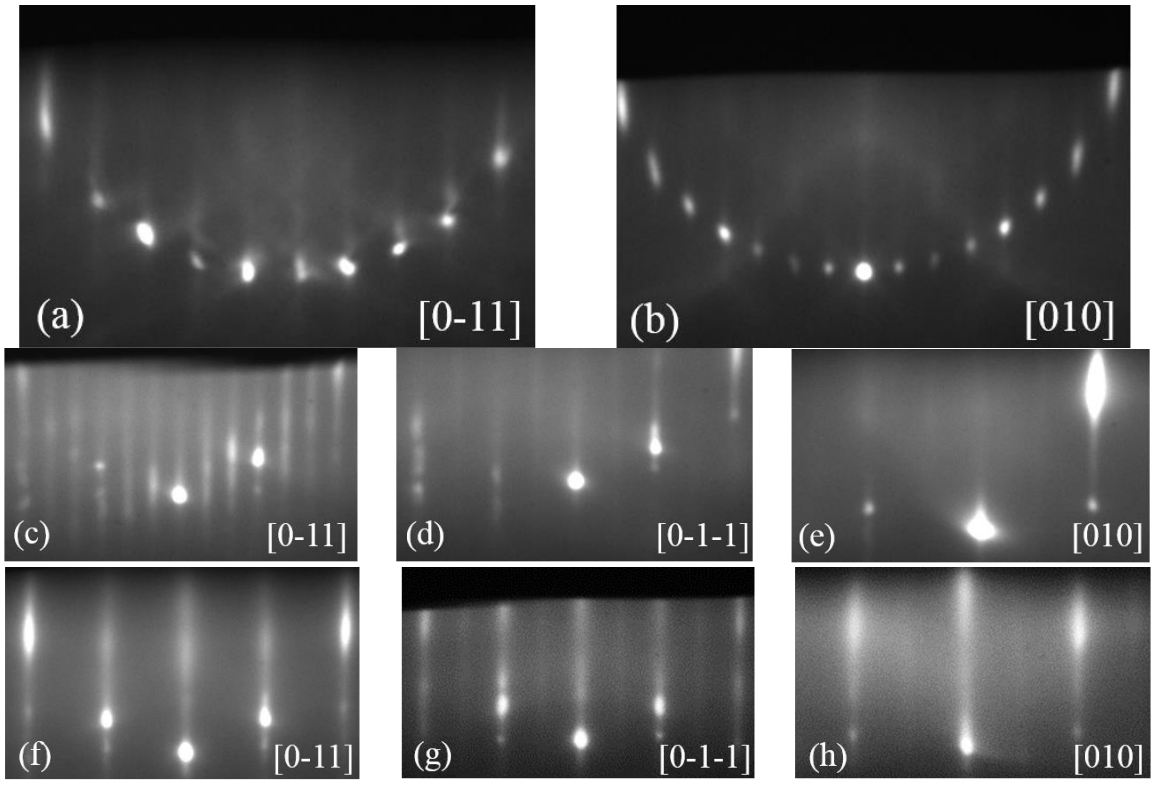

Figure 3.1.3. RHEED reconstruction patterns in the CdTe growth: (a)-(b) streaky (2×2) and c(4×4) patterns right after the direct transfer from III-V chamber to II-VI chamber; (c)-(e) streaky (2×3) and c(2×2) patterns when InSb substrate is exposed with Cd flux; (f)-(h) streaky (2×1) and c(2×2) reconstruction patterns after the CdTe has been grown for 10 minutes.

After the oxide removal, the substrate temperature is brought down to 390 ℃ for the 500 nm InSb buffer growth, with a growth rate of 10.8 nm/min and a Sb/In flux ratio of 1.5. The samples are transferred to the II-VI chamber under UHV, which avoids surface oxidation and contamination. The surface remains high quality after the transfer as indicated by the streaky RHEED patterns. Immediately prior to CdTe growth, InSb surfaces are exposed to a Cd flux for several minutes to prevent the formation of a group III-VI alloy at the interface. Meanwhile the RHEED pattern changes to a (3×2)

reconstruction. A CdTe buffer layer is then grown using an initial Cd/Te flux ratio of 3.0 in order to further prevent the formation of In_3Te_2 at the interface. After two minutes of growth, the flux ratio is then reduced to 1.5. Upon initiation of CdTe growth on InSb, the RHEED pattern becomes slightly hazy as the surface reconstruction transitions from InSb to CdTe. After 10 minutes of growth the pattern becomes streaky. Both (2×1) and $c(2\times2)$ RHEED reconstructions are observed which indicate a Cd-rich growth condition. The initial substrate temperature prior to the growth is set to 280 ℃ (pyrometer reading), and as the II-VI layer is deposited the temperature gradually decreases to ~265 ℃ due to the emissivity change of the wafer surface. The growth temperature and Cd/Te flux ratio has been optimized in previous study by DiNezza et al [44].

3.1.3 Growth rate and flux ratio calibrations

One beauty of MBE is its capability of precisely controlling the layer thickness, material composition, and doping profile, which makes it particularly useful for applications in electronic and optoelectronic devices. Thus, it is essential to have accurate and repeatable calibrations of the growth rates and flux ratios. In this section, the methods of calibrating the growth of InSb and CdTe will be discussed in details.

3.1.3.1 InSb growth rate and Sb/In flux ratio calibrations

As is known, III-V compound semiconductor growth is preferably carried out under a group-V rich condition to maintain high quality stoichiometric growth. Hence, the growth rate of the III-V compound is limited by the group-III flux, and a reasonable sequence is calibrating the group-III flux that leads to the growth rate, followed by calibrating the V/III

flux ratio. Here we will use InSb as a feasibility demonstration, and this method works for other III-V binary growth calibrations

The Indium flux is measured using an ion gauge in terms of ion current as a function of cell thermocouple temperature, as shown in Figure 3.1.4 (a). The curve is then converted to growth rates versus temperature, based on a calibration point near the typical growth rate for InSb grown on InSb. The determination of the growth rate can be carried out using RHEED oscillation, which however, may not be accurate enough in some cases when the oscillation dampens rapidly, or the signal-to noise ratio is poor. A more accurate way to determine the growth rate is by growing InAs/InAsSb superlattice and measuring the period thickness using X-ray diffraction (XRD).

The calibration curves are parameterized using an exponential fitting function (equation (3.2.1)) that serves as a lookup function in the control software to set the effusion cell temperatures for the desired growth rates. T is the cell temperature, m_1 and m_2 are fitting parameters, and G_0 is the pre-factor that is adjusted to reflect the changes in the growth rate for different substrate lattice constants, and the cell depletion using subsequent single temperature calibrations. A fitted calibration curve is shown in Figure 3.1.4 (b).

$$G = G_0 \times exp\left[\frac{m_1}{m_2} \times \left(1 - \frac{m_1}{T}\right)\right] \tag{3.2.1}$$

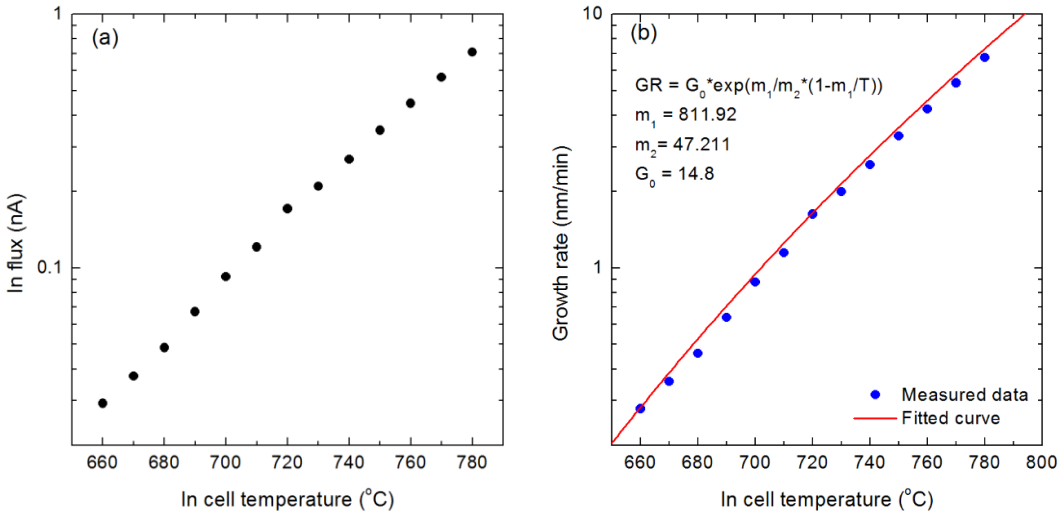

Figure 3.1.4. (a) Flux versus temperature for Indium cell; (b) growth rate versus temperature for Indium cell.

The Sb flux is first measured in terms of ion current as a function of valve position, with the Sb bulk zone set at a thermocouple temperature that provides the desired range of Sb flux over the operating range of the valve. The Sb/In flux ratio is then calibrated against the Indium flux by determining the minimum amount of Sb flux required to maintain a smooth Sb terminated growth surface, for a given In growth rate at a given growth temperature. This calibration point is indicated by the change of RHEED pattern from pseudo-(1×3) to (4×2) as seen in Figure 3.1.5, and is defined as the one-to-one Sb to In flux ratio (Sb/In = 1). The valve calibration curve is then scaled proportionally to ion current to provide an effective Sb flux curve as a function of valve position (see Figure 3.1.6). A fifth order polynomial fitting is applied so that the calibration curve can be parameterized. The flux ratio is regularly calibrated during the growth campaigns, and the temperatures of the Sb bulk zones are adjusted to compensate for the depletion of the bulk

Sb materials. This calibration method has the advantage that the group-V flux curves can be expressed in the same units as those of the group-III growth rate curves, such as monolayers per second, as functions of valve position and bulk source temperature. Furthermore, in this approach, the Sb calibration curves rely on a precise growth condition rather than an arbitrary ion gauge current or pressure reading, which changes with time due to the coating of the ion gauge and varies from gauge to gauge and system to system, thus providing reproducible control of the Sb flux over time.

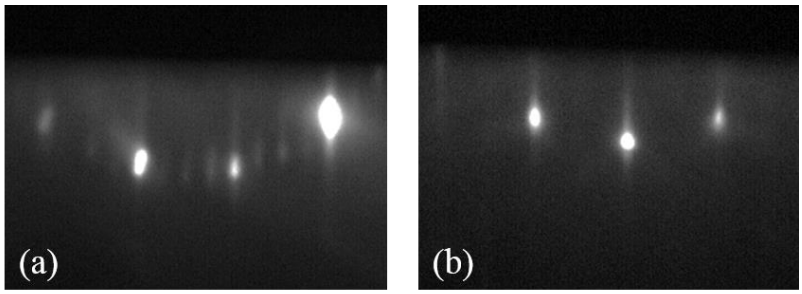

Figure 3.1.5. RHEED patterns of In-rich InSb surface: (a) 4× pattern; (b) 2× pattern.

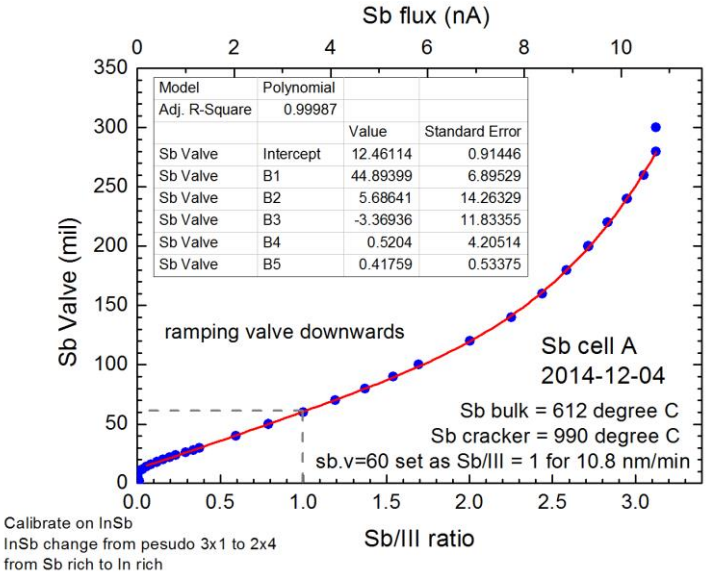

Figure 3.1.6. Sb/In flux ratio calibration curve, where the blue dots are measured data and red solid line is the fifth order polynomial fitting curve.

3.1.3.2 CdTe growth rate and Cd/Te flux ratio calibrations

The growth of II-VI materials is very different from that of III-V materials: (1) the growth temperature is typically more than 200 ℃ lower than that of III-V materials due to their higher vapor pressure; (2) the growth can be carried out under both group-II rich and group-VI rich conditions. The second point enables the calibration of both group-II and group-VI growth rates by RHEED oscillation.

Prior to the growth rate calibration, a CdTe buffer layer is grown on InSb for 30 minutes using the procedures mentioned above to ensure a smooth surface. The intensity of the zeroth order diffraction peak along the (0-1-1) direction is monitored by a camera and recorded by the KSA 400 software. The RHEED oscillation can be initiated by operating the Cd shutter, and typically about 10 periods of oscillations can be observed before the intensity finally dampens, as shown in Figure 3.1.7. The growth rate can then be extracted by fitting the intensity oscillation to a damped sinusoidal curve.

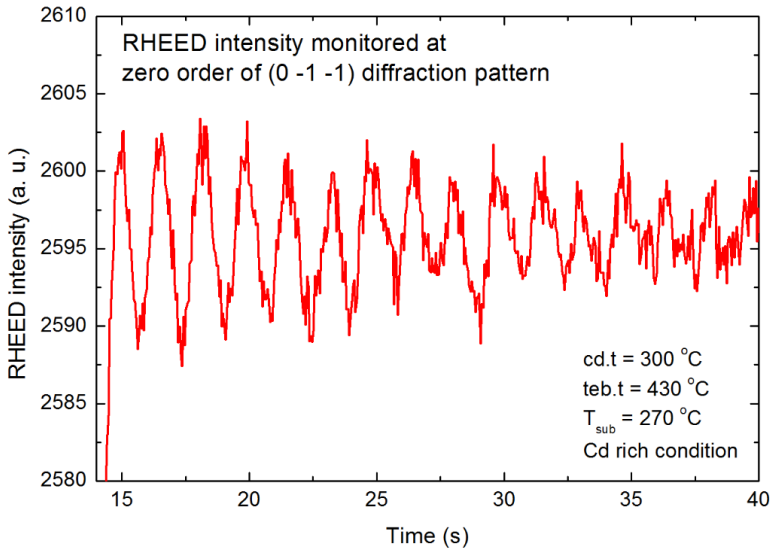

Figure 3.1.7. RHEED intensity oscillation during CdTe growth.

Figure 3.1.8 shows the CdTe growth rate versus Cd cell temperature under Te-rich conditions, and Figure 3.1.9 shows the CdTe growth rate versus Te cell temperature under Cd-rich conditions. Then the Cd/Te flux ratio can be calculated by GR_{Cd} / GR_{Te}.

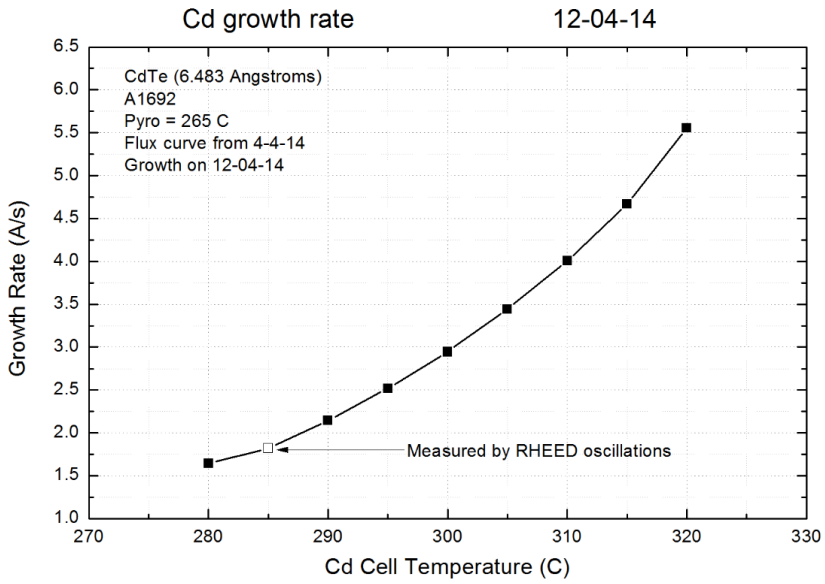

Figure 3.1.8. Calibrated CdTe growth rate versus Cd cell temperature.

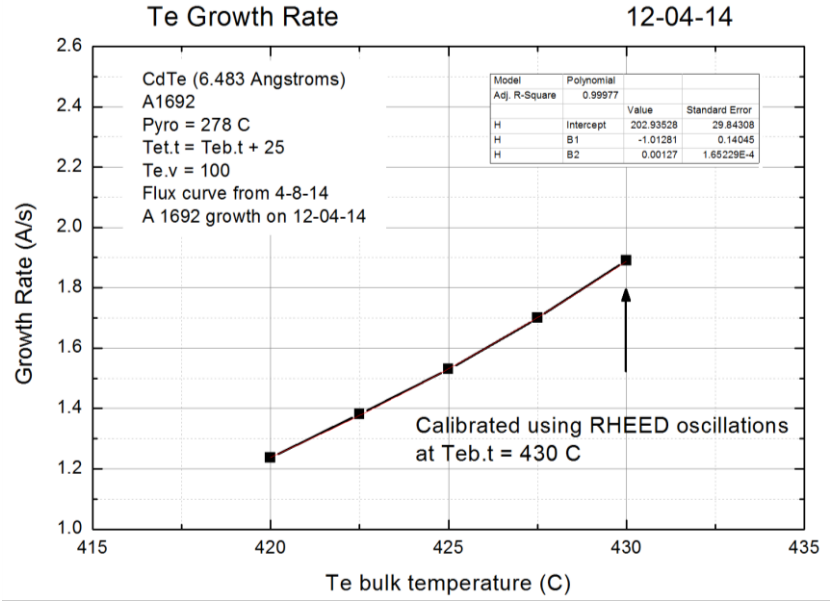

Figure 3.1.9. Calibrated CdTe growth rate versus Te cell temperature.

3.1.4 Summary

This section briefly introduces the fundamentals of MBE, and the growth procedures and conditions of InSb and CdTe materials. The growth rate and flux ratio calibrations of both InSb and CdTe are also discussed.

3.2 Structural and optical properties of CdZnTe/MgCdTe DH

As mentioned in the Section 1.2, the CdTe community has achieved tremendous progress in recent years, especially in the field of single-crystalline CdTe grown on InSb substrates. Regardless of the new achievements, the CdTe is not completely lattice-matched to InSb, which may cause material quality degradation when the layer is beyond a certain thickness (e.g. 2 μm). The problem can be circumvented by adding a small fraction of Zn into CdTe to form a CdZnTe alloy that is completely lattice-matched to InSb and has a negligible bandgap increase. A longer minority carrier lifetime is expected in the CdZnTe epilayer with a thickness beyond 2 μm since the misfit dislocation density is lower in the lattice-matched material system.

On the other hand, bulk CdZnTe substrates have dominated the high end of the HgCdTe infrared detector market due to the advantages of its chemical compatibility with, and lattice-match to, desired HgCdTe [45][46]. However this substrate suffers small wafer size and high manufacturing cost that impedes its application in large-area focal plane arrays [45][46]. Several alternative substrate techniques have been proposed and developed to address these issues, such as CdTe/Si [47], CdTe/Ge [48], CdTe/GaAs [49], CdTe/GaSb [50], or InSb [51], but failed to demonstrate the high performance HgCdTe infrared, especially long-wavelength infrared detectors, due to the huge dislocation density caused

by lattice-mismatch. Thus, growing closely lattice-matched CdZnTe alloys on InSb wafers can provide high-quality virtual substrates for HgCdTe growth with large size and low cost, which is beneficial to large-scale high-performance HgCdTe infrared focal plane arrays.

3.2.1 Structure design

Two sets of samples have been studied here. The first set consists of samples A1654, A1656 and A1659, which are 1 μm CdZnTe layers grown on quarter pieces of 2" InSb substrates under various Zn fluxes for the purpose of lattice-match calibration. The second set consists of samples A1667 and A1666, for structural and optical property comparisons, which are 3 μm CdTe/$Mg_{0.24}Cd_{0.76}Te$ and $Cd_{0.9946}Zn_{0.0054}Te$/$Mg_{0.24}Cd_{0.76}Te$ DHs grown on 2" InSb substrates, as shown in Figure 3.2.1. The 30 nm MgCdTe barrier layers with a Mg composition of 24 % provide carrier confinement and prevent photo-generated carriers from reaching the top surface and bottom buffer/substrate interface to recombine non-radiatively. The Zn composition in the CdZnTe alloy is designed to be 0.54 % so that the alloy is perfectly lattice-matched to the InSb substrate.

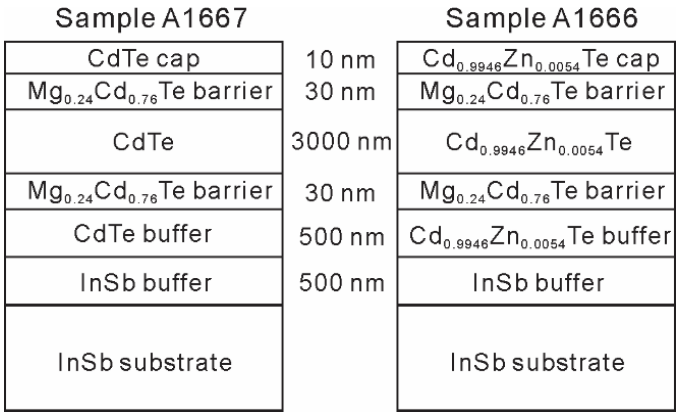

Figure 3.2.1. Layer structures of sample A1667: CdTe/$Mg_{0.24}Cd_{0.76}Te$ double heterostructure, and sample A1666: $Cd_{0.9946}Zn_{0.0054}Te$/$Mg_{0.24}Cd_{0.76}Te$ double heterostructure.

3.2.2 Structural and optical characterizations

The lattice-match calibration of a CdZnTe alloy to an InSb substrate is carried out by measuring the XRD patterns of the first set of samples and determining the Zn compositions. The ω/2θ scans at the (004) orientation of these samples, which are grown under Zn cell temperatures of 235 ℃, 245 ℃, and 255 ℃, respectively, are shown in Figure 3.2.2. It is observed that there are two separate peaks in samples A1654 and A1656 that correspond to the lattice constants of strained CdZnTe alloy and InSb in the growth direction. However, in sample A1659 the two peaks merge together indicating that the CdZnTe alloy has the same lattice constant as InSb, and thus a complete lattice match is reached. The Zn compositions listed in the figure are obtained by fitting the measured diffraction patterns based on the published structural parameters of ZnTe, CdTe [52], and InSb. The narrow full-width at half-maximums (FWHMs) of the CdZnTe peaks, which are comparable to InSb substrates and the clear Pendellösung fringes, are indicators of high quality CdZnTe layers and smooth CdZnTe/InSb interfaces.

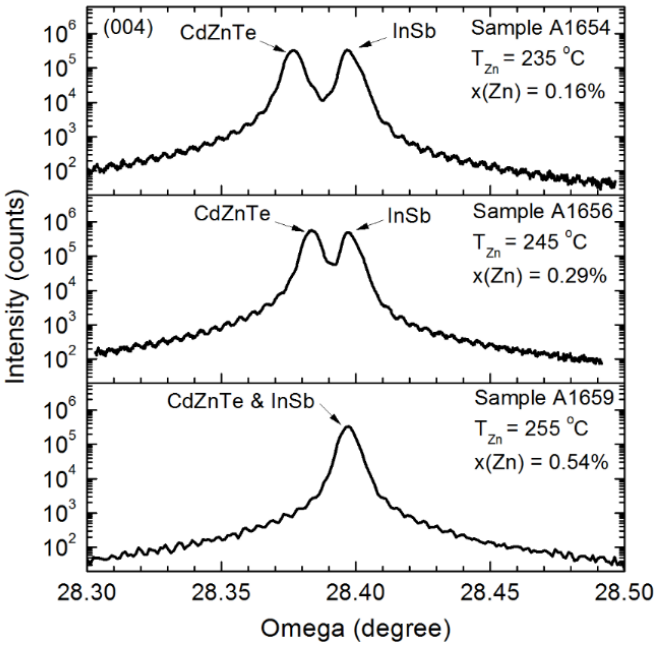

Figure 3.2.2. High-resolution x-ray diffraction (004) patterns of calibration samples A1654, A1656, and A1659, which are 1 μm thick CdZnTe layers on InSb substrates, showing that a complete lattice match is achieved.

The (004) ω/2θ scans were also carried out for samples A1666 and A1667, for which the experimental and simulated diffraction patterns are shown in Figure 3.2.3. The diffraction pattern of sample A1667 clearly shows two separate peaks representing InSb and CdTe, and a strain relaxation of ~30 % for the CdTe layer is determined by the simulation. On the contrary, for sample A1666 the two peaks merged together, which means that the CdZnTe layer and InSb substrate are lattice-matched. A larger FWHM of 22.6 arc sec of sample A1667 compared to that (16.6 arc sec) of sample A1666 shows the degraded material quality due to strain relaxation. The broad peaks of the MgCdTe barrier layers are observed in both samples as well as the Pendellösung fringes, indicating the high material quality of these layers and smooth MgCdTe/Cd(Zn)Te interfaces.

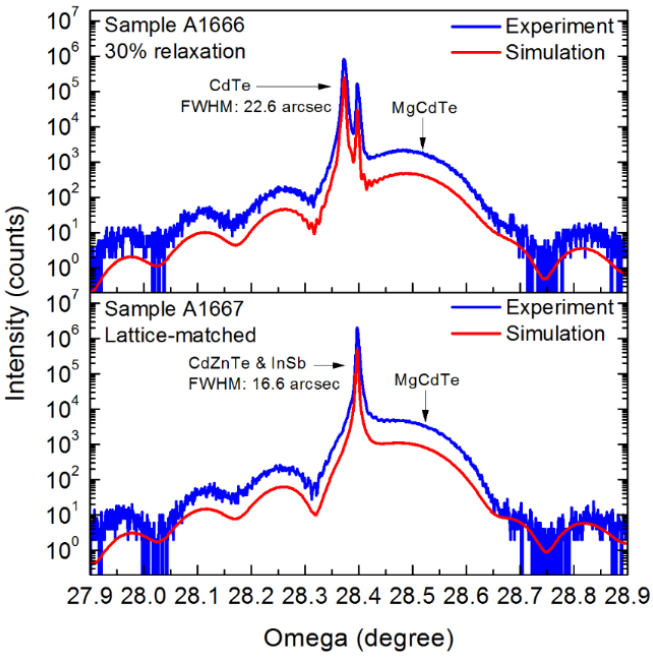

Figure 3.2.3. High-resolution x-ray diffraction (004) patterns of sample A1667 (3 μm CdTe/MgCdTe double heterostructure) and A1666 (3 μm CdZnTe/MgCdTe double heterostructure).

The steady-state PL spectra of samples A1666 and A1667 are measured at room temperature using a diode pumped solid state laser at 532 nm wavelength. The laser excitation power density is kept at 100 mW/cm^2 to mimic AM 1.5G solar radiation, and to protect II-VI films from thermal damage by overheating. As shown in Figure 3.2.4, sample A1667 has a PL peak wavelength of 825 nm, which corresponds to a band-to-band transition energy of 1.503 eV, while sample A1666 has a PL peak wavelength of 824 nm, which corresponds to a band-to-band transition energy of 1.505 eV. Such a slight increase in the transition energy indicates that the bandgap increase caused by introducing 0.54 % Zn in the CdTe binary is negligible, which is desirable for solar cells because any deviation from the optimal bandgap for single-junction solar cells is not preferred. The integrated PL

intensity of sample A1666 is at least one order of magnitude higher than that of sample A1667. Note although the lattice-mismatch between CdTe and InSb is only 0.03 %, it degrades noticeably the optical properties of the CdTe layer when it is as thick as 3 μm and misfit dislocations are generated as a result of strain relaxation.

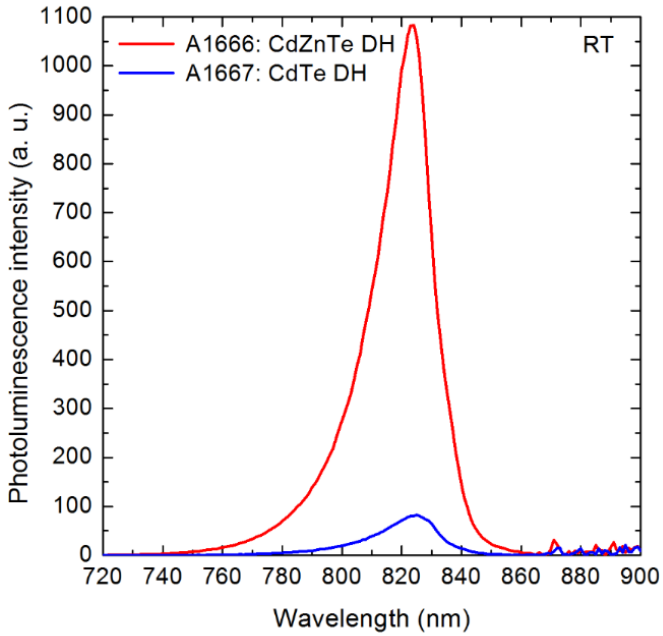

Figure 3.2.4. Room temperature photoluminescence spectra of samples A1666 and A1667, showing that the integrated photoluminescence intensity of the $Cd_{0.9946}Zn_{0.0054}Te/Mg_{0.24}Cd_{0.76}Te$ double heterostructure is over one order of magnitude stronger than that of the $CdTe/Mg_{0.24}Cd_{0.76}Te$ double heterostructure.

Figure 3.2.5 shows the room temperature PL decays, which are referred to as minority carrier lifetime in this paper, of samples A1666 and A1667 measured by a time-correlated single photon counting TRPL system. The samples are excited by an ultra-fast Ti:Sapphire laser with 750 nm emission wavelength, 130 fs pulse duration, and 0.8 MHz repetition rate. The luminescence signal is detected by a spectrometer equipped with a

high-speed micro-channel plate photomultiplier tube, with the detection wavelength set at 820 nm. The minority carrier lifetimes of both samples are determined by fitting the tails of the decay curves, and are shown in Figure 3.2.5. Sample A1666 has a much longer measured lifetime than that of sample A1667, which again proves the necessity of the lattice match to maintaining low defect density and long carrier lifetime for a thick epilayer. A minority carrier lifetime of 340 ns is observed for sample A1666. Note different lifetimes are observed on the edge and center of the 2" wafers for both samples, which are attributed to the growth non-uniformity. For example, it is hotter near the edge of the 2" InSb wafer than in the center due to the wafer holder design, which results in a better oxide removal and thus a higher material quality on the edge of the wafer.

Table 3.2 summarizes the strain relaxation, XRD FWHMs, integrated PL intensities and minority carrier lifetimes of the two samples. These findings consistently prove that better structural and optical qualities are obtained in the lattice-matched CdZnTe alloy compared to CdTe grown on InSb substrates.

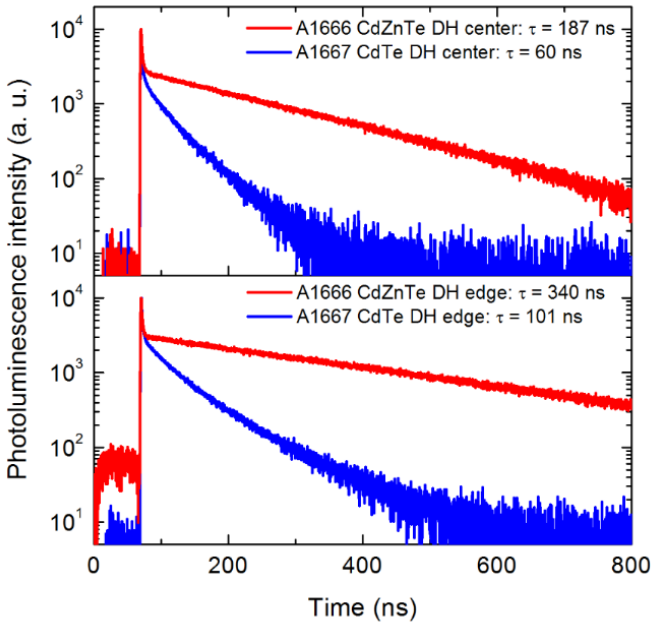

Figure 3.2.5. Time-resolved photoluminescence decays of samples A1666 and A1667 at room temperature, showing a significantly improved minority carrier lifetime achieved by replacing CdTe with CdZnTe.

Table 3.2. Strain relaxations, x-ray diffraction full-width at half-maximums, integrated photoluminescence intensities, and minority carrier lifetimes of sample A1667: CdTe/MgCdTe double heterostructure, and sample A1666: CdZnTe/MgCdTe double heterostructure.

Sample	A1667	A1666
Strain relaxation in Cd(Zn)Te layers (%)	30	0
XRD FWHM of Cd(Zn)Te layers (arc sec)	22.6	16.6
Integrated PL intensity (a. u.)	2556	29717
Carrier lifetime (ns)	101	340

3.2.3 Summary

In summary, a CdZnTe ternary alloy completely lattice-matched to an InSb substrate has been demonstrated with accurate composition control using MBE. The Zn composition is determined to be 0.54 % using XRD. Structural and optical properties comparisons have been carried out for 3 μm CdTe/MgCdTe DH and CdZnTe/MgCdTe DH samples grown on InSb substrates. Despite the fact that the lattice mismatch between CdTe and InSb is only 0.03 %, the 3 μm CdTe layer has a relaxation of ~30 %, and its (004) XRD peak is wider than that of a 3 μm lattice-matched CdZnTe layer. It has also been observed that the CdZnTe/MgCdTe DH sample shows an integrated PL intensity one order of magnitude higher than, and a carrier lifetime three times as long as, those of the CdTe/MgCdTe DH sample. The longest carrier lifetime is measured as 3.4×10^2 ns for the CdZnTe/MgCdTe DH. These comparisons show the excellent material quality of a lattice-matched CdZnTe alloy grown on an InSb substrate, and manifest its great potential in high-efficiency solar cells and large-area focal plane arrays.

3.3 Interface recombination mechanism of CdTe/MgCdTe double heterostructure

Recombination through the surface states, characterized by surface recombination velocity, is a major undesirable carrier loss mechanism for solar cells as well as other optoelectronic devices, such as lasers and photodetectors. The methods of reducing surface recombination include chemical passivation of the free surface and carrier confinement via heterostructures. The former can effectively reduce the surface recombination velocity, while the latter prevents the minority carriers from reaching the free surface. It is well known that AlGaAs, GaInP and AlInP can provide sufficient confinement for the photo-

generated minority carriers in GaAs [53]–[56], which effectively reduces the recombination at/near the free surface. Moreover, these heterointerfaces usually possess low interface recombination velocities, such as 18 cm/s for GaAs/$Al_{0.5}Ga_{0.5}As$ [53], and below 1.5 cm/s for GaAs/$Ga_{0.5}In_{0.5}P$ [55]. This minimizes the total non-radiative recombination of photo-generated carriers, and thus enables the widespread application of these heterointerfaces in GaAs-based solar cells, photodetectors and lasers. As one of the major materials used for single-junction solar cells, CdTe has a surface recombination velocity that is on the order of 10^5 cm/s [20]. Chemical passivation, such as Br:MeOH/hydrazine and Cd-annealing, has been proved effective in reducing the recombination velocity [57][58], and a CdS/CdTe heterostructure has demonstrated interface recombination velocities in the range of 10^3 cm/s to 10^6 cm/s [59][60]. More recently, there has been growing interest in single-crystalline CdTe and its ternary alloys, which have demonstrated minority carrier lifetimes up to 0.34 μs [16][18][19][22][29]. The previous record lifetime was achieved using $Mg_{0.24}Cd_{0.76}Te$ as barrier layers to form a DH structure, which offers effctive carrier confinement and demonstrates low interface recombination velocity of $(4.7 \pm 0.4) \times 10^2$ cm/s [19]. In the present work, we have determined the interface recombination velocities for various CdTe/MgCdTe DH structures with different MgCdTe barrier designs (Mg compositions and layer thicknesses). A significant reduction of the interface recombination velocity and a new record-long minority carrier lifetime are reported. The barrier height and barrier width dependence of the interface recombination velocity has been carefully investigated using the theory of thermionic emission and tunneling.

3.3.1 Thermionic-emission and tunneling induced interface recombination

The typical recombination processes in a double heterostructure are shown in Figure 3.3.1, including radiative, Shockley-Read-Hall (SRH), interface, and surface recombination. Here the interface recombination specifically refers to the non-radiative recombination through the mid-gap states at the barrier/middle layer interface. Additionally, the excess carriers generated in the middle layer can be thermally excited over or tunnel though the barrier and recombine non-radiatively at the surface. As the two processes only happen at the barrier/middle layer interface, they can be treated as equivalent interface recombination. We define the former process as thermionic-emission induced interface recombination [30], and the latter as tunneling induced interface recombination. Intuitively the thermionic-emission induced interface recombination rate is smaller for higher barriers, and the tunneling induced interface recombination rate is smaller for higher and thicker barriers.

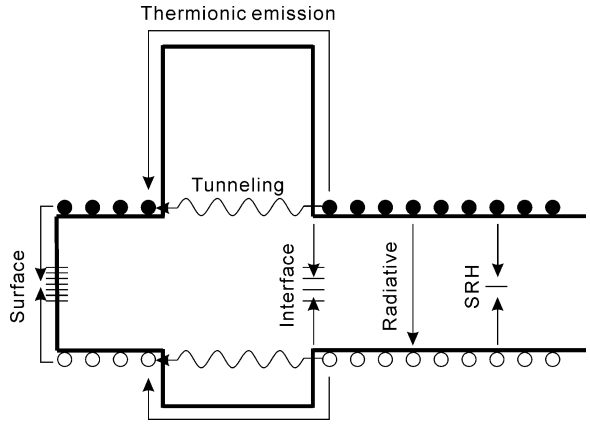

Figure 3.3.1. Typical recombination mechanisms in a double heterostructure, including radiative, Shockley-Read-Hall, interface, and surface recombination. The thermionic emission and tunneling processes are also shown.

With all the recombination processes considered, the effective lifetime τ_{eff} of the carriers in the middle layer can be expressed as:

$$\begin{aligned}\frac{1}{\tau_{eff}} &= \frac{1}{\tau_{rad}} + \frac{1}{\tau_{nr}} = \frac{1}{\tau_{rad}} + \frac{1}{\tau_{SRH}} + \frac{2S_{eff}}{d} \\ &= \frac{1}{\tau_{rad}} + \frac{1}{\tau_{SRH}} + \frac{2S_{int}}{d} + \frac{2S_{thermo}}{d} + \frac{2S_{tunnel}}{d}\end{aligned} \tag{3.3.1}$$

The above equation is valid in the low-injection regime where Auger recombination is negligible, and it assumes the carriers are distributed evenly in the middle layer. Here τ_{rad} is the radiative recombination lifetime, τ_{nr} is the non-radiative recombination lifetime, τ_{SRH} is the SRH recombination lifetime, and d is the middle layer thickness. The effective interface recombination velocity S_{eff} consists of three components, which are the interface recombination velocity S_{int}, the thermionic-emission induced interface recombination velocity S_{thermo}, and the tunneling induced interface recombination velocity S_{tunnel}.

According to the thermionic emission theory [61][62], the thermionic emission current is dependent on the barrier height ϕ_B (the energy difference between the carrier quasi Fermi level and the barrier band edge), effective mass of the carrier m^*, and the semiconductor temperature T:

$$J_{thermo} = e\frac{4\pi m^* k^2}{h^3} T^2 e^{-\frac{q\phi_B}{kT}} \tag{3.3.2}$$

With the carrier concentration n_c substituted in (2), J_{thermo} can also be expressed as:

$$J_{thermo} = en_c \left(\frac{kT}{2\pi m^*}\right)^{1/2} e^{-\frac{\Delta E_{C,V}}{kT}} \tag{3.3.3}$$

where $\Delta E_{C,V}$ represents the conduction or valence band offset between the barrier and middle layer materials. The tunneling current can be calculated through the following equation [63][64]:

$$J_{tunnel} = e\frac{m^* kT}{2\pi^2\hbar^2}\int_{E_{min}}^{E_{max}} Tr\left(E_x\right)\cdot ln\left(\frac{1+e^{\left(E_{f1}-E_x\right)/kT}}{1+e^{\left(E_{f2}-E_x\right)/kT}}\right)dE_x \tag{3.3.4}$$

where E_x represents the energy of the carriers, E_{f1} is the quasi Fermi level in the middle layer and E_{f2} is the quasi Fermi level in the cap layer. The integration is performed against the energy range from the middle layer conduction band edge E_{min} to the barrier conduction band edge E_{max}. $Tr(E_x)$ is the transmission probability of a carrier with energy E_x through a square barrier, calculated by quantum mechanics:

$$Tr\left(E_x\right) = \left[1+\frac{U_0^2 sinh^2\left(|k|W\right)}{4E_x\left(U_0-E_x\right)}\right]^{-1} \tag{3.3.5}$$

$$k = \frac{\sqrt{2m^*\left(E_x-U_0\right)}}{\hbar} \tag{3.3.6}$$

where U_0 is the barrier height and W is the barrier width. Assuming all the carriers that escape through thermionic emission and tunneling will recombine non-radiatively at the CdTe surface and the InSb substrate, we can obtain:

$$\frac{dn_c}{dt} = -\frac{2\left(J_{thermo}+J_{tunnel}\right)}{d\cdot e} \tag{3.3.7}$$

Thus the thermionic-emission and tunneling induced interface recombination velocities can be written as:

$$S_{thermo,tunnel} = \frac{J_{thermo,tunnel}}{e\cdot n_c} \tag{3.3.8}$$

In the following discussion we only consider the electron thermionic emission, as its rate is limiting the thermionic-emission induced recombination in the case we are studying.

3.3.2 Sample design

Figure 3.3.2 shows the schematic layer structure of the studied samples, where the CdTe absorber is sandwiched by two MgCdTe barriers to form a DH. The studied samples are divided into five sets, which feature different MgCdTe barrier designs, as shown in Table 3.3. Within each set, the thickness of the CdTe absorber is designed to range from 200 nm to 2000 nm in order to determine the interface recombination velocity of the CdTe/MgCdTe interface. Sets I, II, and III are designed to study the impact of barrier height on carrier lifetime, while sets III, IV, and V are designed to study the impact of barrier width on carrier lifetime. The key design parameters of each sample are summarized in Table 3.3. All the samples are grown on InSb (001) substrates by a VG V80H dual-chamber MBE system, and detailed growth conditions are explained previously and can be found in publications [16][29].

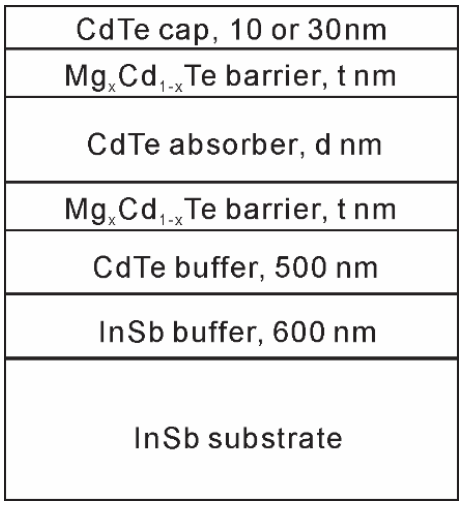

Figure 3.3.2. Schematic layer structure of the CdTe/MgCdTe double heterostructure.

Table 3.3. Structures and x-ray diffraction results of the studied CdTe/$Mg_xCd_{1-x}Te$ double heterostructure samples, where *d* is the CdTe middle layer thickness, t is the MgCdTe barrier thickness, and *x* is the Mg composition.

Set	Sample	Design		XRD results	
		d (nm)	*t* (nm)	$x \pm 0.02$	CdTe FWHM (arcsec)
I	A (A1639)	300	30	0.24	25
	B (A1626)	500			22
	C (A1622)	1000			19
	D (A1625)	2000			16
II	E (A1689)	250	20	0.36	27
	F (A1687)	333			23
	G (A1685)	500			22
	H (A1678)	1000			19
III	I (A1681)	200	15	0.46	27
	J (A1680)	250			26
	K (A1675)	333			24
	L (A1674)	500			21
	M (A1671)	1000			18
IV	N (A1731)	200	22	0.46	27
	O (A1730)	250			25
	P (A1727)	333			23
	Q (A1726)	500			21
V	R (A1706)	200	30	0.46	26
	S (A1703)	250			26
	T (A1702)	333			24
	U (A1696)	500			18

3.3.3 Structural characterization

XRD measurements are performed to determine the actual Mg compositions in the MgCdTe barriers, as well as to monitor the crystal quality of the grown samples. Figure 3.3.3 shows the (004) diffraction patterns of sample C, H, and M, of which the CdTe absorbers have identical 1 μm thickness, and the MgCdTe barriers have 24 %, 36 %, and 45 % Mg, respectively. The different positions of the main diffraction peak of MgCdTe layers indicates the different Mg compositions. A Clear difference in the thickness fringes resulting from different barrier layers is shown in the figure. The FWHMs of the CdTe peaks of all the samples range from ~ 16 arcsec to ~ 27 arcsec, depending on the thickness of the CdTe absorber. However, the FWHM of ~18 arcsec for 1 μm thick CdTe DH sample is comparable to that of the InSb substrate, indicating excellent crystal quality of the grown samples. The thickness fringes of both CdTe and MgCdTe layers are observed, which suggests not only excellent bulk crystalline quality, but also sharp and smooth interfaces. Figure 3.3.4 shows a comparison of the measured and simulated (004) XRD patterns, from which the Mg composition can be determined accurately. The Mg compositions of the MgCdTe barriers for the rest of the samples are listed in Table 3.3.

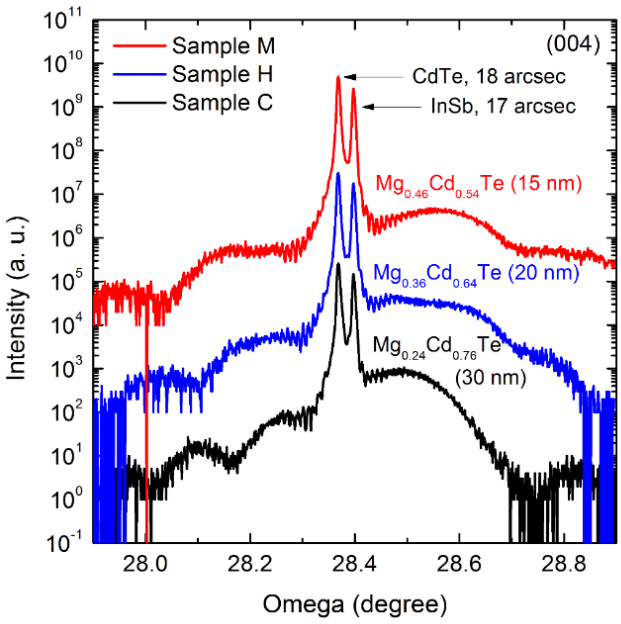

Figure 3.3.3. High-resolution (004) x-ray diffraction patterns of CdTe/MgCdTe double heterostructures with identical 1 μm thick CdTe middle layer but different MgCdTe barrier layers.

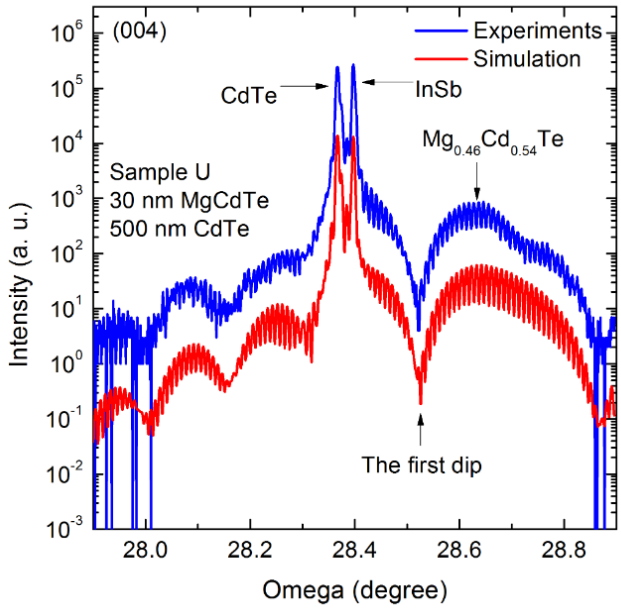

Figure 3.3.4. A comparison between the simulated and measured (004) x-ray diffraction patterns for sample U (500 nm CdTe middle layer, 30 nm $Mg_{0.46}Cd_{0.54}Te$ barriers).

3.3.4 Barrier height dependent lifetime and interface recombination velocity

The study of barrier height dependent carrier lifetime is carried out among sets I, II and III. TRPL measurements are carried out using a time-correlated single photon counting system. The samples with CdTe absorber thicknesses beyond 300 nm are excited by an ultrafast Ti:Sapphire laser with a 750 nm emission wavelength, a 130 fs pulse duration, and a 0.8 MHz repetition rate. In order to guarantee nearly full absorption of the incident photons in the CdTe absorbers, the excitation source is switched to an ultrafast fiber laser with a 550 nm wavelength and a 1 MHz repetition rate for the samples with CdTe absorber thicknesses below 300 nm. It is estimated that for samples of different thickness, the initial excited carrier density is on the order of 10^{15} cm^{-3}. The PL signal is detected by a spectrometer equipped with a high-speed micro-channel plate photomultiplier tube, with the detection wavelength set at 820 nm.

The measured room temperature PL decays of the studied samples (sets I, II, and III) are plotted in Figure 3.3.5. The decay time is referred to as the effective minority carrier lifetime throughout the paper. To avoid the issues of growth non-uniformity and material quality degradation, the TRPL measurements are carried out on the same spot of the samples, and within 24 hours after the samples are taken out of the vacuum. The minority carrier lifetimes of the studied samples, as listed in Figure 3.3.5 and Table 3.4, are obtained by fitting the tails of the PL decay curves. The decreasing lifetime with thickness suggests a non-zero interface recombination velocity. A longest lifetime of 0.83 μs has been observed for sample L.

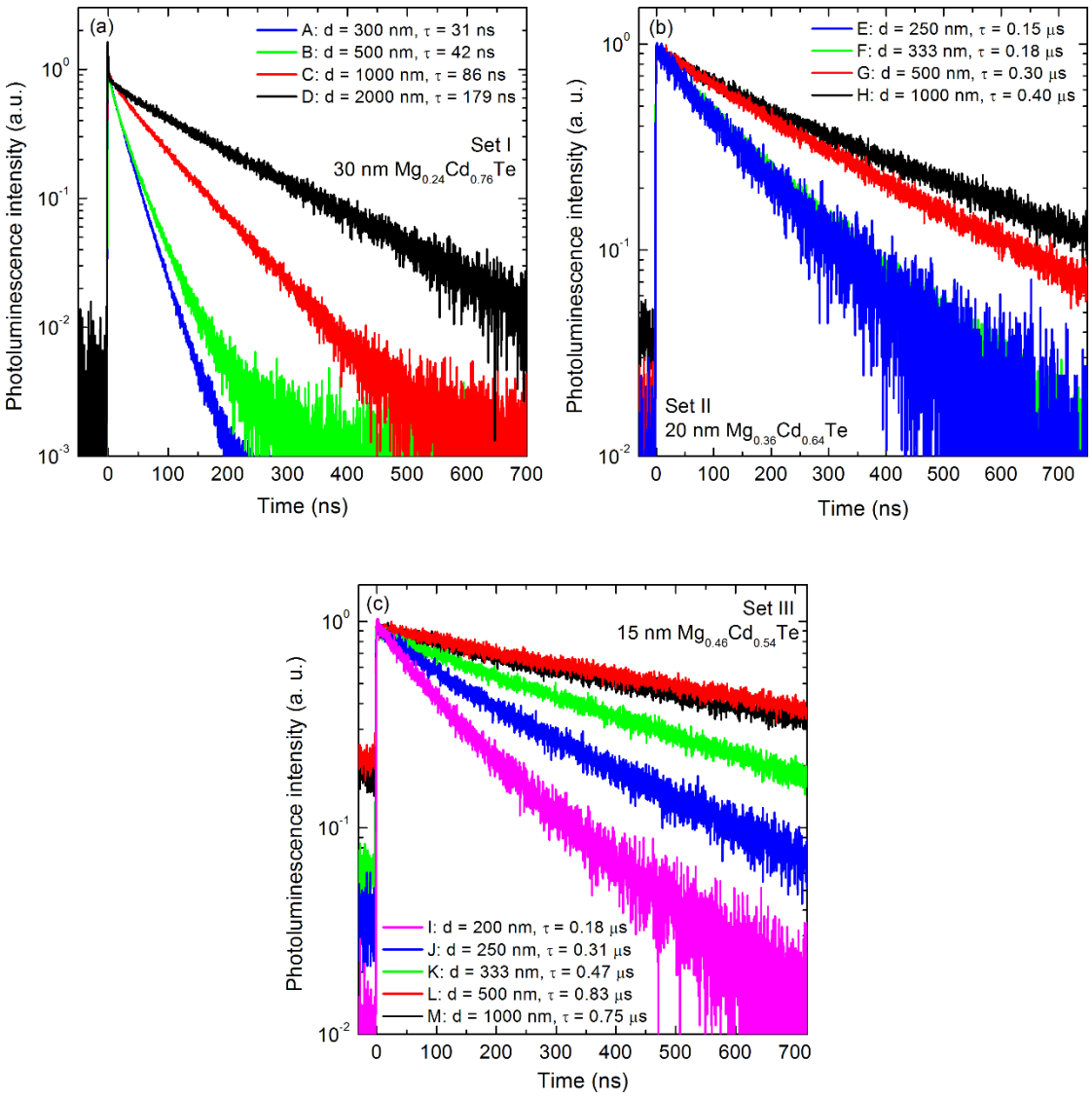

Figure 3.3.5. Normalized time-resolved photoluminescence decays at room temperature for the studied CdTe/MgCdTe double heterostructures. A long minority carrier lifetime of 0.83 μs has been observed.

The radiative recombination lifetime τ_{eff} can be calculated by the following equation:

$$\tau_{rad} = \frac{1}{(1-\gamma)Bn_c} \tag{3.3.9}$$

where B is the radiative recombination coefficient, n_c is the carrier concentration that includes background doping concentration N_{doping} and excess carrier concentration δn, and γ is the photon recycling factor that depends on the thickness and absorption coefficients of the absorber and can be calculated using the ray-tracing method [34][65]. The term (1-γ) accounts for the effect of self-reabsorption of the luminesce photons [66][67], which enhances the radiative recombination lifetime. Using published data for B [18] and assuming a carrier concentration of 5×10^{14} cm^{-3}, the τ_{rad} of a 1000 nm CdTe absorber is calculated to be ~2.8 μs. For the cases where SRH recombination is dominant as in the samples of set I, τ_{rad} can be neglected. However, the measured lifetimes of some of the studied samples in sets II and III are close to 1 μs, and it is thus necessary to consider the radiative recombination lifetime when calculating the interface recombination velocity, as shown below:

$$\frac{1}{\tau_{eff}}-\frac{1}{\tau_{rad}}=\frac{1}{\tau_{nr}}=\frac{1}{\tau_{SRH}}+\frac{2S_{eff}}{d} \tag{3.3.10}$$

The non-radiative recombination lifetime τ_{nr} of each sample can be calculated by subtracting τ_{rad} from τ_{eff}. The background doping concentrations of the grown samples are estimated to be on the order of 10^{14} cm^{-3} by capacitance-voltage measurements, in which the bias is applied through two Hg probes that contact the front surfaces of the double heterostructures. Therefore we pick 5×10^{14} cm^{-3} to calculate τ_{rad}. The effective interface recombination velocity S_{eff} can thus be determined by a linear fitting of $1/\tau_{nr}$ versus $2/d$. The plots of $1/\tau_{nr}$ versus $2/d$ are shown in Figure 3.3.6. Linear fittings of the data shows S_{eff} of $(4.7\pm0.4)\times10^2$ cm/s, 61 ± 14 cm/s and 30 ± 10 cm/s for CdTe/$Mg_{0.24}Cd_{0.76}Te$ (30 nm), CdTe/$Mg_{0.36}Cd_{0.64}Te$ (20 nm) and CdTe/$Mg_{0.46}Cd_{0.54}Te$ (15 nm) DHs, respectively. The

error bars are determined by considering both the standard deviation of the fittings and the uncertainty of the carrier concentration. Note that the determination of bulk SRH lifetime via this fitting has large error bars, especially for the case of high quality materials with long lifetimes. The complete data can be found in Table 3.4.

Table 3.4. Minority carrier lifetimes and interface recombination velocities for sample sets I, II, and III: τ_{eff} is the measured effective lifetime, τ_{rad} is the calculated radiative recombination lifetime assuming a carrier concentration of 5×10^{14} cm^{-3}, τ_{nr} is the non-radiative recombination lifetime, and S_{eff} is the effective interface recombination velocity.

Set	Sample	τ_{eff} (μs)	τ_{rad} (μs)	τ_{nr} (μs)	S_{eff} (cm/s)
I	A	0.031	/	0.031	$(4.7 \pm 0.4) \times 10^2$
	B	0.042	/	0.042	
	C	0.086	/	0.086	
	D	0.18	/	0.18	
II	E	0.15	1.08	0.17	61 ± 14
	F	0.18	1.25	0.21	
	G	0.30	1.63	0.37	
	H	0.40	2.86	0.47	
III	I	0.18	0.97	0.22	30 ± 10
	J	0.31	1.07	0.45	
	K	0.47	1.24	0.75	
	L	0.83	1.61	1.72	
	M	0.75	2.82	1.01	

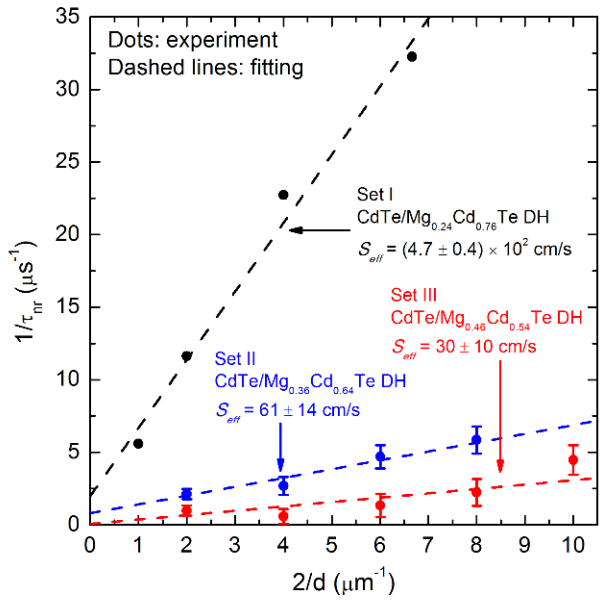

Figure 3.3.6. Plots of inversed non-radiative recombination lifetime $1/\tau_{nr}$ versus inversed sample thickness $2/d$ (sets I, II and III). The effective interface recombination velocities are extracted to be $(4.7 \pm 0.4) \times 10^2$ cm/s, 61 ± 14 cm/s and 30 ± 10 cm/s for $CdTe/Mg_{0.24}Cd_{0.76}Te$, $CdTe/Mg_{0.36}Cd_{0.64}Te$, and $CdTe/Mg_{0.46}Cd_{0.54}Te$ double heterostructures, respectively.

3.3.5 Barrier width dependent lifetime and interface recombination velocity

The study of barrier width dependent carrier lifetime and interface recombination velocity is carried out among sets III, IV and V. The barriers in these samples have the same Mg composition, but different thicknesses of 15 nm, 22 nm, and 30 nm, respectively. TRPL measurements are carried out using the same set up as described in last section. The initial excited carrier density is lowered to about or below 10^{14} cm^{-3}, by defocusing the laser beam, to fulfill the low injection criterial. The measured room temperature PL decays of the samples in sets IV and V are plotted in Figure 3.3.7. The decays are single exponential decays, and the fitted decay times are shown in the figures. All the samples present very long lifetimes of over 1 μs, with the longest lifetime of 2.7 μs observed in

sample U, which has 30 nm $Mg_{0.46}Cd_{0.54}Te$ barriers and a 500 nm CdTe middle layer. These long lifetimes are attributed to significantly reduced interface recombination due to the increased barrier heights and widths.

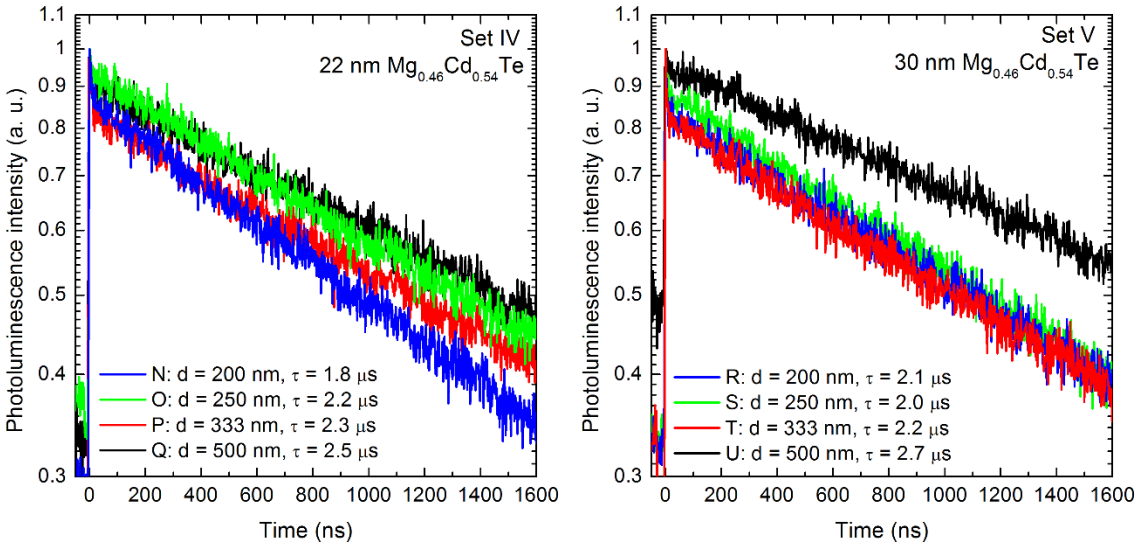

Figure 3.3.7. Normalized time-resolved photoluminescence decays at room temperature for the studied CdTe/MgCdTe double heterostructures (sets IV and V). A longest minority carrier lifetime of 2.7 μs has been observed.

The interface recombination velocities for samples in sets IV and V can be obtained using the same method as described in last section. The radiative and non-radiative recombination lifetimes, which are calculated using Equation (3.3.9) and (3.3.10), are shown in Table 3.5. The plots of $1/\tau_{nr}$ versus $2/d$ are shown in Figure 3.3.8, where the error bars of $1/\tau_{nr}$ are determined by considering both the error bars of measured lifetime τ_{eff} and radiative recombination coefficient B. Weighted fittings are performed, which give effective interface recombination velocities of 1.1 ± 0.5 cm/s and 0.1 ± 0.7 cm/s for the DHs in sets III and IV, respectively. These values are close to/better than the lowest number

reported for the GaAs material system, which is $S \leq 1.5$ cm/s observed in GaAs/$Ga_{0.5}In_{0.5}P$ double heterostructure [55].

Table 3.5. Minority carrier lifetimes and interface recombination velocities for sample sets IV and V: τ_{eff} is the measured effective lifetime, τ_{rad} is the calculated radiative recombination lifetime, and τ_{nr} is the non-radiative recombination lifetime; S_{eff} is the effective interface recombination velocity; d_{CdTe} is the CdTe middle layer thickness, which is determined from the x-ray diffraction patterns.

Set	Sample	d_{CdTe} (nm)	τ_{eff} (μs)	τ_{rad} (μs)	τ_{nr} (μs)	S_{eff} (cm/s)
IV	N	200	1.8	5.3	2.7	1.1 ± 0.5
	O	250	2.2	5.9	3.4	
	P	333	2.3	6.9	3.4	
	Q	490	2.5	9.0	3.5	
V	R	190	2.1	5.5	3.5	0.1 ± 0.7
	S	241	2.0	6.1	3.0	
	T	320	2.2	7.1	3.2	
	U	510	2.7	9.2	3.8	

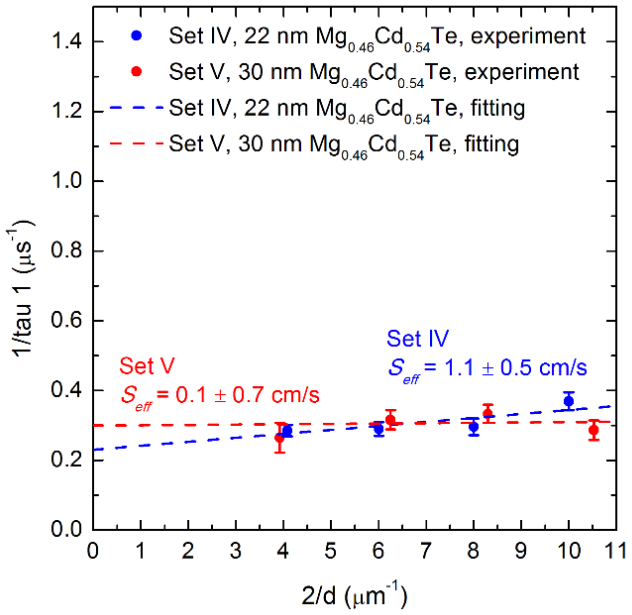

Figure 3.3.8. Plots of inversed non-radiative recombination lifetime $1/\tau_{nr}$ versus inversed sample thickness $2/d$ for the studied of CdTe/MgCdTe double heterostructures (sets IV and V). The interface recombination velocities of both double heterostructures are fitted.

Moreover, by using the temperature-dependent PL measurement, the room temperature internal quantum efficiencies of the samples can be estimated. Figure 3.3.9 shows the integrated PL intensity as a function of temperature for sample R, which increases monotonously as the temperature decreases due to the reduction of the non-radiative recombination rate and enhancement of the radiative recombination rate. As the temperature approaches 10 K, the integrated PL intensity is gradually saturated, indicating that radiative recombination is dominating. A saturated integrated PL intensity means the internal quantum efficiency reaches 100 %. By comparing the integrated PL intensity at 10 K and 300 K, it is concluded the internal quantum efficiency at 300 K is ~ 40 %.

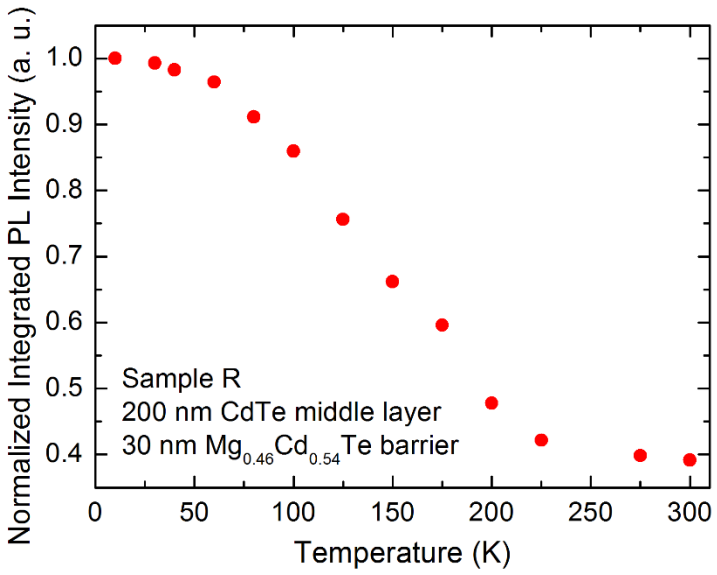

Figure 3.3.9. Normalized integrated photoluminescence versus temperature for sample R, showing an internal quantum efficiency of ~ 40 % at room temperature.

The internal quantum efficiency is defined as [68]:

$$IQE = \frac{\frac{1}{\tau_{rad}}}{\frac{1}{\tau_{rad}} + \frac{1}{\tau_{nr}}} \tag{3.3.11}$$

With the internal quantum efficiency and effective carrier lifetime determined by temperature-dependent PL and TRPL previously, the radiative lifetime τ_{rad} and non-radiative lifetime τ_{nr} are calculated to be 5.25 μs and 3.5 μs, respectively. These numbers are in good agreement with the ones in Table 3.5. Thus we obtain:

$$\frac{1}{\tau_{nr}} = \frac{1}{\tau_{SRH}} + \frac{2S_{eff}}{d} = 0.29\,\mu s^{-1} \tag{3.3.12}$$

Equation (3.3.12) suggests an upper limit for the effective interface recombination velocity S_{eff}, which is obtained by assuming an infinitely long SRH lifetime: $2S/d \leq 0.29$

μs^{-1}, and thus $S \leq 2.7$ cm/s. This value is in agreement with the one determined through the linear fitting (as shown in Figure 3.3.8).

3.3.6 Analysis of the thermionic-emission and tunneling induced interface recombination in CdTe/MgCdTe double heterostructures

The effective interface recombination velocity of set I samples, determined as $(4.7 \pm 0.4) \times 10^2$ cm/s previously [19], is one order of magnitude larger than those of the samples with higher Mg composition barriers (sets II and III). The reason for the difference is that CdTe/MgCdTe have type-I band alignment [69], and with larger Mg composition the barriers are higher for both electrons and holes. Thus it is easier for the excess carriers in CdTe/$Mg_{0.24}Cd_{0.76}Te$ DH to be thermally excited over the barriers and recombine non-radiatively at the CdTe surface and in the CdTe/InSb buffers. This process is defined as thermionic-emission induced interface recombination, with its lifetime and recombination velocity calculated by the following two equation:

$$\tau_{th} = \frac{d}{2} \cdot \sqrt{\frac{2\pi m^*}{kT}} \cdot e^{-\frac{\Delta E_C}{kT}} \tag{3.3.13}$$

$$S_{th} = \sqrt{\frac{kT}{2\pi m^*}} \cdot e^{-\frac{\Delta E_C}{kT}} \tag{3.3.14}$$

The hypothesis is validated qualitatively by temperature-dependent TRPL measurements for CdTe/$Mg_{0.24}Cd_{0.76}Te$ and CdTe/$Mg_{0.46}Cd_{0.54}Te$ DHs, as shown in Figure 3.3.10. The blue dots are carrier lifetimes extracted from the TRPL measurements at different temperatures from 150 K to 296 K. For illustration, the temperature dependence of radiative lifetime ($\tau_{rad} \propto T^{1.5}$, red dashed line), bulk SRH and interface ($\tau_{SRH,int} \propto T^{-0.5}$, black dashed line), thermionic-emission induced interface recombination lifetime ($\tau_{th} \propto T^{-}$

$^{0.5}$ $e^{\Delta Ec/kT}$, grey dashed line), and effective recombination lifetime (blue dashed line), are plotted along with the data. Here T is the semiconductor temperature, and ΔE_C is the conduction band offset between CdTe and $Mg_xCd_{1-x}Te$. The conduction band offsets of CdTe/$Mg_{0.24}Cd_{0.76}Te$ and CdTe/$Mg_{0.46}Cd_{0.54}Te$ are 250 meV and 480 meV, respectively, which are 70 % of the band-gap energy difference [69][70]. It can be clearly seen that for the CdTe/$Mg_{0.24}Cd_{0.76}Te$ DH at temperatures near 300 K, the measured lifetime increases rapidly as temperature decreases, indicating a strong contribution of the thermionic-emission induced interface recombination process. The fitting shows that thermionic-emission induced interface recombination accounts for the measured effective lifetime at 296 K. However, for the CdTe/$Mg_{0.46}Cd_{0.54}Te$ DH, the carrier lifetime is determined only by radiative and SRH recombination, meaning $Mg_{0.46}Cd_{0.54}Te$ is effective in confining the photo-generated carriers within the CdTe middle layer. It is thus concluded that the previously determined effective interface recombination velocity for CdTe/$Mg_{0.24}Cd_{0.76}Te$ is largely due to the recombination process in which carriers are thermally excited over the barriers and recombine at the CdTe free surface, and in the CdTe/InSb buffers.

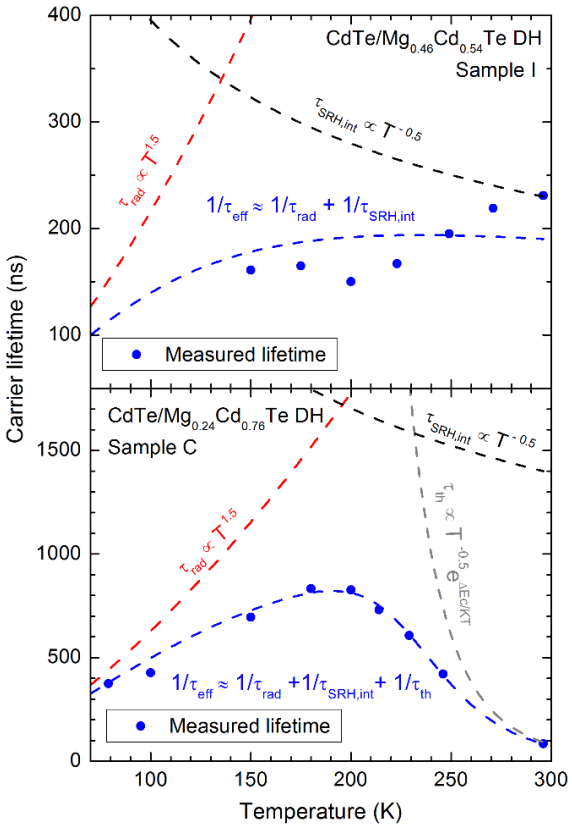

Figure 3.3.10. Carrier lifetime versus temperature for CdTe/$Mg_{0.46}Cd_{0.54}$Te (upper) and CdTe/$Mg_{0.24}Cd_{0.76}$Te (lower) double heterostructures (blue dots). Also plotted are the fitted radiative lifetime ($\tau_{rad} \propto T^{1.5}$, red dashed line), bulk Shockley-Read-Hall and interface lifetime ($\tau_{SRH,int} \propto T^{-0.5}$, black dashed line), thermionic-emission induced interface recombination lifetime ($\tau_{th} \propto T^{-0.5}\, e^{\Delta Ec/kT}$, grey dashed line), and effective recombination lifetime (blue dashed line).

The ultra-low interface recombination velocity (close to zero) achieved in sample sets IV and V indicates nearly perfect quality of the CdTe/MgCdTe interfaces. The larger interface recombination velocities for CdTe/MgCdTe DHs with either lower Mg composition (set I) or smaller barrier thickness (set III) can be attributed to the thermionic-emission and/or tunneling induced interface recombination. Table II shows the comparison

between the measured and calculated effective interface recombination velocities. The S_{thermo} and S_{tunnel} are calculated using equations (3.3.2)-(3.3.8), assuming that the conduction band offset between CdTe and MgCdTe is 30 % of their band-gap energy difference. A range of these calculated interface recombination velocity values are given to account for the uncertainty in the barrier width and height. The calculated S_{eff} is a sum of the calculated S_{thermo} and S_{tunnel}, assuming an ideal interface with zero S_{int}. It is found that the thermionic-emission induced interface recombination dominates for the DH samples with $Mg_{0.24}Cd_{0.76}Te$ barriers (set I), and it becomes negligible for the DH samples with $Mg_{0.46}Cd_{0.54}Te$ barriers (sets III, IV, and V). The tunneling induced interface recombination dominates for the DH samples with 15 nm barriers (set III), and it is greatly suppressed for the DH samples with thicker barriers (sets IV and V). Additional visualized comparison is shown in the semi-log plots in Figure 3.3.11. The calculated S_{eff} is in good agreement with the measured S_{eff}, with the error bars taken into account. This proves that the CdTe/MgCdTe interface is nearly ideal, and insufficient carrier confinement resulting from low and thin barriers leads to carrier loss through thermionic-emission and tunneling induced interface recombination.

Table 3.6. Comparison of the calculated and measured interface recombination velocities of the four sets of CdTe/$Mg_xCd_{1-x}Te$ double heterostructures in this study.

Set	$x \pm 0.02$	d_{MgCdTe} ±2 (nm)	Measured S_{eff} (cm/s)	Calculated S_{thermo} (cm/s)	Calculated S_{tunnel} (cm/s)	Calculated S_{eff} (cm/s)
I	0.24	30	470 ±40	(0.3~1.4)×10^3	(2~10)×10^1	(0.3~1.5)×10^3
III	0.46	15	30 ±10	0.05~0.25	0.3~33	0.4~33
IV	0.46	22	1.1 ±0.5	0.05~0.25	0.005~0.079	0.06~0.33
V	0.46	30	0.1 ±0.7	0.05~0.25	0.003~0.017	0.06~0.26

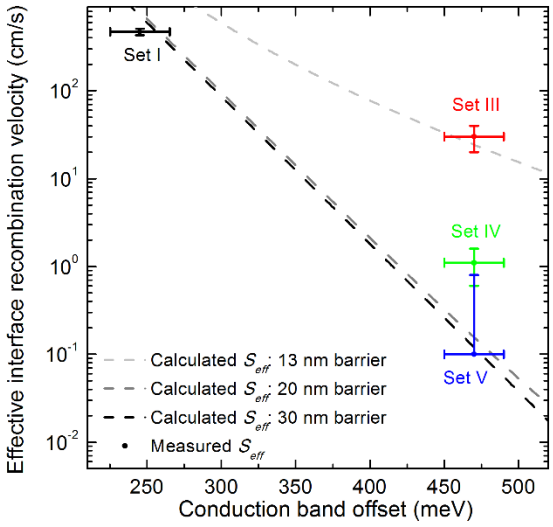

Figure 3.3.11. A visualized comparison between the measured and calculated effective interface recombination velocities: the dashed lines are calculated S_{eff} as a function of the CdTe/MgCdTe conduction band offset for double heterostructures with 13 nm, 20 nm, and 30 nm barriers. The dots represent the measured S_{eff} for the four sets of double heterostructure samples.

3.3.7 Summary

In Section 3.3, the interface recombination velocities and carrier lifetimes of five different CdTe/MgCdTe double heterostructures, which have MgCdTe barriers with different Mg compositions (0.24, 0.36, and 0.46) and thicknesses (15 nm, 22 nm, and 30 nm), have been carefully studied. Figure 3.3.12 shows all the achieved lifetime values plotted against the CdTe layer thickness. The carrier lifetime and interface recombination velocity are greatly enhanced in the samples with thicker and higher MgCdTe barriers, and a recombination model involving thermionic emission and tunneling is developed to explain these findings. The plots also show that the best samples are approaching the radiative recombination limited regime.

Figure 3.3.13 shows the progress of the CdTe development at ASU. In less than two years, the CdTe lifetime has increased dramatically from 50 ns to 2.7 μs through rigorous structure and growth optimization. Both the CdTe lifetime and the CdTe/MgCdTe interface recombination velocity are currently as good as those of GaAs-based materials, suggesting the great potential of CdTe solar cells to achieve excellent performance comparable to that of GaAs solar cells.

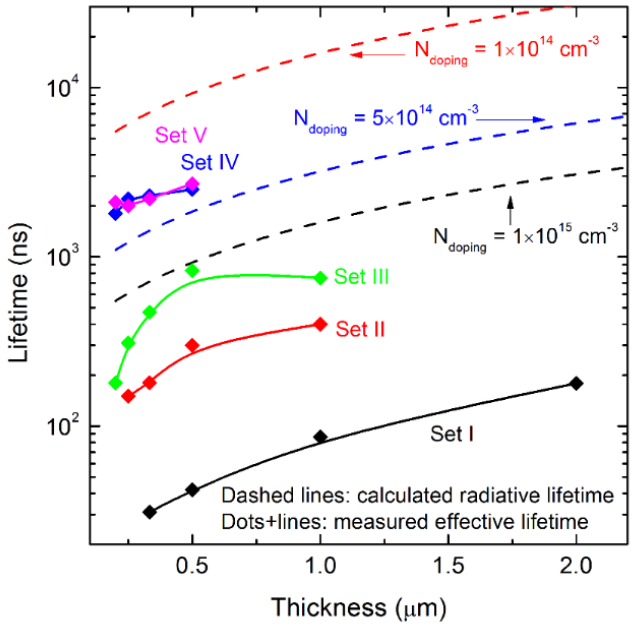

Figure 3.3.12. The achieved lifetimes versus CdTe middle layer thickness for all the studied CdTe/MgCdTe double heterostructure samples.

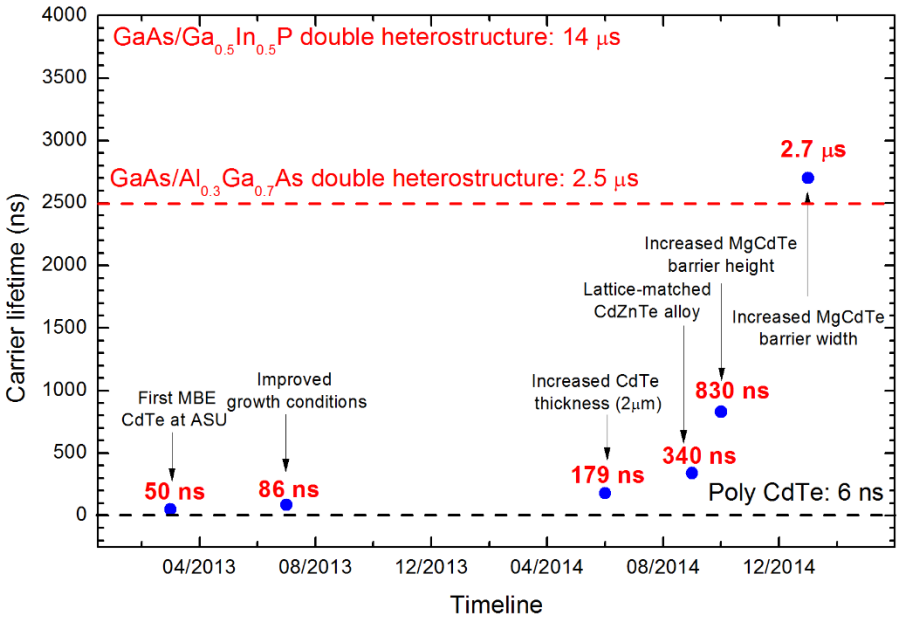

Figure 3.3.13. Progress of the CdTe lifetime development.

3.4 MgCdTe alloys for II-VI/Si tandem solar cell applications

The efficiency records for Si, GaAs, and CdTe single-junction solar cells have reached 25.6 % [7], 28.8 % [5][6], and 21.5 %[8], respectively, but still smaller than the ~ 30 % limit for single-junction solar cells predicted by the detailed balance model [11]. Further improvement of the efficiency to beyond 30 % may require a tandem design with multiple junctions. III-V multi-junction (MJ) solar cells have demonstrated steady enhancement of cell performance, and have achieved the highest efficiency of 46 % among all photovoltaic technologies [3][4]. However, the high manufacturing costs, including expensive substrates and epitaxial layer deposition, prevent III-V MJ solar cells from being widely adopted. To reduce the material costs, Si substrates have been used to replace Ge substrates in III-V/Si MJ cells [71][72], which, however, suffer substantial efficiency drop due to the poor III-V material quality when grown on Si. Decent efficiency improvement has been obtained by lifting-off the III-V cells from lattice-matched substrates and transplanting them to Si bottom cells [73][74], but this process still cannot yield an efficiency of over 30 %. On the other hand, the use of II-VI materials for MJ photovoltaics to reduce overall cost has been explored. The study of CdZnTe/Si tandem cell grown by molecular beam epitaxy (MBE) has been reported to yield an efficiency of 17 % [75].

Another II-VI alloy, MgCdTe, can also be integrated with Si to produce a tandem solar cell. Compared to CdZnTe alloys, MgCdTe alloys have a wider bandgap range from 1.5 eV to 3.0 eV, which is more favorable in splitting the solar spectrum for MJ cells with three or more junctions. In addition, MgCdTe alloys have closer lattice-match to CdTe, and thus fewer extended defects are expected to be produced during growth. Since epitaxial MgCdTe alloys were first demonstrated in the early 90s [76][70], little progress has been

made. The previous demonstration of CdTe/MgCdTe DHs with long carrier lifetime and low interface recombination velocity, suggests that high-quality MgCdTe can be achieved.

In this section, we report the $Mg_xCd_{1-x}Te$ alloys with a band gap of ~ 1.7 eV, which have been grown using MBE, and characterized using high-resolution X-ray diffraction (XRD), transmission electron microscopy (TEM), steady-state photoluminescence (PL), and time-resolved photoluminescence (TRPL). The growth is carried out on InSb (100) substrates as an initial demonstration, but further integration with Si can be achieved through either monolithic growth or epitaxial lift-off.

3.4.1 Sample structure design and growth

A DH structure is designed to provide confinement for photo-generated carriers, and thus reduces surface recombination and enhances luminescence. This confinement creates a desirable model system in which the $Mg_xCd_{1-x}Te$ alloy can be isolated and studied. Figure 3.4.1 shows the DH schematic of the studied samples, where the $Mg_xCd_{1-x}Te$ middle layer is sandwiched by two $Mg_yCd_{1-y}Te$ barrier layers. The Mg composition x is designed to be 0.13 to yield a bandgap of 1.7 eV, and the Mg composition y is designed to be 0.50 so that the conduction and valence band offsets are large enough to confine carriers. The compositionally-graded MgCdTe layers are inserted between the middle and the barrier layers.

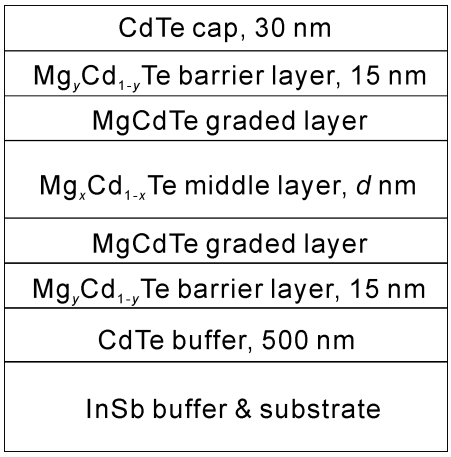

Figure 3.4.1. Schematic layer structure of the $Mg_xCd_{1-x}Te/Mg_yCd_{1-y}Te$ double heterostructures.

Three samples, with different $Mg_xCd_{1-x}Te$ middle layer thicknesses of 100 nm, 200 nm, and 500 nm (referred as samples A, B, and C, respectively), are grown using a VG V80H dual-chamber MBE system with separate III-V and II-VI growth chambers connected by an ultra-high vacuum (UHV) transfer chamber. The growth conditions are similar to those of CdTe on InSb. First, the InSb substrates are thermally deoxidized under Sb flux in the III-V chamber, followed by the growth of a 600-nm-thick InSb buffer at a rate of 10.8 nm/min, an Sb/In flux ratio of 1.5, and a substrate temperature of 390 ℃. The substrates are then transferred to the II-VI chamber under UHV, which prevents oxidation and contamination of the surfaces. The II-VI growth is carried out at a growth rate of 9.6 nm/min and a Cd/Te flux ratio of 1.5. The substrate temperature is set initially at 280 ℃ (measured by a pyrometer) prior to growth and gradually drops to between 265 ℃ and 270 ℃ due to changes in surface emissivity. The Mg cell temperature for the $Mg_xCd_{1-x}Te$ middle layer growth is determined by extrapolating the Mg flux calibration curve and assuming a unity sticking coefficient of Mg. The Mg cell temperature is ramped linearly at

a constant rate of 15 ℃/min during the MgCdTe graded layer growth, and the Mg composition profile is thus concave.

3.4.2 Structural properties

High-resolution XRD measurements are performed to characterize the structural properties of the grown samples, including the layer thicknesses and Mg compositions of the middle and the barrier layers. The full-width at half-maximum (FWHM) of the diffraction peaks is also examined. Figure 3.4.2 shows the (004) $\omega/2\theta$ scans for samples A, B, and C, where the blue and red lines represent the experimental and simulation results, respectively. Pendellösung fringes of the $Mg_xCd_{1-x}Te$ middle layers are clearly observed for all samples, indicating excellent crystalline and interface qualities. The MgCdTe diffraction-peak positions for samples A, B, and C are located at 28.469 °, 28.464 °, and 28.448 °, respectively. With the (115) reciprocal space maps of samples A and C showing negligible strain relaxation (Figure 3.4.3), the difference of the diffraction-peak positions must be due to different Mg composition in the MgCdTe alloys. The simulations of the diffraction patterns give Mg composition of 0.134 and 0.135 for samples A and B, and a slightly smaller Mg composition of 0.114 for sample C. The weaker and broader peaks at ~ 28.7 ° are due to the MgCdTe barrier layers that have higher Mg composition. The thickness fringe at ~ 28.1 °is due to the 30-nm-thick CdTe cap. Table I shows the structural parameters of the studied samples. The determination of Mg composition of the barrier layer is not as accurate as that of the middle layer since the diffraction peaks associated with these layers are weak and broad.

Table 3.7. X-ray diffraction results and design parameters of the studied $Mg_xCd_{1-x}Te/Mg_yCd_{1-y}Te$ double-heterostructure samples, where x and y are the Mg compositions for the middle and the barrier layers, respectively.

Sample	XRD results		Design	
	$x \pm 0.007$	$y \pm 0.01$	d_{middle} (nm)	$d_{barrier}$ (nm)
A (A1722)	0.134	0.46	100	15
B (A1701)	0.135	0.46	200	15
C (A1721)	0.114	0.46	500	15

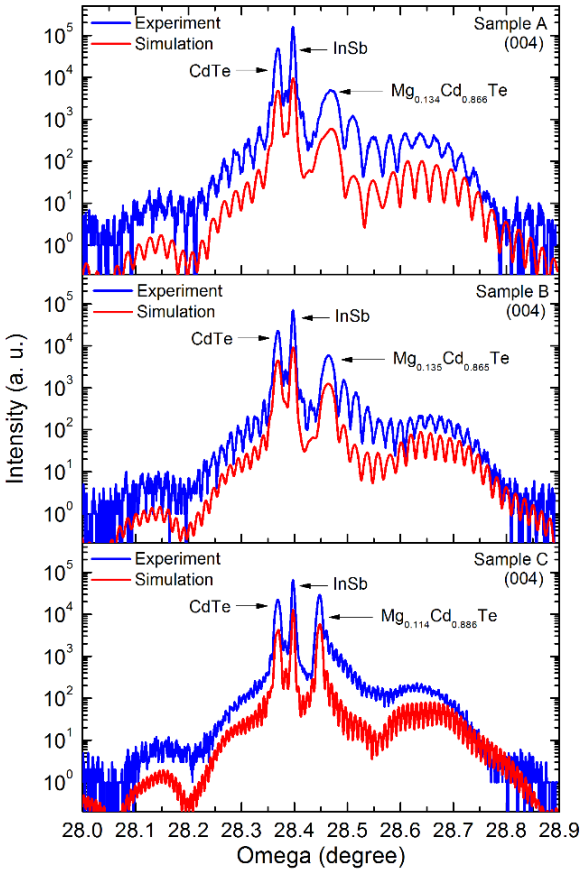

Figure 3.4.2. Experimental and simulated (004) X-ray diffraction patterns for the studied $Mg_xCd_{1-x}Te/Mg_yCd_{1-y}Te$ double heterostructures.

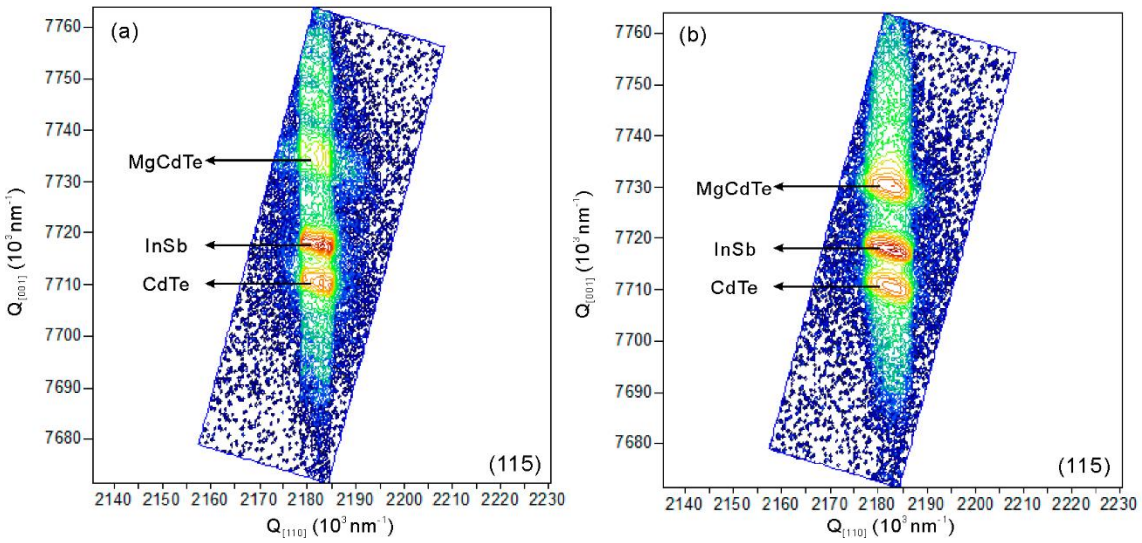

Figure 3.4.3. Reciprocal space maps of two $Mg_xCd_{1-x}Te/Mg_yCd_{1-y}Te$ double heterostructures at (115) direction with contours plotted on a logarithmic scale: (a) sample A; (b) sample C.

Samples are prepared for TEM observation along [110]-type projection using conventional mechanical polishing and dimple grinding, followed by argon-ion-milling (maximum beam energy 2.2 keV) under liquid-nitrogen cooling in an effort to minimize ion-beam damage. Electron microscopy is performed using a JEOL JEM-4000EX high-resolution electron microscope with an accelerating voltage of 400 kV and structural resolution of 1.7 Å. Figure 3.4.4 is a representative bright-field TEM image for sample B, showing excellent structural quality of the entire structure; extended defects are rarely observed in the CdTe buffer layer. Sharp CdTe/InSb and CdTe/MgCdTe interfaces are also observed. The interface between MgCdTe barrier and grading layers is not visible due to diffraction conditions.

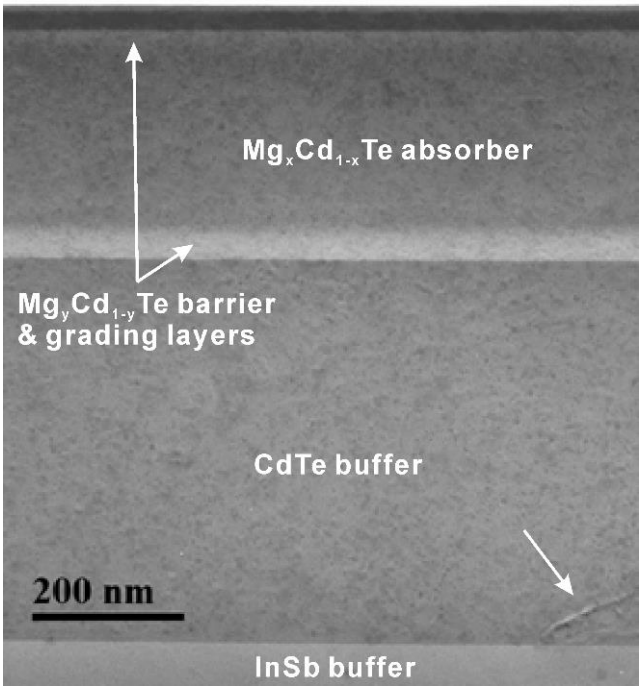

Figure 3.4.4. Bright-field cross-sectional transmission electron micrograph of the entire structure of sample B, showing excellent structural quality: occasional extended defect observed in the CdTe buffer layer (arrowed). The interface between MgCdTe barrier and grading layers is not visible due to diffraction conditions.

3.4.3 Optical properties

The steady-state PL spectra of the three samples are measured at room temperature using an InGaN laser diode with a wavelength of 405 nm and an excitation density of 2 W/cm^2. The photoluminescence is collected and analyzed by a spectrometer equipped with a photomultiplier tube. As shown in Figure 3.4.5, samples A and B show an identical PL peak wavelength of 714 nm, which corresponds to a band-to-band transition energy of 1.74 eV, while sample C shows a PL peak wavelength of 726 nm, which corresponds to a band-to-band transition energy of 1.71 eV. The red shift of the PL peak wavelength again confirms the lower Mg composition in sample C. Relaxation of the tensile strain of MgCdTe layers, on the contrary, will induce a blue shift of the PL peak wavelength and is

thus not likely here. A PL peak at 820 nm is observed in samples A and B but very weak in sample C, which indicates that the 820-nm emission is from the CdTe buffer pumped by the transmitted laser light. The substantial reduction of MgCdTe luminescence intensity in sample A with the thinnest middle layer is due not only to the limited absorption of the pump light (less than 100 %), but also the greater impact of the non-radiative interface recombination.

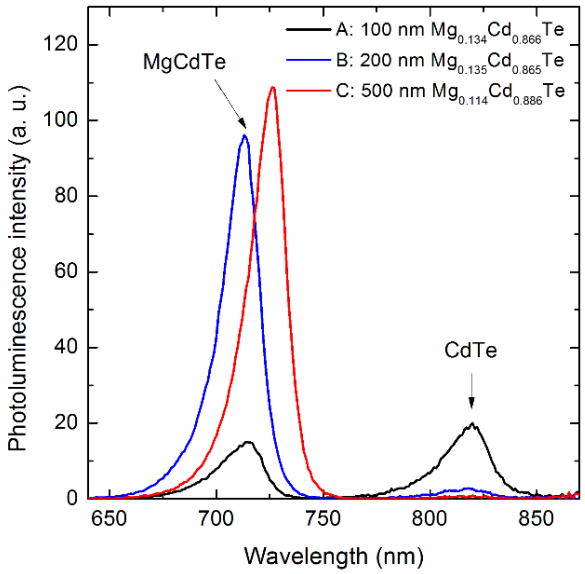

Figure 3.4.5. Steady-state photoluminescence spectra of the studied samples at room temperature.

TRPL measurements are carried out using a time-correlated single-photon-counting system to study the minority carrier lifetimes. The samples are excited by an ultrafast fiber laser with a 650-nm emission wavelength, a 6-ps pulse duration, and a 10-MHz repetition rate. It is estimated that the initial excess carrier density is on the order of 10^{15} cm^{-3}. The PL signal is detected by a spectrometer equipped with a high-speed micro-channel plate

photomultiplier tube, with the detection wavelength set at 714 nm. The measured room-temperature PL decays of the samples are plotted in Figure 3.4.6. The decay time is referred to as the effective minority carrier lifetime. The minority carrier lifetimes of samples A, B and C are determined to be 1.9 ns, 5.6 ns, and 11 ns, respectively, by fitting the tails of the PL decay curves. To the best of our knowledge, the lifetime of 11 ns is the longest carrier lifetime ever reported for MgCdTe. The reduced lifetime with decreasing thickness suggests a non-zero effective recombination velocity at the $Mg_xCd_{1-x}Te/Mg_yCd_{1-y}Te$ interfaces on both sides of the DH, and potentially carrier leakage to the CdTe surface and InSb substrate through thermionic emission over the barrier. Figure 3.4.7 shows the linear fitting of $1/\tau$ versus $2/d$, suggesting an effective interface recombination velocity S_{eff} of $(1.869 \pm 0.007) \times 10^3$ cm/s. An improved interface recombination velocity is expected with optimized barrier layer design and growth conditions.

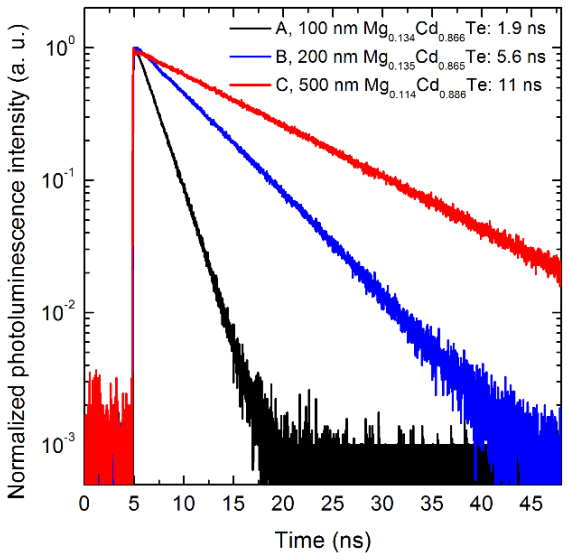

Figure 3.4.6. Normalized time-resolved photoluminescence decays at room temperature for the studied samples. The effect of interface recombination is clearly apparent since the measured effective lifetime decreases with decreasing middle layer thickness.

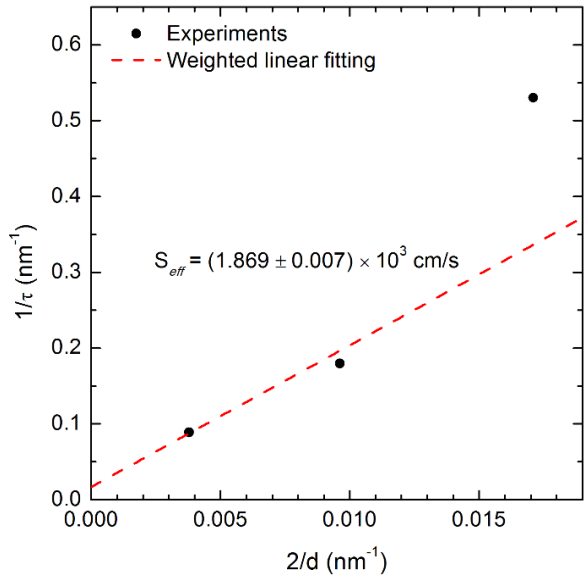

Figure 3.4.7. Plot of inverse non-radiative recombination lifetime $1/\tau_{nr}$ versus inverse sample thickness $2/d$ for the studied double heterostructures. The effective interface recombination velocity is extracted to be $(1.869 \pm 0.007) \times 10^3$ cm/s.

The PL spectra and decays of sample B at low temperatures are measured using the same set up as described above. For PL spectra measurement, the sample is cooled by a close-loop compressed Helium cryostat; for PL decay measurement, the sample is cooled by liquid Nitrogen in a N_2 environment. The measured PL decays of sample B at all temperatures are plotted in Figure 3.4.8. The minority carrier lifetimes are determined by fitting the tails of the PL decay curves. The lifetime is plotted against temperature, along with the integrated PL intensity, in Figure 3.4.9. A maximum lifetime of 105 ns is observed at 175 K. It can be clearly seen that at high temperatures (above 175 K) non-radiative recombination dominates, and at low temperatures (below 175 K) radiative recombination dominates. The integrated PL intensity increases with decreasing temperature and starts to saturate at 150 K, which suggests radiative recombination contributes more significantly

than non-radiative recombination. The temperature-dependence trends of integrated PL intensity and carrier lifetime are in great agreement.

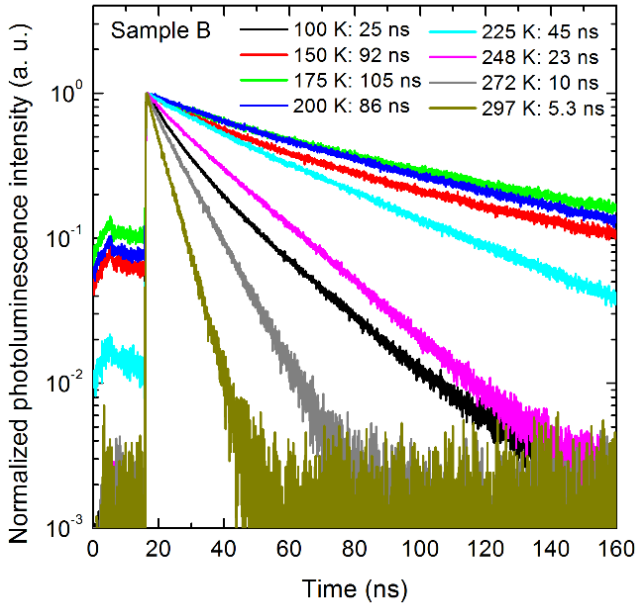

Figure 3.4.8. Normalized time-resolved photoluminescence decays for sample B at temperatures from 100 K to 300 K.

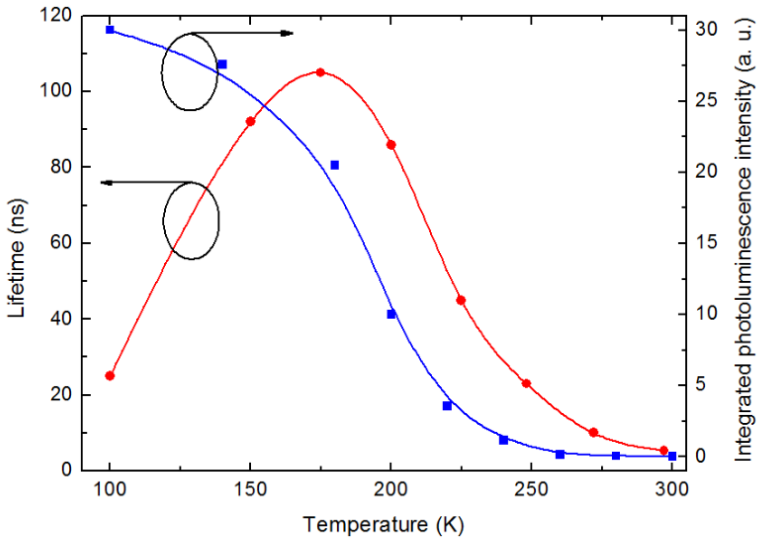

Figure 3.4.9. Carrier lifetime and integrated photoluminescence intensity versus temperature for sample B.

Through temperature-dependent TRPL measurement, we can also decouple the different recombination mechanisms, as we did in Section 3.3.3. Figure 3.4.10 below shows the fitting results of the temperature-dependent lifetimes of sample B, which clearly show that the recombination at room temperature is dominated by the thermionic-emission induced interface recombination. The conduction band offset between $Mg_{0.13}Cd_{0.87}Te$ and $Mg_{0.46}Cd_{0.54}Te$ is ~ 350 meV, and the compositional graded MgCdTe layer can help the carrier transport by lowering the effective barrier height. The fitted SRH and interface lifetime is on the order of 1 μs, indicating excellent bulk and interface quality of the sample. Further improvement for the lifetime and interface recombination velocity of the DH sample can be achieved by raising the MgCdTe barrier height.

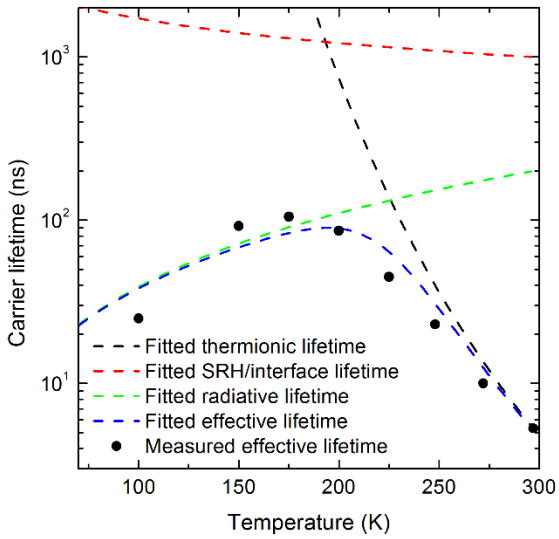

Figure 3.4.10. Carrier lifetime versus temperature for sample B (black dots). Also plotted are the fitted radiative lifetime ($\tau_{rad} \propto T^{1.5}$, green dashed line), bulk Shockley-Read-Hall and interface lifetimes ($\tau_{SRH,int} \propto T^{-0.5}$, red dashed line), thermionic-emission induced interface recombination lifetime ($\tau_{th} \propto T^{-0.5}\ e^{\Delta Ec/kT}$, black dashed line), and effective recombination lifetime (blue dashed line).

3.4.4 Summary

The growth of $Mg_xCd_{1-x}Te$ alloy on an InSb (100) substrate with a Mg composition of ~13 % and a bandgap of ~ 1.7 eV is demonstrated. The excellent crystal quality of the samples has been confirmed by XRD, and cross-sectional TEM. The MgCdTe epilayers are coherently strained for thicknesses up to 500 nm. Steady-state PL measurements confirm that the grown $Mg_xCd_{1-x}Te$ samples have bandgaps around 1.7 eV, and thicker samples give stronger luminescence. The carrier lifetimes are determined to be 11 ns for 500 nm MgCdTe, 5.6 ns for 200 nm MgCdTe, and 1.9 ns for 100 nm MgCdTe, and an effective interface recombination velocity is determined to be $(1.869 \pm 0.007) \times 10^3$ cm/s cm/s. The carrier lifetime increases with decreasing temperature from room temperature to 175 K and then decreases with decreasing temperature, suggesting non-radiative recombination dominates at high temperatures and radiative recombination dominates at low temperatures. A maximum lifetime of 105 ns is observed at 175 K for the 200 nm MgCdTe sample. These promising results show the great potential of using 1.7 eV MgCdTe for II-VI/Si tandem solar cells.

CHAPTER 4

CONCLUSIONS

Ten types of planar structures with different combinations of smooth, textured, non-reflective, and reflective surfaces are explored to optimize the optical design of GaAs single-junction solar cells for record energy conversion efficiency. The calculation of optical properties and device performance is carried out by a semi-analytical model. Both absorptance and photon recycling factor increase with absorber thickness as more photons can be absorbed/reabsorbed in longer optical paths, while the average generation rate decreases with absorber thickness. Among all the optical designs, those utilizing a combination of textured and reflective surfaces maximize absorptance at a given absorber thickness, and hence provide the smallest absorber thickness and largest average generation rate. The device performance calculation shows an optimal thickness for all the structures due to the tradeoff between more absorption and less non-radiative recombination losses. It is found that by applying both a textured surface and a reflective back surface, the optimal absorber thickness is only ~10 % of that of planar solar cells, while the absorption is still sufficient. Thus, the non-radiative recombination and spatial-relaxation loss is greatly reduced and the conversion efficiency is increased by more than 10 %. The structure that has textured surfaces on both sides and a mirror on the back side gives a maximum achievable efficiency of 31.20 % under one sun AM1.5G solar spectrum.

The Phong distribution is implemented in the semi-analytical model to explore the impact of non-Lambertian scattering on the optical properties and device performance of GaAs single-junction solar cells. The absorptance is strongly enhanced with a scattering closer to the Lambertian case compared to a higher order of Phong distribution at an

absorber thickness below 1 μm. It also indicates that the thinner the absorber is, the more dependent the absorptance is on the scattering effectiveness of the textured surface. The modeling results also show stronger light extraction with rougher surfaces (smaller *m* values), especially for thinner absorbers, which therefore have smaller photon recycling factors compared to absorbers with smoother surfaces. The optimal thickness of the device shifts to larger values, and the maximum efficiency drops, as the surface becomes smoother (larger *m* values). The efficiency of a thinner cell is found to be more dependent on the scattering effectiveness, which results from the dependence of J_{sc}; however, the V_{oc} remains almost constant for different orders of Phong distributions due to the domination of non-radiative recombination under a normal one-sun condition.

The study on the optical structures of the GaAs solar cells inspired more efforts into research on solar cells with surface roughness. Devices with surface roughness and reflective mirrors are more desirable as the absorber thickness is greatly reduced because of increased optical path by multiple scattering/reflection events. A practical design is proposed by integrating the ultra-thin solar cell with a reflective back scattering layer. The candidates for the scattering layer and the reflective mirror are carefully examined. The material used for the scattering layer should have a wide bandgap as well as being lattice-matched to GaAs, and the mirror should be highly reflective with minimal parasitic loss in visible and NIR ranges. According to detailed simulation, $Al_{0.5}In_{0.5}P$ and Ag are the best materials for the scattering layer and the mirror, respectively. The MgF_2/ZnS double-layer AR coating for an ultra-thin GaAs single-junction solar cell is carefully optimized using the transfer matrix method. Multiple layers, including GaInP window layer, GaAs absorber, and GaInP BSF layer, are taken into account for the reflectance calculation. The optimal

AR coating design is determined to be a 96 nm MgF_2/47 nm ZnS pair, which gives 1.60 % reflection loss.

A fabricated 300 nm thick GaAs single-junction solar cell with AlInP/Au reflective back scattering has demonstrated a J_{sc} of 24.5 mA/cm^2, a V_{oc} of 1.0 V, a *FF* of 77 %, and an efficiency of 19.1 %. However, these measured values are still below the modeled best achievable values due to imperfections in the device, such as non-Lambertian scattering, non-unity reflectivity of the back mirror, non-radiative recombination, and series resistance. Calculations show a reduced average reflectivity of 95 % for the $Al_{0.52}In_{0.48}P$/Au interface near the GaAs absorption edge for the Lambertian scattering case, compared to the value of 98 % for the air/Au interface. The Phong exponent of the non-Lambertian scattering at the back surface is determined to be ~12 by fitting the simulated short-circuit current density and external quantum efficiency to experimental values. A non-radiative recombination lifetime of ~130 ns, and a specific series resistivity of 1.2 $\Omega \cdot cm^2$ are determined by fitting the simulated and measured V_{oc} and *FF*, respectively. The efficiency of the ultra-thin GaAs single-junction solar cell can be further improved by enhancing the reflective back scattering layer using dielectric material, reducing non-radiative recombination using a material with better quality or a compositional gradient window layer, and improving the current spreading in the device.

The MBE growth procedures of InSb and CdTe, as well as the growth rate and flux ratio calibrations are discussed in details. A few studies on the carrier lifetime and interface recombination velocity of the CdTe material system have been carried out.

A CdZnTe ternary alloy completely lattice-matched to an InSb substrate has been demonstrated with accurate composition control using MBE. The Zn composition is

determined to be 0.54 % using X-ray diffraction (XRD). Structural and optical properties comparisons have been carried out for a 3 μm thick CdTe/MgCdTe double heterostructure (DH) and a CdZnTe/MgCdTe DH grown on InSb substrates. Despite the fact that the lattice mismatch between CdTe and InSb is only 0.03 %, the 3 μm thick CdTe layer has a relaxation of ~30 %, and its (004) XRD peak is wider than that of a 3 μm thick lattice-matched CdZnTe layer. It has also been observed that the CdZnTe/MgCdTe DH sample shows an integrated PL intensity one order of magnitude higher than, and a carrier lifetime three times as long as, those of the CdTe/MgCdTe DH sample. The longest carrier lifetime is measured as 0.34 μs for the CdZnTe/MgCdTe DH. These comparisons show the excellent material quality of a lattice-matched CdZnTe alloy grown on an InSb substrate, and manifest its great potential for high-efficiency solar cells and large-area focal plane arrays.

The interface recombination mechanism in CdTe/MgCdTe DH samples are carefully explored. Five sets of samples, which have MgCdTe barriers with different heights and widths, are characterized using time-resolved photoluminescence (TRPL). The first three sets of samples are designed with 30 nm $Mg_{0.24}Cd_{0.76}Te$, 22 nm $Mg_{0.36}Cd_{0.64}Te$, and 15 nm $Mg_{0.46}Cd_{0.54}Te$ barriers, respectively, to study the impact of barrier height on interface recombination. It is found that the effective interface recombination velocity is dependent on the barrier height (Mg composition), which is attributed to the thermionic emission process in which the carriers go over the barriers and recombine at the CdTe surface or the InSb substrate. Specifically, the effective interface recombination velocities for CdTe/$Mg_{0.24}Cd_{0.76}Te$ (30 nm), CdTe/$Mg_{0.36}Cd_{0.64}Te$ (20 nm), and CdTe/$Mg_{0.46}Cd_{0.54}Te$ (15 nm) are determined as $(4.7 \pm 0.4) \times 10^2$ cm/s, 61 ± 14 cm/s, and 30 ± 10 cm/s,

respectively. Temperature-dependent TRPL measurements show that the recombination in the sample with 30 nm $Mg_{0.24}Cd_{0.76}Te$ barriers is dominated by thermionic-emission induced interface recombination, while that in the sample with 15 nm $Mg_{0.46}Cd_{0.54}Te$ barriers is not. The longest minority carrier lifetime of 0.83 μs among these samples is observed in a DH sample with a 500 nm CdTe middle layer and 15 nm $Mg_{0.46}Cd_{0.54}Te$ barriers. Further enhancement of carrier lifetime and reduction of interface recombination velocity is achieved when the barrier width is increased to 22 nm and 30 nm, which is believed to be due to the reduction of the carrier tunneling through the barriers. A recombination model that involves thermionic emission and tunneling has been developed, which can explain the barrier height and width dependent interface recombination velocity of the CdTe/MgCdTe double heterostructures. The longest observed carrier lifetime is 2.7 μs and the lowest interface recombination velocity is 0.1 ± 0.7 cm/s, both of which are very close to/better than the best values for GaAs material system. These promising results show the great potential of CdTe/MgCdTe DHs in photovoltaic and other optoelectronic device applications.

In order to address some issues related with single-junction thin film solar cells, such as the high manufacturing costs of GaAs cell, and the relative low efficiency of CdTe cell, the MgCdTe/Si tandem solar cell is proposed. The MgCdTe subcell with a bandgap energy of ~ 1.7 eV is used to absorb the high energy photons, while the Si subcell is to absorber the low energy ones. The initial demonstration (material growth and characterization) is carried out via molecular beam epitaxial (MBE) growth on InSb substrates. The eventual configuration of the tandem cell will be poly-MgCdTe cell integrated with mono-Si cell. However, the material property study of single-crystalline

MgCdTe grown by MBE is essential as the understanding of defects, lifetime, interface, and doping can be transferred to the poly-crystalline MgCdTe. The excellent crystal quality of the grown samples has been confirmed by XRD, and cross-sectional transmission electron microscopy. The MgCdTe epilayers are coherently strained for thicknesses up to 500 nm as observed in reciprocal space maps. Steady-state PL measurements confirm that the grown $Mg_xCd_{1-x}Te$ samples have bandgaps around 1.7 eV, and thicker samples give stronger luminescence. The carrier lifetimes are determined to be 11 ns for 500 nm MgCdTe, 5.6 ns for 200 nm MgCdTe, and 1.9 ns for 100 nm MgCdTe, and an effective interface recombination velocity is determined to be $(1.869 \pm 0.007) \times 10^3$ cm/s. The carrier lifetime increases with decreasing temperature from room temperature to 175 K and then decreases with decreasing temperature, suggesting non-radiative recombination dominates at high temperatures and radiative recombination dominates at low temperatures. A maximum lifetime of 105 ns is observed at 175 K for the 200 nm MgCdTe sample. The temperature-dependent lifetimes also suggest that the thermionic induced interface recombination dominates the total recombination at room temperature. These promising results show the great potential of using 1.7 eV MgCdTe for II-VI/Si tandem solar cells.

REFERENCES

[1] S. Esterly and R. Gelman, “2013 Renewable Energy Data Book,” 2013.

[2] “Best research-cell efficiencies,” 2014. [Online]. Available: http://www.nrel.gov/ncpv/images/efficiency_chart.jpg.

[3] “New world record for solar cell efficiency at 46%,” *Soitec press release*, 2014. [Online]. Available: http://www.soitec.com/en/news/press-releases/new-world-record-for-solar-cell-efficiency-at-46-percent-1599/.

[4] “New world record for solar cell efficiency at 46% French-German cooperation confirms competitive advantage of European photovoltaic industry,” *Fraunhofer ISE press release*, 2014. [Online]. Available: http://www.ise.fraunhofer.de/en/press-and-media/press-releases/press-releases-2014/new-world-record-for-solar-cell-efficiency-at-46-percent.

[5] B. M. Kayes, H. Nie, R. Twist, S. G. Spruytte, F. Reinhardt, I. C. Kizilyalli, and G. S. Higashi, “27.6 % conversion efficiency, a new record for single-junction solar cells under 1 sun illumination,” in *Proceedings of 37th Photovoltaic Specialists Conference*, 2011, pp. 4–8.

[6] M. A. Green, K. Emery, Y. Hishikawa, W. Warta, and E. D. Dunlop, “Solar cell efficiency tables (Version 45),” *Prog. Photovoltaics Res. Appl.*, vol. 23, p.1, 2015.

[7] “Panasonic HIT® solar cell achieves world’s highest energy conversion efficiency of 25.6% at research level,” *Panasonic press release*, 2014. [Online]. Available: http://news.panasonic.com/press/news/official.data/data.dir/2014/04/en140410-4/en140410-4.html.

[8] “First Solar builds the highest efficiency thin film PV cell on record,” *First Solar press release*, 2015. [Online]. Available: http://investor.firstsolar.com/releasedetail.cfm?ReleaseID=895118.

[9] "New best mark in thin-film solar performance with 21.7 percent efficiency," *ZSW press release*, 2014. [Online]. Available: http://www.zsw-bw.de/en/support/press-releases/press-detail/zsw-brings-world-record-back-to-stuttgart.html.

[10] G. J. Bauhuis, P. Mulder, E. J. Haverkamp, J. C. C. M. Huijben, and J. J. Schermer, "26.1% thin-film GaAs solar cell using epitaxial lift-off," *Sol. Energy Mater. Sol. Cells*, vol. 93, no. 9, p. 1488, 2009.

[11] W. Shockley and H. J. Queisser, "Detailed balance limit of efficiency of p-n junction solar cells," *J. Appl. Phys.*, vol. 32, no. 3, p. 510, 1961.

[12] C. H. Henry, "Limiting efficiencies of ideal single and multiple energy gap terrestrial solar cells," *J. Appl. Phys.*, vol. 51, no. 8, p. 4494, 1980.

[13] D. Ding, S. R. Johnson, and Y.-H. Zhang, "A semi-analytical model for semiconductor solar cells: From detailed balance to practical devices," in *Proceedings of 35th Photovoltaic Specialists Conference*, 2010, pp. 002908–002911.

[14] D. Ding, S. R. Johnson, S.-Q. Yu, S.-N. Wu, and Y.-H. Zhang, "A semi-analytical model for semiconductor solar cells," *J. Appl. Phys.*, vol. 110, no. 12, p. 123104, 2011.

[15] T. a. Gessert, S.-H. Wei, J. Ma, D. S. Albin, R. G. Dhere, J. N. Duenow, D. Kuciauskas, a. Kanevce, T. M. Barnes, J. M. Burst, W. L. Rance, M. O. Reese, and H. R. Moutinho, "Research strategies toward improving thin-film CdTe photovoltaic devices beyond 20% conversion efficiency," *Sol. Energy Mater. Sol. Cells*, vol. 119, p. 149, 2013.

[16] M. J. DiNezza, X.-H. Zhao, S. Liu, A. P. Kirk, and Y.-H. Zhang, "Growth, steady-state, and time-resolved photoluminescence study of CdTe/MgCdTe double heterostructures on InSb substrates using molecular beam epitaxy," *Appl. Phys. Lett.*, vol. 103, no. 19, p. 193901, 2013.

[17] A. P. Kirk, M. J. DiNezza, S. Liu, X.-H. Zhao, and Y.-H. Zhang, "CdTe vs. GaAs solar cells — A modeling case study with preliminary experimental results," in *Proceedings 39th Photovoltaic Specialists Conference*, 2013, pp. 2515–2517.

[18] X.-H. Zhao, M. J. DiNezza, S. Liu, S. Lin, Y. Zhao, and Y.-H. Zhang, "Time-resolved and excitation-dependent photoluminescence study of CdTe/MgCdTe double heterostructures grown by molecular beam epitaxy," *J. Vac. Sci. Technol. B Microelectron. Nanom. Struct.*, vol. 32, no. 4, p. 040601, 2014.

[19] X.-H. Zhao, M. J. DiNezza, S. Liu, C. M. Campbell, Y. Zhao, and Y.-H. Zhang, "Determination of CdTe bulk carrier lifetime and interface recombination velocity of CdTe/MgCdTe double heterostructures grown by molecular beam epitaxy," *Appl. Phys. Lett.*, vol. 105, no. 25, p. 252101, 2014.

[20] D. Kuciauskas, A. Kanevce, J. M. Burst, J. N. Duenow, R. Dhere, D. S. Albin, D. H. Levi, R. K. Ahrenkiel, and A. T. E. T. Photoluminescence, "Minority Carrier Lifetime Analysis in the Bulk of Thin-Film Absorbers Using Subbandgap," *IEEE J. Photovoltaics*, vol. 3, no. 4, p. 1319, 2013.

[21] D. Kuciauskas, A. Kanevce, P. Dippo, S. Seyedmohammadi, R. Malik, S. Member, and A. L. P. Emission, "Minority-Carrier Lifetime and Surface Recombination Velocity in Single-Crystal CdTe," *IEEE J. Photovoltaics*, vol. 5, no. 1, p. 366, 2015.

[22] C. H. Swartz, M. Edirisooriya, E. G. LeBlanc, O. C. Noriega, P. a. R. D. Jayathilaka, O. S. Ogedengbe, B. L. Hancock, M. Holtz, T. H. Myers, and K. N. Zaunbrecher, "Radiative and interfacial recombination in CdTe heterostructures," *Appl. Phys. Lett.*, vol. 105, no. 22, p. 222107, 2014.

[23] J. N. Duenow, J. M. Burst, D. S. Albin, D. Kuciauskas, S. W. Johnston, R. C. Reedy, and W. K. Metzger, "Single-crystal CdTe solar cells with Voc greater than 900 mV," *Appl. Phys. Lett.*, vol. 105, no. 5, p. 053903, 2014.

[24] S. Liu, D. Ding, S. R. Johnson, and Y.-H. Zhang, "Optimal optical designs for planar GaAs single-junction solar cells with textured and reflective surfaces," in *Proc. of SPIE*, vol. 8256, 2012, p. 82560M.

[25] S. Liu, D. Ding, S. R. Johnson, and Y. Zhang, "Approaching single-junction theoretical limit using ultra-thin GaAs solar cells with optimal optical designs," in *Proceedings of 38th Photovoltaic Specialists Conference*, 2012, pp. 2082–2087.

[26] W. Yang, C. Allen, J. Li, H. Cotal, C. Fetzer, S. Liu, D. Ding, S. Farrell, Z. He, H. Li, H. Dettlaff, N. Karam, and Y. Zhang, "Ultra-Thin GaAs Single-Junction Solar Cells Integrated with Lattice- Matched ZnSe as a Reflective Back Scattering Layer," in *Proceedings of 38th Photovoltaic Specialists Conference*, 2012, pp. 978–981.

[27] W. Yang, J. Becker, Y.-S. Kuo, J.-J. Li, S. Liu, B. Landini, K. Campman, and Y.-H. Zhang, "Ultra-thin GaAs single-junction solar cells integrated with an AlInP layer for reflective back scattering," in *Proceedings of 39th Photovoltaic Specialists Conference*, 2013, pp. 3329–3332.

[28] S. Liu, W. Yang, J. Becker, Y. Kuo, and Y. Zhang, "Non-Lambertian reflective back scattering and its impact on device performance of ultra-thin GaAs single-junction solar cells," *IEEE J. Photovoltaics*, vol. 5, no. 3, p. 832, 2015.

[29] S. Liu, X.-H. Zhao, C. Campbell, M. J. DiNezza, Y. Zhao, and Y.-H. Zhang, "Minority carrier lifetime of lattice-matched CdZnTe alloy grown on InSb substrates using molecular beam epitaxy," *J. Vac. Sci. Technol. B, Nanotechnol. Microelectron. Mater. Process. Meas. Phenom.*, vol. 33, no. 1, p. 011207, 2015.

[30] S. Liu, X.-H. Zhao, C. M. Campbell, M. Lassise, Y. Zhao, and Y. Zhang, "Carrier lifetimes and interface recombination velocities in CdTe/$Mg_xCd_{1-x}Te$ double heterostructures with different Mg compositions grown by molecular beam epitaxy," *Appl. Phys. Lett.*, 2015.

[31] S. Liu, X.-H. Zhao, C. M. Campbell, M. B. Lassise, Y. Zhao, and Y. Zhang, "Impacts of thermionic emission and tunneling on the carrier recombination in CdTe/MgCdTe double heterostructures," *Appl. Phys. Lett.*, 2015.

[32] F. Urbach, "The long-wavelength edge of photographic sensitivity and of the electronic absorption of solids," *Phys. Rev.*, vol. 92, no. 5, p. 1324, 1953.

[33] G. B. Rybicki and A. P. Lightman, *Radiative Processes in Astrophysics*. John Wiley and Sons, 1979.

[34] J.-B. Wang, S. R. Johnson, D. Ding, S.-Q. Yu, and Y.-H. Zhang, "Influence of photon recycling on semiconductor luminescence refrigeration," *J. Appl. Phys.*, vol. 100, no. 4, p. 043502, 2006.

[35] E. D. Palik, *Handbook of optical constants of solids*. New York, NY: Academic Press, 1985.

[36] S. Adachi, *Properties of Group-IV, III-V and II-VI*. Hoboken, NJ: John Wiley & Sons, 2005.

[37] B. T. Phong, "Illumination for computer-generated pictures," *Commun. ACM*, vol. 18, no. 6, p. 311, 1975.

[38] U. Rau, U. W. Paetzold, and T. Kirchartz, "Thermodynamics of light management in photovoltaic devices," *Phys. Rev. B*, vol. 90, no. 3, p. 035211, 2014.

[39] J. Zhao and M. A. Green, "Optimized antireflection coatings for high-efficiency silicon solar cells," *IEEE Trans. Electron Devices*, vol. 38, no. 8, 1991.

[40] S. Adachi, *Optical constants of crystalline and amorphous semiconductors: numerical data and graphical information*. New York, NY: Springer, 1999.

[41] W. Yang, J. Becker, S. Liu, Y. Kuo, J. Li, B. Landini, K. Campman, and H. Zhang, "Ultra-thin GaAs single-junction solar cells integrated with a reflective back scattering layer," *J. Appl. Phys.*, vol. 115, p. 203105, 2014.

[42] Mohamed Henini, Ed., *Molecular Beam Epitaxy From research to mass production*. Waltham, MA: Elsevier, 2013, p. 2.

[43] W. K. Liu and M. B. Santos, "Characterization of oxide desorption from InSb (001) substrates," *J. Vac. Sci. Technol. B Microelectron. Nanom. Struct.*, vol. 14, p. 647, 1996.

[44] M. J. DiNezza, “Monocrystalline ZnTe/CdTe/MgCdTe double heterostructure solar cells grown on InSb substrates by molecular beam epitaxy,” Arizona State University, 2014.

[45] A. Rogalski, “HgCdTe infrared detector material: history, status and outlook,” *Reports Prog. Phys.*, vol. 68, no. 10, p. 2267, 2005.

[46] O. Gravrand, G. Destefanis, S. Bisotto, N. Baier, J. Rothman, L. Mollard, D. Brellier, L. Rubaldo, a. Kerlain, V. Destefanis, and M. Vuillermet, “Issues in HgCdTe Research and Expected Progress in Infrared Detector Fabrication,” *J. Electron. Mater.*, vol. 42, no. 11, p. 3349, 2013.

[47] R. Sporken, S. Sivananthan, K. K. Mahavadi, G. Monfroy, M. Boukerche, and J. P. Faurie, “Molecular beam epitaxial growth of CdTe and HgCdTe on Si (100),” *Appl. Phys. Lett.*, vol. 55, no. 18, p. 1879, 1989.

[48] J. P. Zanatta, G. Badano, P. Ballet, C. Largeron, J. Baylet, O. Gravrand, J. Rothman, P. Castelein, J. P. Chamonal, a. Million, G. Destefanis, S. Mibord, E. Brochier, and P. Costa, “Molecular beam epitaxy growth of HgCdTe on Ge for third-generation infrared detectors,” *J. Electron. Mater.*, vol. 35, no. 6, p. 1231, 2006.

[49] R. N. Jacobs, C. Nozaki, L. a. Almeida, M. Jaime-Vasquez, C. Lennon, J. K. Markunas, D. Benson, P. Smith, W. F. Zhao, D. J. Smith, C. Billman, J. Arias, and J. Pellegrino, “Development of MBE II–VI Epilayers on GaAs(211)B,” *J. Electron. Mater.*, vol. 41, no. 10, p. 2707, 2012.

[50] W. Lei, R. J. Gu, J. Antoszewski, J. Dell, and L. Faraone, “GaSb: A New Alternative Substrate for Epitaxial Growth of HgCdTe,” *J. Electron. Mater.*, vol. 43, no. 8, p. 2788, 2014.

[51] T. J. de Lyon, R. D. Rajavel, B. Z. Nosho, S. Terterian, M. L. Beliciu, P. R. Patterson, D. T. Chang, M. F. Boag-O’Brien, B. T. Holden, R. N. Jacobs, and J. D. Benson, “MBE Growth and Transfer of HgCdTe Epitaxial Films from InSb Substrates,” *J. Electron. Mater.*, vol. 39, no. 7, p. 1058, 2009.

[52] S. Adachi, *Handbook on physical properties of semiconductors: II-VI compound semiconductors*. Boston, MA: Kluwer Academic Publishers, 2004.

[53] L. W. Molenkamp and H. F. J. van't Blik, "Very low interface recombination velocity in (Al,Ga)As heterostructures grown by organometallic vapor-phase epitaxy," *J. Appl. Phys.*, vol. 64, no. 8, p. 4253, 1988.

[54] R. J. Nelson and R. G. Sobers, "Interfacial recombination velocity in GaAlAs/GaAs heterostructures," *Appl. Phys. Lett.*, vol. 32, no. 11, p. 761, 1978.

[55] J. M. Olson, R. K. Ahrenkiel, D. J. Dunlavy, B. Keyes, and a. E. Kibbler, "Ultralow recombination velocity at Ga0.5In0.5P/GaAs heterointerfaces," *Appl. Phys. Lett.*, vol. 55, no. 12, p. 1208, 1989.

[56] G. D. Gilliland, D. J. Wolford, T. F. Kuech, J. a. Bradley, and H. P. Hjalmarson, "Minority-carrier recombination kinetics and transport in '"surface-free"' GaAs/AlxGa1−xAs double heterostructures," *J. Appl. Phys.*, vol. 73, no. 12, p. 8386, 1993.

[57] R. Cohen, V. Lyahovitskaya, E. Poles, a. Liu, and Y. Rosenwaks, "Unusually low surface recombination and long bulk lifetime in n-CdTe single crystals," *Appl. Phys. Lett.*, vol. 73, no. 10, p. 1400, 1998.

[58] M. O. Reese, J. M. Burst, C. L. Perkins, A. Kanevce, S. W. Johnston, D. Kuciauskas, T. M. Barnes, and W. K. Metzger, "Surface Passivation of CdTe Single Crystals," *IEEE J. Photovoltaics*, vol. 5, no. 1, p. 382, 2015.

[59] K. W. Mitchell, A. L. Fahrenbruch, and R. H. Bube, "Evaluation of the CdS/CdTe heterojunction solar cell," *J. Appl. Phys.*, vol. 48, no. 10, p. 4365, 1977.

[60] E. Marín, J. Santoyo, A. Calderón, O. Vigil-Galán, and G. Contreras-Puente, "Influence of the thiourea/CdCl2 concentration ratio used for the chemical bath deposition of CdS thin films, upon the CdS/CdTe interface recombination velocity in CdTe/CdS/glass structures.," *J. Appl. Phys.*, vol. 107, no. 12, p. 123701, 2010.

[61] H. A. Bethe, "Theory of the boundary layer of crystal rectifiers," *MIT Radiat. Lab. Rep.*, vol. 43, p. 12, 1942.

[62] S. M. Sze and K. K. Ng, *Physics of semiconductor devices*, 3rd ed. Hoboken, NJ: John Wiley & Sons, 2007, p. 47.

[63] R. Tsu and L. Esaki, "Tunneling in a finite superlattice," *Appl. Phys. Lett.*, vol. 22, no. 11, p. 562, 1973.

[64] S. M. Sze and K. K. Ng, *Physics of semiconductor device physics*, 3rd ed. Hoboken, NJ: John Wiley & Sons, 2007, p. 48.

[65] M. a. Steiner, J. F. Geisz, I. García, D. J. Friedman, a. Duda, and S. R. Kurtz, "Optical enhancement of the open-circuit voltage in high quality GaAs solar cells," *J. Appl. Phys.*, vol. 113, no. 12, p. 123109, 2013.

[66] P. Asbeck, "Self-absorption effects on the radiative lifetime in GaAs-GaAlAs double heterostructures," *J. Appl. Phys.*, vol. 48, no. 2, p. 820, 1977.

[67] R. K. Ahrenkiel, D. J. Dunlavy, B. Keyes, S. M. Vernon, T. M. Dixon, S. P. Tobin, K. L. Miller, and R. E. Hayes, "Ultralong minority-carrier lifetime epitaxial GaAs by photon recycling," *Appl. Phys. Lett.*, vol. 55, no. 11, p. 1088, 1989.

[68] S. L. Chuang, *Physics of Photonic Devices*, 2nd ed. John Wiley & Sons, 2009.

[69] B. Kuhn-Heinrich, W. Ossau, H. Heinke, F. Fischer, T. Litz, a. Waag, and G. Landwehr, "Optical investigation of confinement and strain effects in CdTe/(CdMg)Te quantum wells," *Appl. Phys. Lett.*, vol. 63, no. 21, p. 2932, 1993.

[70] A. Waag, F. Fischer, T. Litz, B. Kuhn-Heinrich, U. Zehnder, W. Ossau, W. Spahn, H. Heinke, and G. Landwehr, "Wide gap Cd1-xMgxTe : molecular beam epitaxial growth and characterization," *J. Cryst. Growth*, vol. 138, p. 155, 1994.

[71] M. Umeno, T. Soga, K. Baskar, and T. Jimbo, “Heteroepitaxial technologies on Si for high-efficiency solar cells,” *Sol. Energy Mater. Sol. Cells*, vol. 50, no. 1–4, p. 203, 1998.

[72] J. F. Geisz, J. M. Olson, M. J. Romero, C. S. Jiang, and A. G. Norman, “Lattice-mismatched GaAsP solar cells grown on silicon by OMVPE,” in *Proc. IEEE 4th World Conference on Photovoltaic Energy Conversion*, 2006, pp. 772–775.

[73] H. Taguchi, T. Soga, and T. Jimbo, “Fabrication of GaAs/Si Tandem Solar Cell by Epitaxial Lift-Off Technique,” *Jpn. J. Appl. Phys.*, vol. 42, no. Part 2, No. 12A, p. L1419, 2003.

[74] J. Yang, Z. Peng, D. Cheong, and R. Kleiman, “Fabrication of High-Efficiency III–V on Silicon Multijunction Solar Cells by Direct Metal Interconnect,” *IEEE J. Photovoltaics*, vol. 4, no. 4, p. 1149, 2014.

[75] M. Carmody, S. Mallick, J. Margetis, R. Kodama, T. Biegala, D. Xu, P. Bechmann, J. W. Garland, and S. Sivananthan, “Single-crystal II-VI on Si single-junction and tandem solar cells,” *Appl. Phys. Lett.*, vol. 96, no. 15, p. 153502, 2010.

[76] A. Waag, H. Heinke, S. Scholl, C. R. Becker, and G. Landwehr, “Growth of MgTe and Cd1-xMgxTe thin films by molecular beam epitaxy,” *J. Cryst. Growth*, vol. 131, p. 607, 1993.